2001

A novel continuation-based quasi-steady-state analysis approach to mitigate long-term voltage instability

Qin Wang
Iowa State University

INFORMATION TO USERS

This manuscript has been reproduced from the microfilm master. UMI films the text directly from the original or copy submitted. Thus, some thesis and dissertation copies are in typewriter face, while others may be from any type of computer printer.

The quality of this reproduction is dependent upon the quality of the copy submitted. Broken or indistinct print, colored or poor quality illustrations and photographs, print bleedthrough, substandard margins, and improper alignment can adversely affect reproduction.

In the unlikely event that the author did not send UMI a complete manuscript and there are missing pages, these will be noted. Also, if unauthorized copyright material had to be removed, a note will indicate the deletion.

Oversize materials (e.g., maps, drawings, charts) are reproduced by sectioning the original, beginning at the upper left-hand corner and continuing from left to right in equal sections with small overlaps.

Photographs included in the original manuscript have been reproduced xerographically in this copy. Higher quality 6" x 9" black and white photographic prints are available for any photographs or illustrations appearing in this copy for an additional charge. Contact UMI directly to order.

ProQuest Information and Learning
300 North Zeeb Road, Ann Arbor, MI 48106-1346 USA
800-521-0600

A novel continuation-based quasi-steady-state analysis approach to mitigate long-term voltage instability

by

Qin Wang

A dissertation submitted to the graduate faculty

in partial fulfillment of the requirements for the degree of

DOCTOR OF PHILOSOPHY

Major: Electrical Engineering (Electric Power)

Major Professor: Venkataramana Ajjarapu

Iowa State University

Ames, Iowa

2001

Graduate College
Iowa State University

This is to certify that the Doctoral dissertation of

Qin Wang

has met the dissertation requirements of Iowa State University

Signature was redacted for privacy.

Major Professor

Signature was redacted for privacy.

For the Major Program

Signature was redacted for privacy.

For the Graduate College

TABLE OF CONTENTS

LIST OF TABLES

LIST OF FIGURES

ACKNOWLEDGMENTS

I would like to thank my advisor, Dr. Venkataramana Ajjarapu, for the time, effort and advice, that he generously provided throughout this work. His professional enthusiasm encouraged me and his constant guidance was of immense help during the course of this endeavor.

I would also like to thank Dr. W. Kliemann for his great help and encouragement during this research work and for serving on my committee.

I greatly appreciate Dr. Vijay Vittal, Dr. M. Khammash, and Dr. J. D. McCalley's valuable comments on this work as well as their other contributions as members of my committee.

My sincere thanks to Jian Fu, Yuan Zhou, Nagaraj Balijepalli, and all other friends for their friendship and assistance.

I am thankful for the support and encouragement of my parents throughout all of my college years. I offer a sincere "thank-you" from the depths of my heart.

A novel continuation-based quasi-steady-state analysis approach to mitigate long-term voltage instability

Qin Wang

Major Professor: Venkataramana Ajjarapu
Iowa State University

A novel Continuation-based Quasi-Steady-State (CQSS) analysis is developed and integrated with trajectory sensitivity which in turn can be used to address various aspects of control strategies to mitigate long-term voltage collapse.

In this research, two scenarios are defined according to the severity of the contingency:

- Scenario One: The post-contingency long-term load characteristic intersects the system's PV curve:
- Scenario Two: The post-contingency long-term load characteristic doesn't intersect the system's PV curve:

First, the CQSS simulation, which is based on two different parameterizations, is utilized to trace the system trajectory after the contingency. One is for Scenario One where load change and OLTC action are considered. The other is for Scenario Two where load restoration and OLTC action are taken into account simultaneously. Secondly, the identification of the saddle node bifurcation point (SNB) and singularity-induced bifurcation (SIB) point can be accomplished by either continuation parameter or trajectory sensitivity. A new approach is developed in the CQSS simulation to approximate the differential representation of the thermostatic load restoration. It also avoids the numerical problem around the singularity point.

The salient features of this research are listed below:

- A new CQSS simulation is developed.
  - It is numerically well-conditioned.
  - It can readily identify the SIB point and the SNB point.

  - The time information of the controls can be obtained automatically.
  - Combined effects of the OLTCs and the load change on voltage stability are taken into account.

- A computationally-fast approximation of the generic load restoration is developed.
  - Parameterization of the load exponent provides a new way to approximate the load restoration in the long-term time scale.
  - The change of load types and compositions with the time can be considered.

- Trajectory sensitivity is derived and calculated in two ways.
  - It is applied to identify the long-term SNB point.
  - It is related to margin sensitivity by using continuation method.
  - It is used to formulate the control problem to maintain a sufficient stability margin.

- A systematic and comprehensive control strategy to mitigate long-term voltage instability is developed and implemented.

This proposed methodology is tested on two systems.

1 INTRODUCTION

1.1 Practical Definition of Power System Stability

Power system stability [1] can be generally defined as a property of a power system that enables it to remain in a stable operating equilibrium under normal operating conditions and regain an acceptable state of equilibrium after being subjected to a disturbance.

Nowadays voltage stability has been considered a major limiting factor for secure operation of many power systems worldwide. There is an increasing concern about voltage collapse in an open access environment since the less regulated power flow patterns and the increased utilization of transmission facilities potentially make power systems more vulnerable to voltage collapse [1, 2, 3, 4, 5].

For the purpose of understanding, it is helpful to define some terms related to voltage stability as developed by the IEEE and the CIGRÉ [4, 6, 7].

- Small-disturbance voltage stable: An operating point of a power system is *small-disturbance voltage stable* if, following any small disturbance, voltages near loads are identical or close to the pre-disturbance values. (Mathematically, small-disturbance voltage stability analysis means the disturbance is small enough that a linearized dynamic model can be used to model the original system.)

- Voltage collapse: A power system enters a state of *voltage collapse* when a disturbance, an increase in load demand, or a change in system condition, causes a progressive, uncontrollable drop in the voltage. Voltage collapse may be total (blackout) or partial.

We can now place voltage stability within the context of power system stability in general. Table 1.1 shows a classification scheme based on two criteria: time scale and driving force of instability. For voltage stability, the relative load characteristics are also listed.

The time frame of rotor angle stability is that of electromechanical dynamics, lasting typically for a few seconds. Automatic voltage regulators, excitation systems, turbine and governor dynamics, all act within this time frame. The loads considered here are generally induction motors and HVDC

Table 1.1 Power system stability classification

Time scales	Generator-driven	Load-driven	Load characteristics
Short-term	rotor angle stability	short-term	transient (short-term)
	transient small-signal	voltage stability	steady-state (long-term)
Long-term	frequency stability	long-term	transient (short-term)
		voltage stability	steady-state (long-term)

interconnections, which have their own transient and steady-state characteristics. When the above mentioned short-term dynamics are stable and eventually die out, the system enters a slower time frame. Various dynamic components are present in this time frame such as transformer tap changers and generator limiters. The relevant transients last typically for several minutes. This time frame is referred to as long-term time scale. In this time scale, frequency problems are due to generation-load imbalance irrespective of network aspects within each connected area, whereas voltage problems mainly come from the electrical distance between generation and loads and thus depend on the network structure. The dynamics in these two time scales are represented mathematically by the differential equations using different time constants.

With these definitions in mind, we will briefly touch upon the different techniques used in recent years for voltage stability research.

1.2 Concepts of Preventive and Corrective Control

Considerable research has been done on many aspects of the voltage stability problem. Generally, it can be divided into two parts: offline studies and online studies. In the offline environment, the overall procedure includes the following stages:

- Tools and Techniques: Choosing appropriate tools and techniques may be the first step that should be considered in voltage stability research. Power flow analysis, Quasi-Steady-State analysis and transient stability analysis, are the major tools that can be selected to do static or dynamic analysis of the system. They can be used to understand the mechanisms of the problem and make operational and planning decisions based on more reliable simulations.

- Modeling Issues: Selecting suitable models and scenarios for the simulation associated with voltage collapse is very important. The interaction of system load and equipment, such as generator protection, OLTC transformer control, shunt compensation or load shedding, plays an important

role in this process. Understanding the dynamics related to the devices will allow the engineers to make the best decisions on control schemes.

- Indices: Using indices online or offline could help operators determine whether the system's state is secure or not. Additionally, they could be considered as the criteria for the system security assessment.

- Control Strategy: Creating a comprehensive preventive and corrective methodology is necessary to mitigate voltage collapse. In cases for which the voltage stability criterion is not satisfied, remedial control measures have to be designed to enhance the system to meet the criterion.

The ultimate goal of the research on voltage stability is to develop and implement an effective control strategy to cope with voltage collapse. There are two basic and complementary concepts: preventive and corrective control (PCC). The purpose of preventive control regarding voltage stability is to shift the current operating state to a secure level before the instability actually occurs [8, 9, 10]. The corrective control exists to stabilize an unstable power system, directing the system's trajectory onto a new stable equilibrium point shortly after a severe contingency. Corrective control generally refers to a set of control actions that specifically stabilize the post-contingency unsolvable system.

For the sake of clarity, Figures 1.1 and 1.2 depict the concepts of preventive and corrective control by PV diagrams respectively. In order to understand these curves, some terms should be clarified first.

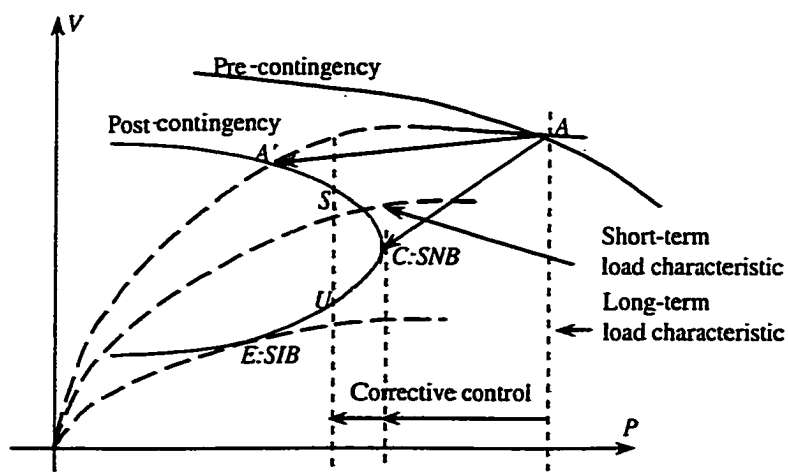

Figure 1.1 Concept of corrective control

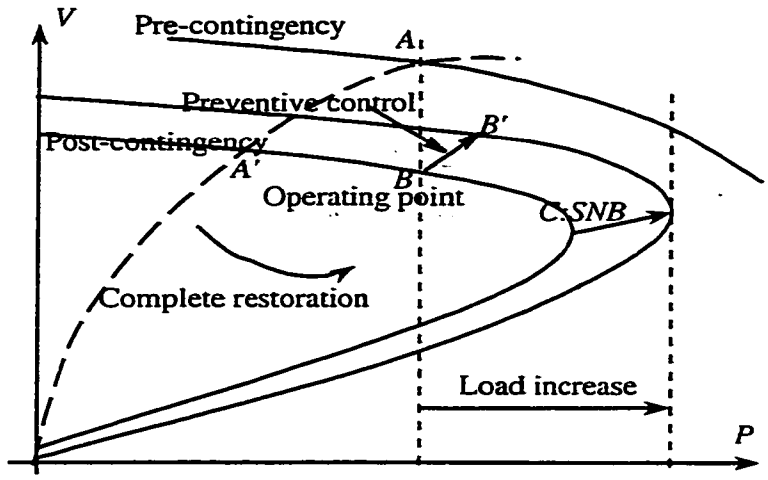

Figure 1.2 Concept of preventive control

- Network PV curve: It is the curve of load voltage as a function of the real power of the system. Each point of the PV curve corresponds to the equilibrium condition of the generation and transmission systems under a specified load demand. It represents the characteristics of the network.

- Load demand: It is an independent variable which corresponds to the amount of connected equipment. It is important to emphasize the clear distinction made between actually consumed load power and load demand. This distinction is necessary for the understanding of a basic instability mechanism by which increased demand may result in reduced consumption of power.

- Short-term load characteristic: The load real or reactive power is defined as the function of voltage. load demand and load state. In the short term, load dynamics can be described by the differential equation of the load state. The intersection of the short-term load characteristic curve and the network PV curve is the short-term equilibrium.

- Long-term load characteristic: The load real or reactive power is defined as the function of voltage and load demand. It doesn't depend on the load state variable. The intersection of the long-term load characteristic curve and the network PV curve is the long-term equilibrium. In this research, when "long-term (resp. short-term)" is used to define an equilibrium, a bifurcation point or a specific operating point, the "long-term" is from the load characteristic point of view. When

"long-term (resp. short-term)" is applied to describe voltage stability or dynamics. the "long-term" is based on the whole time scale for stability classification (see Table 1.1).

- Nose point and bifurcation point: The nose point of the PV curve can be explained as an operating point where the transmission network delivers the maximum real power. It is not generally the bifurcation point from the stability point of view. PV curve is not a bifurcation diagram since P is not an independent variable according to the particular load model. The exception to this case occurs when the constant power load model is used.

- Loadability limit: It is the point where the load characteristic becomes tangent to the network characteristic. At this point, the load demand reaches its maximum value. A load increase beyond this point results in the loss of equilibrium and the system can't operate any more. It is the bifurcation point of the system. It can also be defined corresponding to the short-term and long-term load characteristics. Note that loadability limit doesn't necessarily coincide with the nose point of the PV curve in the long term, since it depends on the load characteristic.

In Figure 1.1, before the contingency, the system operates at point A. Due to a severe contingency, the network PV curve shrinks so that it no longer intersects the long-term load characteristic curve. An unsolvable case will occur at A in the long-term time scale. However, just after the contingency, the load responds instantaneously with its short-term characteristic and it decreases because the voltage drops. The system's operating point jumps from A to A' according to the short-term load characteristic. After A', two factors come in and drives the system's evolution. One is the on-load tap changer transformer (OLTC) and the other is the load self-restoration.

Once the OLTC starts to operate, voltage at the load bus will gradually be brought up toward its reference value, and load power increases, provided the tap ratio does not reach its limit. Restoration of load bus voltage and load power may increase the reactive demand on generators sufficiently to raise generator field currents above their continuous limits. The limiting of generator field current causes the generator terminal voltage to be reduced. This in turn causes the load bus voltages to go down, initiating further OLTC operations.

Load self-restoration recovers the load from its short-term characteristic to its long-term characteristic by changing the load state variable. Since the network load power supply is less than the load demand at A', the load dynamics will try to draw more power by increasing the load state variable. This is equivalent to increasing the load conductance or the load current. It drives the operating point to a lower voltage. If the imbalance between the load demand and the network supply persists, the

system will continuously operate on the intersection of the post-contingency PV curve and the drifting short-term load characteristic curve with a monotonically decreasing voltage.

Therefore, these two dynamics shift the short-term load characteristic curve consequentially from higher voltage to lower voltage. Three dashed lines in Figure 1.1 represent the short-term load characteristics with three different tap ratios of the OLTC or three different load state variables of the load self-restoration (Appendix E).

Without any control, the system reaches the singularity induced bifurcation (SIB) [11] point E, where the short-term load characteristic curve is tangent to the network PV curve and a final collapse happens. Hence, corrective control of load shedding should be quickly carried out to save the system. This will change the long-term and short-term load characteristics as well as the network PV curve. The aim of corrective control is to create a new long-term equilibrium while considering the load dynamics in the short term.

From the long-term point of view, it is required to decrease the load below the value corresponding to the long-term saddle node bifurcation (SNB) point C. If the long-term constant power load is assumed, this will shift the vertical long-term load characteristic (dotted line) to the left, yielding the stable (resp. unstable) equilibrium S (resp. U).

From the short-term point of view, load shedding moves the dashed line of the short-term load characteristic to an operating point that has a little higher voltage. To achieve a successful load shedding, the new intersection of the short-term load characteristic and the network PV curve should be located in the region of attraction of S.

Note, if the power factor is large, the network PV curve is almost unchanged by load shedding [12]. However, if another control such as shunt compensation is taken into account, there will be a new "post-control" network PV curve.

It is necessary to perform controls to increase the stability margin if it is not sufficient. Insufficiency may result from some small contingencies. This is not the true preventive control which is defined as the control actions to prevent the actual contingency. In the case presented in Figure 1.2, the short-term load characteristic (dashed line) can be fully restored to the long-term load characteristic (dotted line). After the contingency, the system is initially operated at A' according to the short-term load characteristic. Due to either the OLTC or the load self-restoration, the system completely restores to the long-term equilibrium B. Each point on the PV curve is the short-term equilibrium before B and the long-term equilibrium afterwards. After the restoration is fully achieved, the component associated with the OLTC will not play a significant role in voltage stability, though it may try to maintain the

voltage. Other factors, for example, load increase, come in and dominate the system's slow evolution. We mainly consider the long-term load characteristic after B.

In Figure 1.2, if the present operating point B is not secure by evaluating the voltage stability quantitatively, different control variables are adjusted in an economical and efficient way so that the stability margin between B and the long-term SNB point C can be enlarged to meet the specified requirement. If no control actions had been taken when the load demand is increased according to a given scenario, the system would result in a voltage collapse. This control is aimed to shift the current operating state (B) to a secure state (B') in advance, so as to maintain a specified stability margin.

Now we know that in this research the controls deal with the conditions of a system after some contingencies. Table 1.2 summarizes the various steps and corresponding means involved in voltage instability estimation and control. The following sections briefly describe some important approaches that are used in voltage stability analysis.

Table 1.2 Procedure of post-contingency analysis

Steps	Means
Contingency evaluation	Post-contingency power flow
	Multi-time-scale simulation
	Quasi-Steady-State
	long-term simulation
Critical point determination	Continuation power flow (CPF)
	Optimization methods
	Time simulation together
	with sensitivity analysis
Preventive/corrective control	Sensitivity and eigenvector analysis
	Optimization method

1.3 Steady-State Analysis

Steady-state analysis can capture the loss of a long-term equilibrium since it is based on algebraic equations that stem from the equilibrium conditions of long-term dynamics. The point of the singularity of the power flow Jacobian, is regarded as the point of voltage collapse. There are unreasonable assumptions used in representing the system by the power flow model. In general, the singularity of the power flow Jacobian does not indicate instability. Meanwhile, it is unable to represent the system's behavior "beyond the critical point" as well as account for controls that depend on the system's time evolution.

1.4 Large-Disturbance Analysis

When the power system is subjected to large perturbations such as short circuits, multi-time domain simulation is well-known as a single tool to cover all instabilities. Therefore, it is very helpful in determining the control actions. However, time domain simulation needs to deal with the instability of short-term dynamics and requires extensive output processing and analysis to find the causes of voltage instability. Although numerical integration techniques have become more efficient, time domain simulation takes much more computing time, especially with respect to long-term analysis and remains heavy in data maintenance. It is not adequate for real-time applications.

1.5 Small-Disturbance Analysis

The aim of small-disturbance voltage stability analysis is to determine whether a suggested operating point of a power system will be voltage stable with respect to a small disturbance. To achieve it, the original nonlinear dynamic equations are linearized around the specified operating point and the system matrix is calculated. The eigenvalues of the system matrix determine the dynamic response to the system for small disturbances around this point. However, the eigenvalue calculation is very expensive and thus is very demanding for large system studies.

1.6 Quasi-Steady-State Analysis

In between steady-state analysis and full numerical integration, there is some room for Quasi-Steady-State (QSS) long-term analysis. It has the following features:

- It focuses on the cause of instability: long-term dynamics;
- It is sufficient for the purpose of voltage stability analysis;
- It is a compromise between the efficiency of steady-state analysis methods and the modeling advantage of time-domain methods;
- It performs extensive simulations, typical of planning and operational planning;
- It has interactive use as an operator tool;
- It is adequate for real-time use in emergency conditions.

Nevertheless, there are still some limitations of the original QSS long-term simulation since it is based on conventional power flow. The main problems associated with it are explained as follows:

- It is sensitive to the selection of slack bus;
- The divergence may be caused by purely numerical problems;
- In truly unstable cases, following divergence, it leaves us without information on the nature and location of the problem, remedies, etc.

1.7 Organization of the Thesis

The thesis is organized as follows:

The introduction in Chapter 1 provides a motivation for the research work as well as a general summary of the techniques used. The literature review in Chapter 2 provides a concise record of the source material, related topics and background information, as well as gives the scope of this research and its salient features. Chapter 3 gives the power system model used in this work. Chapter 4 contains the general idea of the continuation-based QSS analysis and presents the major improvements in this work. Chapter 5 proposes a load restoration scheme for the long-term voltage stability study by using continuation method. Chapter 6 describes the procedure to obtain trajectory sensitivity by studying the differential and algebraic equations of the power system and its application to voltage control. Chapter 7 presents the formulation of the voltage control problem and proposes the method to solve it. For the purpose of understanding this research consistently, numerical results on a small test system are given from Chapter 4 to Chapter 7. The simulation results on the New England system shown in Chapter 8, validate the proposed approach. Chapter 9 presents the conclusions and provides some directions for future work. The derivations of some key concepts associated with this research are presented in the appendices.

During all the processes, we try to clarify, mathematically and practically, some basic concepts related to the voltage stability problem.

2 LITERATURE REVIEW AND SCOPE OF PRESENT WORK

Voltage instability or collapse generally arises from two types of system events: gradual deterioration in the system's operating conditions due to a rapid load pickup, and severe contingency. For the first type of event, the system's state can be approximately assumed to move from one operating point of relative security to another with increased vulnerability through a quasi-steady-state variation. In such a scenario, the system could experience voltage collapse as a result of either a saddle node bifurcation, or a Hopf bifurcation. Sometimes, voltage collapse can also occur immediately after some generators activate their field current limitations or armature current limitations as indicated in [13]. For the events of contingency type, the system could lose voltage stability transiently; in that case, no new equilibrium exists after a contingency or no early enough control actions are carried out, to attract the system's trajectory towards a new stable equilibrium.

2.1 Review of Previous Work

Until now, preventive measures were the principal measures of providing voltage stability. However, since everyday operational experience has shown that some voltage collapse happens in non-typical operating regimes, much attention has been paid recently to the development of appropriate corrective measures [9, 14].

Traditionally, preventive and corrective controls can be formulated as a nonlinear optimization problem as follows:

$$\begin{aligned} & min && f(x, y, \mu) && (2.1)\\ subject\ to\quad & && g(x, y, \mu) = 0 && (2.2)\\ & && h(x, y, \mu) \leq 0 && (2.3) \end{aligned}$$

where x is the vector of state variables, y is the vector of algebraic variables and μ is the vector of all controllable variables. Here $f(x, y, \mu)$ is the objective function, $g(x, y, \mu)$ is system equality constraints

including load flow balance equations, $h(x, y, \mu)$ is inequality constraints including the limits for all variables.

Control cost minimization is generally the objective of preventive control. For corrective control, the aim is to find a good load-shedding scheme which takes into account three associated issues: time, location and amount.

Preventive and corrective control is different from the traditional optimal power flow (OPF), in that OPF only considers some operating constraints of system state variables such as voltage magnitude, angle and power output, etc. However, the main purpose of preventive and corrective control is to guarantee the stable operation of the system. It means that PCC shall include some stability considerations either in the objective function or in the constraint set.

Greene et al. [15] generalized the normal vector [16] to compute the effectiveness of changing various power system parameters to increase the system's voltage stability margin. It provides one method of calculating indices for stability consideration in the PCC problem. Gao et al. [17] applied the modal analysis [18] around the nose point of a PV curve to identify the best location for a SVC device to increase the post-contingency voltage stability margin. In the preventive and corrective control problem, the location selection is very important, though it may not explicitly appear in the optimization formulation. In [19], an index based on the minimum singular value of a power flow Jacobian matrix is obtained to prevent voltage instability. It is known that a minimum singular value is a useful tool to determine the proximity to voltage collapse.

Tuan et al. [20] proposed two sensitivity-based algorithms for a fast calculation of the load-shedding amount. The stability limits are considered by the sensitivity information. Also in [21], another viable load-shedding algorithm presented is based on the indicator of voltage instability [22]. The goal of this method is to achieve an indicator profile lower than a threshold value through load-shedding to ensure that the power system will remain in a state far from the voltage instability point. However, the analysis uses static models, and the dynamic aspects associated with voltage stability are not taken into account.

In [10] and [23], T. Kumano et al. discussed a new online methodology for monitoring and rescheduling control settings to prevent voltage instability. The methodology is based upon the multiple load-flow solutions and the sensitivity analysis. The preventive control to accommodate the load increase is initiated when a pair of close power-flow solutions are detected under heavily loaded system conditions. Then it is formulated as an optimization problem and solved by the sequential unconstrained minimization technique. However, the proposed method is not optimal. Furthermore, before the control

implementation, the normal vector of the extended critical load-flow manifold has to be calculated, which is complicated and time-consuming.

All these methods use sensitivity information as the stability indicator. In fact, it is common that stability constraints are represented by some specific sensitivity obtained from various methods and incorporated in the problem formulation.

Arnborg et al. [12] also presented a method for under-voltage load shedding (UVLS). The analysis takes into account the generator and load dynamics. An iterative load-shedding scheme is shown to be successful in avoiding voltage collapse in the long-term time scale. In [24], R. Balanathan proposed a simpler but still powerful under-voltage load-shedding criterion using a dynamic load model. A nonlinear optimization technique is used to estimate the parameters of the dynamic load model. However, the speed of the estimation process restricts the implementation of the UVLS criterion only for short-term voltage stability problems. Strictly, they should not be considered as the PCC problems, since they simply use some criteria to implement controls and are not optimization-based.

For corrective control, load shedding is one of the principal means because of its regulating capabilities with regard to the speed of the voltage phenomena [9]. The other control measures, such as generation re-dispatch, AVR regulation, capacitor/reactor switching, OLTC tap changers, phase angle shifters and SVC resources offer significant contributions to the prevention of voltage collapse.

D.S. Popovic et al. [25] investigated the impact of load shedding and secondary voltage control on voltage stability. They introduced a new secondary voltage control emergency-assist mode in cases where voltage instability had been initiated. The local and system approaches to load shedding are analyzed. Then, the emergency-assist mode of secondary voltage control and the developed system-load-shedding procedure are integrated into a new linear optimization model, representing the unified multi-step remedy for voltage-unstable regimes. It shows that the coordinated emergency action of secondary voltage control and load shedding can efficiently prevent an already initiated voltage-collapse process. In this optimization problem, some online estimated sensitivities linking pilot-bus-voltage deviations, reactive-injection deviations and voltage deviations at critical buses, with the change of generator terminal buses, are needed to deal with the stability issue.

In order to restore power system solvability due to a severe contingency, Overbye [26, 27] used the special convergence characteristic of damped Newton method and the concept of normal vector [16] to compute the closest point on the power flow solvability boundary. Then, linear approximation together with control sensitivity are used to determine the control quantities. In this case, control sensitivity plays an important role in enhancing the system's voltage stability.

Van Cutsem et al. [28] proposed an approach integrating fast simulation, instability diagnosis and corrective control determination. This fast simulation method, initially proposed in [29] and called Quasi-Steady-State analysis, approximates the long-term evolution by a succession of equilibrium points. The heart of instability diagnosis is an identification of the so-called critical point along the simulated system trajectory. Stability conditions of a set of tap changers are derived, and their implementation using fast sensitivity calculations, is described. In his method, the binary section method is applied to determine the minimum amount of load that shall be shed. The location and time issues relating to load shedding are considered in the simulation and the sensitivity calculation.

Van Cutsem [30] first applied the very "strong" voltage dependent load model reducing the load demand to obtain a solution inside the post-contingency boundary. Then along the system's transient trajectory, he found the critical point, and continued with basically the same methodology as [26]. Furthermore, he proposed a decision tree methodology to tackle voltage security concerns under preventive-wise and corrective-wise facets [31]. The whole process involved here is not associated with the optimization procedure for the general PCC problem.

Granville et al. [32] applied the direct interior point method to compute the minimum load shedding to restore the power flow solvability. Wang et al. [33] applied the same method to solve both preventive and corrective control problems. Nonlinear programming methods in general are computationally intensive in forming and factoring the Hessian matrix. Also the optimal solution involves a large number of control actions that need to be further reduced for practical implementation. In [33], voltage stability margin limits are incorporated into the inequality constraints to increase the system's operating reliability.

C.W. Taylor [9] presented a concept of undervoltage load shedding analogous to underfrequency load shedding. The load-shedding scheme is of a pre-defined type, where the amount of load to be shed was fixed as *a priori*. Tso et al. [34] presented a reliable load-shedding approach which made use of a knowledge base and extended fuzzy reasoning to arrest dynamic voltage insecurity following a disturbance. Irrespective of the nature of the dynamic voltage instability, the location and the required amount of load shedding among load control buses can be promptly presented in real-time to the system operators. However, the amount of load to be shed is also fixed *a priori*. Fuzzy logic is an advanced optimization application. All the stability considerations are included in the fuzzy reasoning process.

M.K.Pal [35] presented the viability of load shedding and capacitor switching as useful emergency measures to combat voltage collapse. It also demonstrates an explanation of the mechanism of extending voltage stability limits by means of SVC, which is very important for providing sufficient reactive

margins while the system is operated in the lower portion of the PV curve with constant power load characteristics. Meanwhile, it is shown that the blocking of LTCs might not always be justified. This tutorial paper gives the assessment of some basic corrective measures for voltage stability considering load dynamics.

Now we have a general sense of the previous experience on the PCC problem. However, after reviewing the literature, it is found that there is no systematic approach to mitigate long-term voltage instability:

- Some papers address a particular problem such as using a new index (sensitivity information) or developing an efficient analysis method to identify the effect of a specific parameter on the voltage stability. They are not focused on the control strategies.
- Some papers propose a new numerical method to the control problem such as interior point method and sequential quadratic programming. They convert the whole problem to a purely mathematical problem; however, some characteristics of power system voltage stability may not be considered in detail.
- Some papers only discuss one aspect of the control problem, either preventive control or corrective control. Moreover, the distinction between preventive control and corrective control is not clear in some papers.
- Some papers tackle both preventive control and corrective control, nevertheless, there are still some limitations. Time, location and amount issues, sometimes are not completely considered to implement controls.

An alternative is needed to solve this problem efficiently and comprehensively. This is the goal of this research.

2.2 Scope of This Work

A novel Continuation-based Quasi-Steady-State (CQSS) analysis is developed and integrated with trajectory sensitivity [36, 37] which in turn can be used to address various aspects of control strategies to mitigate long-term voltage collapse.

For the convenience of analysis, two scenarios are defined according to the severity of the contingency:

- Scenario One: The post-contingency long-term load characteristic intersects the system's PV curve:

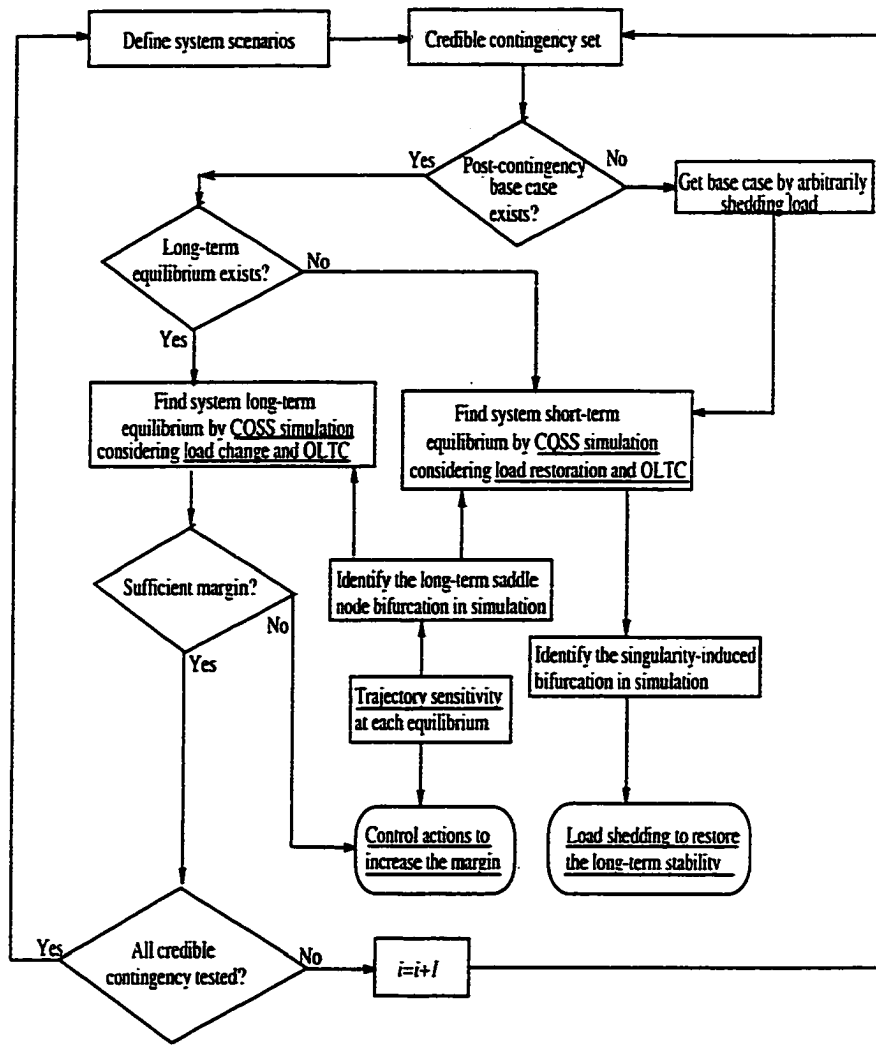

Figure 2.1 Flowchart for systematic voltage stability assessment

- Scenario Two: The post-contingency long-term load characteristic doesn't intersect the system's PV curve;

These two terms are used throughout the thesis. Figure 2.1 gives the general flowchart proposed for the systematic voltage stability assessment incorporating several basic functions such as system simulation, sensitivity analysis and control implementation. This flowchart clearly shows the links between the different parts (underlined) in this research. For an unsolvable case, corrective control actions should be developed to restore the system's long-term stability. In this thesis, we choose load shedding as the primary corrective control measure. Other controls could be considered in a similar way. In a stable case with an insufficient margin after a contingency, control actions could be devised to increase the system's stability margin to a desired level. As defined in Chapter 1, preventive control should be implemented before the actual contingency. Therefore, the margin increase designed in this work is not the real preventive control. However, the term "preventive control" appearing in this thesis simply indicates enlarging the system's stability margin following a contingency.

First, based on two different parameterizations, the CQSS simulation is utilized to trace the system's trajectory after the contingency. One is for Scenario One where both load change and OLTC action are considered. The other is for Scenario Two where load restoration and OLTC action are taken into account simultaneously. Secondly, identification of the saddle node bifurcation or the singularity-induced bifurcation can be accomplished by either trajectory sensitivity or continuation parameter. Here, a new approach is developed in the CQSS simulation to approximate the differential representation of thermostatic load restoration. It also avoids the numerical problem around the singularity point.

The salient features of this research are listed below:

- A new CQSS simulation is developed.
  - This simulation is numerically well-conditioned by introducing continuation method.
  - The new CQSS simulation can readily identify the SIB (Appendix D), and SNB points in the long-term time scale.
  - The time information of the controls can be obtained from the simulation automatically.
  - Combined effects of the OLTCs and the load change on voltage stability are taken into account.
- A computationally-fast approximation of generic load restoration is developed based on physical phenomena of power system long-term dynamics.

  - Parameterization of the load exponent provides a new way to simulate load restoration for slow load dynamics in the long-term time scale.
  - The change of load types and compositions along with the time can be considered.

- Trajectory sensitivity is derived and calculated for voltage stability studies in two ways.
  - It is applied to identify the long-term SNB point.
  - It is related to margin sensitivity at the long-term SNB point by using continuation method.
  - It is used to formulate the control problem to maintain a sufficient stability margin in such a way that the margin constraints as well as other state variable constraints could be incorporated.

- A systematic and comprehensive control strategy to mitigate the long-term voltage instability is developed and implemented. This method takes into account time, location and amount issues, with respect to load shedding.

For each item listed above, a detailed discussion on the previous work and major improvements in this research will be described in the following chapters. However, first we introduce the power system model that is suitable for the long-term voltage stability study.

3 POWER SYSTEM MODEL

The differential and algebraic equations are commonly known as a DAE representation of the power system. In this research, they can be denoted as:

$$\dot{x} = f(x, y, z_C, z_D, \lambda) \tag{3.1}$$

$$0 = g(x, y, z_C, z_D, \lambda) \tag{3.2}$$

$$z_D(k^+) = h_D(x(k^-), y(k^-), z_C(k^-), z_D(k^-), \lambda(k)) \tag{3.3}$$

$$\dot{z}_C = h_C(x, y, z_C, z_D, \lambda) \tag{3.4}$$

where x includes transient state variables and y includes algebraic variables, usually network bus voltage magnitudes and angles. The long-term dynamics are captured by discrete and/or continuous-time variables. z_D relates to controls and protecting devices. Note for (3.3), the expression of the change of z_D is due to the implementation of the QSS simulation. z_C originates from the centralized voltage/frequency control representation. λ includes load demand coefficients and the corresponding generation rescheduling during the long-term scale. It is taken as a "smooth" function of time. Table 3.1 [5] shows indicative time scales of various system components and load behaviors taking part in voltage phenomena.

Actually, z_C also includes load state variables. However, in order to explore the influence of OLTCs on voltage stability, the load self-restoration dynamics will not be addressed when we discuss Scenario One. We will present a new method to consider generic load restoration for Scenario Two in Chapter 5.

Here a power system is assumed to have n buses and m generators. Each generator is assumed to be equipped with the same type of excitation control system and speed governor. The specific model of each component of the power system can be mathematically formulated as follows. The commonly used power system notations are adopted here.

Table 3.1 Indicative time scales

Scale	System components	Load
Long-term	On-load tap changers (OLTCs)	thermostatic load restoration
	OvereXcitation limiters (OXLs)	
	switched capacitors/inductors	
	AGC, secondary voltage control	
	small load variation	
Short-term	generators, AVRs, governors	induction motors
	SVCs, HVDC links	
Instantaneous	network	static loads

3.1 Synchronous Generator

Without loss of generality, the rotor angle of the m-th generator is chosen as the system angle reference. No assumptions are necessary for choosing such a reference. When stator transients are ignored, the two-axis model describing the synchronous machine dynamics can be given as:

$$\dot{\delta}_i = (\omega_i - \omega_m)\omega_0 \qquad i = 1, \ldots, m-1 \tag{3.5}$$

$$\dot{\omega}_i = M_i^{-1}[P_{mi} - D_i(\omega_i - \omega_m) - (E'_{qi} - X'_{di}I_{di})I_{qi} - (E'_{di} + X'_{qi}I_{qi})I_{di}] \qquad i = 1, \ldots, m \tag{3.6}$$

$$\dot{E}'_{qi} = T_{d0i}^{-1}[E_{fdi} - E'_{qi} - (X_{di} - X'_{di})I_{di}] \qquad i = 1, \ldots, m \tag{3.7}$$

$$\dot{E}'_{di} = T_{q0i}^{-1}[-E'_{di} + (X_{qi} - X'_{qi})I_{qi}] \qquad i = 1, \ldots, m \tag{3.8}$$

where ω_m is the system frequency, and ω_i is the machine frequency, namely, the generator angular speed, and ω_0 is the system rated frequency (377.0rad/sec). All the quantities are in per unit except ω_0.

Interface voltage equations to the network are given as follows:

$$E'_{qi} = V_i\cos(\delta_i - \theta_i) + R_{si}I_{qi} + X'_{di}I_{di} \qquad i = 1, \ldots, m \tag{3.9}$$

$$E'_{di} = V_i\sin(\delta_i - \theta_i) + R_{si}I_{di} - X'_{qi}I_{qi} \qquad i = 1, \ldots, m \tag{3.10}$$

3.2 Excitation Control System

The simplified IEEE type DC-1 excitation system is used here. The corresponding mathematical model is:

$$\dot{E}_{fdi} = T_{ei}^{-1}[V_{ri} - (S_{ei}(E_{fdi}))E_{fdi}] \qquad i = 1, \ldots, m \tag{3.11}$$

$$\dot{V}_{ri} = T_{ai}^{-1}[V_{ri} + K_{ai}(V_{refi} - V_i - R_{fi})] \qquad i = 1, ..., m \tag{3.12}$$

$$\dot{R}_{fi} = T_{fi}^{-1}[-R_{fi} - [K_{ei} + S_{ei}(E_{fdi})]K_{fi}E_{fdi}/T_{ei} + K_{fi}V_{ri}/T_{ei}] \qquad i = 1, ..., m \tag{3.13}$$

Here V_{refi} is the reference voltage of the Automatic Voltage Regulator (AVR), V_{ri} and R_{fi} are the outputs of the AVR and exciter soft feedback respectively.

3.3 Prime Mover and Speed Governor

Figure 3.1 shows the block diagram for a simplified prime mover and speed governor. Two differential equations are involved to describe the dynamics when no μ_i limit is hit.

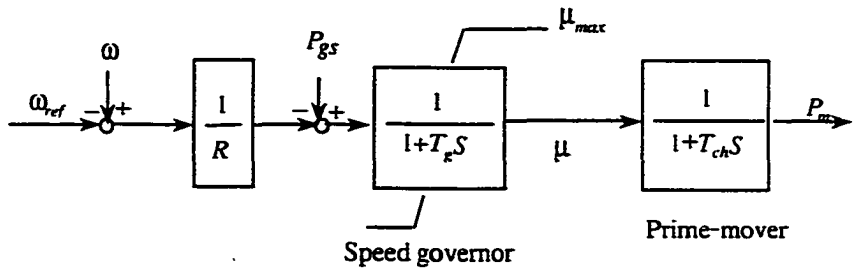

Figure 3.1 The simplified speed governor and prime mover

$$\dot{P}_{mi} = T_{chi}^{-1}(\mu_i - P_{mi}) \qquad i = 1, ..., m \tag{3.14}$$

$$\dot{\mu}_i = T_{gi}^{-1}[P_{gsi} - (\omega_i - \omega_{ref})/R_i - \mu_i] \text{ if } \mu_{i,min} \leq \mu_i \leq \mu_{i,max} \qquad i = 1, ..., m \tag{3.15}$$

where P_{gsi} is the designed real power generation, P_{mi} is the mechanical power of the prime mover and μ_i is the steam valve or water gate opening, R_i is the governor regulation constant representing its inherent speed-droop characteristics, and ω_{ref} (= 1.0) is the governor reference speed.

3.4 Network Power Equations

Corresponding to the above models, the network equations can be written as:

$$0 = P_{gi} - (1 + K_{lpi}\lambda)P_{li} - P_{inji} \qquad i = 1, ..., n \tag{3.16}$$

$$0 = Q_{gi} - (1 + K_{lqi}\lambda)Q_{li} - Q_{inji} \qquad i = 1, ..., n \tag{3.17}$$

where

$$P_{inji} = \sum_{k=1}^{n} V_i V_k Y_{ik} \cos(\theta_i - \theta_k - \varphi_{ik}) \qquad i = 1, \ldots, n \tag{3.18}$$

$$Q_{inji} = \sum_{k=1}^{n} V_i V_k Y_{ik} \sin(\theta_i - \theta_k - \varphi_{ik}) \qquad i = 1, \ldots, n \tag{3.19}$$

and

$$P_{gi} = I_{di} V_i \sin(\delta_i - \theta_i) + I_{qi} V_i \cos(\delta_i - \theta_i) \qquad i = 1, \ldots, m \tag{3.20}$$

$$Q_{gi} = I_{di} V_i \cos(\delta_i - \theta_i) - I_{qi} V_i \sin(\delta_i - \theta_i) \qquad i = 1, \ldots, m \tag{3.21}$$

P_{gi} and Q_{gi} are the generator output powers and P_{inji} and Q_{inji} are the powers injected into the network at bus i. P_{li} and Q_{li} are the load powers at bus i. K_{lpi} and K_{lqi} are load-changing factors specified for bus i.

3.5 Load Tap Changers Model

There are two types of LTC modeling. Assume a transformer with negligible resistance and magnetizing reactance has a constant leakage reactance X_t. The equivalent one-line diagram of the LTC transformer is shown in Figure 3.2 [5] using an ideal transformer with an $r : 1$ ratio.

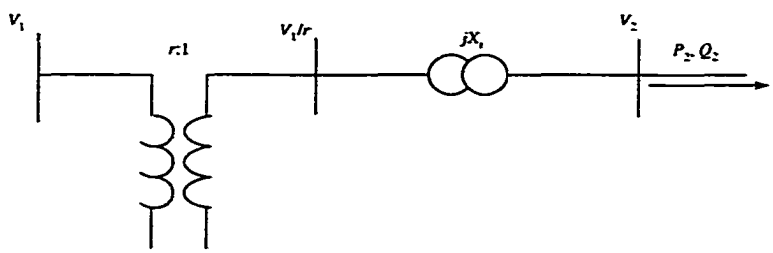

Figure 3.2 Equivalent circuit of an OLTC

Continuous LTC Model: The continuous LTC model, which is often used for the sake of stability analysis, is based on the assumption of a continuously changing tap $r(t)$ that is in the range of r^{min} and r^{max}. It can be represented by using the following differential equation:

$$T_c \dot{r} = V_2 - V_2^0 \qquad r^{min} \leq r \leq r^{max} \tag{3.22}$$

Discrete LTC Model: The discrete LTC model, which is often used for the sake of practical implementation, assumes that when the LTC is activated it will raise or lower the transformer ratio

by one tap step instantaneously. We generally denote the size of each tap step by Δr. The LTC can operate at discrete time instant $t_k, k = 0, 1, ..., n$. Unlike usual discrete-time systems, t_k is not an independent variable, and ΔT_k is not necessarily constant. A universal formula for ΔT_k including fixed and inverse-time delays is the following:

$$\Delta T_k = T_d \frac{d}{|V_2 - V_2^0|} + T_f + T_m \tag{3.23}$$

where V_2 is the controlled voltage, V_2^0 is the reference voltage, and d is half the LTC deadband. T_d is the maximum time delay of the inverse-time characteristics. T_f is the fixed intentional time delay, and T_m is the mechanical time necessary to perform the tap change.

The tap changing logic at time instant t_k is the following:

$$r_{k+1} = \begin{cases} r_k + \Delta r & \text{if } V_2 > V_2^0 + d \text{ and } r_k < r^{max} \\ r_k - \Delta r & \text{if } V_2 < V_2^0 - d \text{ and } r_k > r^{min} \\ r_k & \text{otherwise} \end{cases} \tag{3.24}$$

where r^{max} and r^{min} are the upper and lower tap limits.

3.6 Generic Load Model

All the models are voltage and frequency dependent. However, in a voltage stability problem, the frequency dependent part of the load model usually is omitted. The generic load models are associated with an exponential type of voltage characteristic. The short-term (transient) and long-term (steady-state) load characteristics can be expressed as follows:

$$P_t = P_t(P_{t0}, V, z_P) \tag{3.25}$$

$$Q_t = Q_t(Q_{t0}, V, z_Q) \tag{3.26}$$

$$P_s = P_t(P_{t0}, V) \tag{3.27}$$

$$Q_s = Q_t(Q_{t0}, V) \tag{3.28}$$

where P_{t0} and Q_{t0} are the *load demands* which have been defined in Chapter 1. They are the powers absorbed by the load at the nominal voltage V_0. z_P and z_Q are the load internal state variables associated with load dynamics. Details of the load model, which is very important in this research, will be given in Chapter 5. As mentioned before, P_t is not an independent variable in the above model.

3.7 Concluding Remarks

The mathematical equations representing the power system model under consideration have been described. The short-term state variables x, algebraic variables y, discrete-type long-term state variables z_D and continuous-type long-term state variables z_C as well as load parameter λ are given as follows:

$$x = (\delta, \omega, E_q', E_d', P_m, \mu, E_{fd}, V_r, R_f) \tag{3.29}$$

$$y = (V, \theta) \tag{3.30}$$

$$z_D = (r_k) \tag{3.31}$$

$$z_C = (z_P, z_Q) \tag{3.32}$$

$$\lambda = \lambda(t)$$

The work in the following chapters will be focused on the discussion of the system DAE formulation.

QSS analysis in the long-term scale in Chapter 4 focuses on using continuation method to solve this set of equations as well as the consideration of z_D. The approximation of the load restoration procedure relating to z_C will be discussed in Chapter 5. Chapter 6 deals with trajectory sensitivity, which is derived from the sensitivity analysis of the general DAE system. Trajectory sensitivity is calculated to obtain the useful information of the system's state variable with respect to different control measures as well as to check the system's long-term instability.

4 CONTINUATION-BASED QUASI-STEADY-STATE ANALYSIS

4.1 Introduction to Quasi-Steady-State Analysis

We have been given the components, phenomena, controllers and protecting devices which play a role in voltage stability, according to the time scale of the corresponding dynamics.

In stability analysis, an instantaneous response is assumed for the network, according to the quasi-sinusoidal (of fundamental-frequency) assumption. The network is thus depicted by the algebraic equation $g(x, y, z_D, z_C, \lambda) = 0$ derived from the Kirchhoff's current law at each bus, and involving the vector y of bus voltage magnitudes and phase angles.

The long-term components, acting typically over several minutes, may be represented either through discrete-time equations (e.g. shunt switched capacitors and OLTC operations) or through continuous-time equations (e.g. generic load models). Specific approaches should be developed to deal with these equations in a reasonable and efficient way.

Before discussing the voltage stability in the long-term time scale, we will briefly address the short-term dynamics which last typically for several seconds following a disturbance in stability analysis, as we assume that the short-term stability has been achieved before the long-term stability.

In [38], an attempt is made to distinguish the difference between voltage and angle instability. Although the final outcome of the scenario is a loss of synchronization, the initializing event is load restoration in the long-term time scale. Therefore it is justified to classify this as a voltage stability problem. The dynamic analysis tool such as EPRI's Extended Transient/Midterm Stability Program (ETMSP) which uses time-domain simulations to solve the transient angle stability problem also is suitable for the voltage stability analysis in the short-term period. It can model devices which are important for voltage stability such as OLTCs, OXLs, thermostatical loads and induction motors as well as some special control system models. When voltage instability is ensured not to happen during the transient period by using ETMSP, (which means the base case for the long-term time-scale simulation has been successfully established) QSS fast simulation of voltage stability comes into play.

Quasi-Steady-State simulation has been widely used to speed up long-term voltage stability calcu-

lations, which filters out the short-term transients.

Van Cutsem [28] proposed the general idea of QSS analysis, which consists of approximating the long-term time evolution by a succession of short-term equilibrium points. thereby offering a good compromise between load-flow-type methods and full time domain methods. The central idea is simple and intuitively appealing: it deals with the long-term subsystem of the DAEs based on the assumption that the transient subsystem is infinitely fast and can be replaced by its equilibrium equations. Load restoration following some disturbances mainly depends on OLTC transformers. This method is applied to trace the system's equilibrium for Scenario Two and is a good diagnostic tool for corrective control. However, the original QSS simulation encounters numerical difficulties when the system approaches the SIB point. In order to overcome this problem, continuation method is applied to solve the system equations as well as to consider Scenario One conveniently.

QSS simulation has been thoroughly validated with respect to full time domain simulation. It has been found more than 1000 times faster than the numerical integration using the Trapezoidal Rule with a fixed time step size, while offering comparable accuracy in terms of security limits. On the EDF system, it has also been effectively implemented and validated. with respect to the full time simulation software EUROSTAG [39]. EUROPSTAG is a comprehensive simulation tool for the multi-time scale calculation. It is very useful when not only long-term dynamics but also short-term dynamics are considered in the power system analysis. The detailed introduction can be found in [40, 41, 42, 43, 44].

In this research, the dynamic characteristics of generators and their control systems are completely considered. Combined with the parameterized continuation technique, the methodology identifies voltage collapse during the equilibrium tracing while the OLTC is activated to restore the load indirectly (Appendix E). In Scenario One, the system's load is increased according to the defined scenario after it is fully restored to the pre-contingency level. At the same time, OLTC tries to maintain the voltage of the load bus within some tolerance. The driving force of voltage collapse is not only the load restoration activated by the OLTCs but also the increase of the load level, which may be more important during this process. Due to continuation method, the singularity checking of the Jacobian matrix could be eliminated. which significantly reduces the computational cost. Moreover, all the unrealistic assumptions for the slack bus and PV buses are totally removed, except for the initialization of system control settings at base case. The system's limits, which often lead to voltage collapse, are considered. It is important to note that the generator field and armature current limits are explicitly taken into account in our framework.

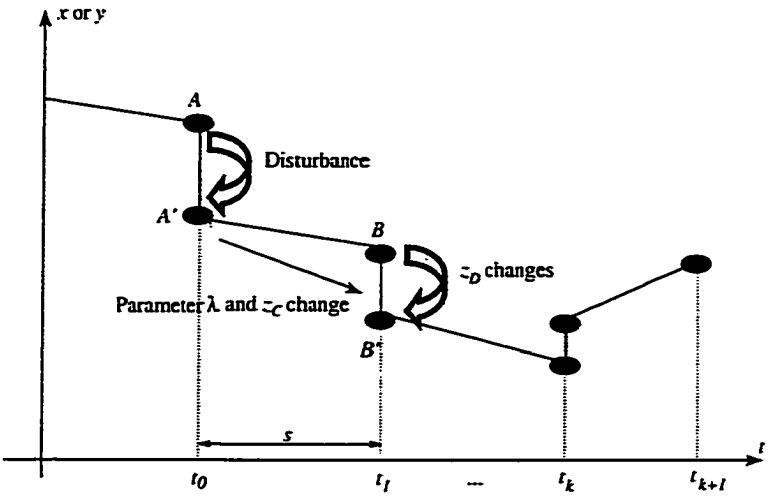

Figure 4.1 Illustration of Quasi-Steady-State simulation

As we focus on the long-term voltage instability, $\dot{x}$ in (3.1) is replaced by the equilibrium equation:

$$0 = f(x, y, z_D, z_C, \lambda) \tag{4.1}$$

From there on, the system's evolution is dictated by the long-term time dynamics (3.3-3.4) and the change of λ. This suggests the simplified simulation method outlined in Figure 4.1, which describes the time evolution of an x or y variable. Assume the disturbance at t_0, then:

- Point A is an equilibrium of (4.1) and (3.2) before the disturbance.
- Point A' is an equilibrium of (4.1) and (3.2) after the disturbance.
- At A', predict the next transition time s that is the shortest internal delay or sampling period among various discrete-type long-term components. In this research, it is dictated by the built-in delays of the OLTCs.
- The continuous change from A' to B results from the evolution of λ and/or z_C. Time integration may be required.
- The transition from B to B' is from the discrete change of z_D. Newton method for solving the new equilibrium is applied here.

The computational steps involved here are explained as follows:

At $t = t_0^-$,

$$\begin{aligned} 0 &= f(x_0^-, y_0^-, z_{C0}, z_{D0}, \lambda_0) \\ 0 &= g(x_0^-, y_0^-, z_{C0}, z_{D0}, \lambda_0) \\ 0 &= h_D(x_0^-, y_0^-, z_{C0}, z_{D0}, \lambda_0) \\ 0 &= h_C(x_0^-, y_0^-, z_{C0}, z_{D0}, \lambda_0) \\ \lambda_0 &= \lambda(t_0) \end{aligned}$$

At $t = t_0^+$, new equilibrium point $(x_0^+, y_0^+, z_{C0}, z_{D0}, \lambda)$ exists where

$$\begin{aligned} 0 &= f(x_0^+, y_0^+, z_{C0}, z_{D0}, \lambda_0) \\ 0 &= g(x_0^+, y_0^+, z_{C0}, z_{D0}, \lambda_0) \\ 0 &\neq h_D(x_0^+, y_0^+, z_{C0}, z_{D0}, \lambda_0) \\ 0 &\neq h_C(x_0^+, y_0^+, z_{C0}, z_{D0}, \lambda_0) \\ \lambda_0 &= \lambda(t_0) \end{aligned}$$

If $t_0 < t < t_1$, keep updating λ and/or z_C. Numerical integration method may be used here. Solve

$$\begin{aligned} 0 &= f(x_1^-, y_1^-, z_{C1}, z_{D0}, \lambda_1) \\ 0 &= g(x_1^-, y_1^-, z_{C1}, z_{D0}, \lambda_1) \end{aligned}$$

with initial guess $(x_{1(0)}^-, y_{1(0)}^-) = (x_0^+, y_0^+)$.

At $t = t_1$, fix $\lambda_1 = \lambda(t_1)$ and z_{D0} becomes z_{D1}. Solve

$$0 = f(x_1^+, y_1^+, z_{C1}, z_{D1}, \lambda_1) \tag{4.2}$$

$$0 = g(x_1^+, y_1^+, z_{C1}, z_{D1}, \lambda_1) \tag{4.3}$$

with initial guess $(x_{1(0)}^+, y_{1(0)}^+) = (x_1^-, y_1^-)$. The discontinuity from B to B' results from solving (4.2) and (4.3) iteratively with $(z_{C1}, z_{D1}, \lambda_1)$ fixed. Newton method is applied, which is:

$$\underbrace{\begin{bmatrix} f_x & f_y \\ g_x & g_y \end{bmatrix}}_{J_{xy}} \begin{bmatrix} x_{1(j)}^+ - x_{1(j-1)}^+ \\ y_{1(j)}^+ - y_{1(j-1)}^+ \end{bmatrix} = \begin{bmatrix} -f(x_{1(j-1)}^+, y_{1(j-1)}^+, z_{C1}, z_{D1}, \lambda_1) \\ -g(x_{1(j-1)}^+, y_{1(j-1)}^+, z_{C1}, z_{D1}, \lambda_1) \end{bmatrix} \tag{4.4}$$

QSS simulation considers (x, y) and z variables separately. The Jacobian matrix J_{xy} only involves the derivatives of (f, g) with respect to (x, y). When a system approaches the bifurcation point, J_{xy}

becomes more and more ill-conditioned. This may result in a long simulation time or a divergent solution before the Jacobian actually becomes singular. Continuation method is well-suited for dealing with such problems. It remains feasible over the entire solution path even at the bifurcation point by choosing an appropriate continuation parameter. In this chapter, we are proposing a numerically well-conditioned continuation method to solve (4.4).

Since transient dynamics are neglected, no numerical integration is needed. Also, because λ is supposed to vary smoothly with the time, it is not considered when predicting the next transition time. Based on the appropriate step-size selection, it changes according to the predictor-corrector scheme of the applied continuation method. This will be discussed in detail later.

Furthermore, in QSS simulation, there is no point in detecting very exactly when the discrete transitions take place. Rather, discrete transitions are "synchronized" at times dictated by the time step size which results in the formulation of (3.3). Decreasing time step tends to cancel this synchronization but may be of interest for a finer analysis of numerous interacting OLTCs. Increasing time step obviously delays some transitions and the choice to do so depends on the various purposes of the analysis.

All these characteristics ensures that the method is computationally efficient while able to render the long-term sequence of events and provide the transient-free "snapshots" required for the voltage stability analysis.

Van Cutsem considers OLTC dynamics by changing z_D and thermostatic load restoration by integrating z_C. However, the change of $\lambda(t)$ and its effects on voltage stability have not been addressed. Moreover, if z_C could be taken into account with no numerical integration, this method would be very computationally efficient. Chapter 4 proposes a methodology that combines the effects of the OLTCs and the load change on voltage stability. Chapter 5 provides a new approach for load restoration that avoids the numerical integration.

4.2 Equilibrium Tracing by Continuation Technique

Feng et al. [45] made an attempt to further extend the application of the continuation method described in [46] to the power system DAE formulation.

By using continuation technique, we can:

- Simultaneously solve the system DAEs and obtain all the system's variables in one step so that the assumptions for the slack bus and PV buses are eliminated;
- Directly identify the system's voltage collapse point during the tracing process;

- Produce the true system stability information.

Based on the power system model (3.1-3.4) introduced before, continuation method is also applied to trace the equilibrium of long-term dynamics. Prediction and correction are two basic procedures in this methodology. In the prediction stage, the tangent vector is solved from:

$$-\begin{bmatrix} f_x & f_y & f_\lambda \\ g_x & g_y & g_\lambda \\ & e_k^T & \end{bmatrix}\begin{bmatrix} dx \\ dy \\ d\lambda \end{bmatrix} = \begin{bmatrix} 0 \\ 0 \\ \pm 1 \end{bmatrix} \tag{4.5}$$

After the prediction is made with the tangent vector, the following correction is performed to find the equilibrium point:

$$-\begin{bmatrix} f_x & f_y & f_\lambda \\ g_x & g_y & g_\lambda \\ & e_k^T & \end{bmatrix}\begin{bmatrix} \Delta x \\ \Delta y \\ \Delta\lambda \end{bmatrix} = \begin{bmatrix} f \\ g \\ 0 \end{bmatrix} \tag{4.6}$$

where $[dx \;\; dy \;\; d\lambda]^T$ is the tangent vector. e_k^T is a row unit vector with all the elements equal to zero except for the k-th one, which corresponds to the current continuation parameter.

Since f_λ and g_λ can't be null vectors at the same time even at the base case where $\lambda = 0$, the singularity of the augmented Jacobian matrix can be easily avoided by appropriately selecting the continuation parameter. To efficiently implement the limits and speed up the computation, the fixed-structured Jacobian is used in (4.5) and (4.6).

In (4.5), it is shown that the component of tangent vector actually indicates some kind of sensitivity of system variables to the current continuation parameter. Usually, such sensitivity can be used to identify the system's bifurcation point [28]. Moreover, since λ is introduced to parameterize the system's generation and load level, it changes with the time. $d\lambda$ is positive before λ reaches its maximum, and negative afterwards. Null $d\lambda$ indicates the singularity of J_{xy}. From a detailed analysis of the system's total Jacobian and reduced system state matrices in different time scales (Appendix A), we know that the singularity identified by null $d\lambda$ corresponds to the singularity induced bifurcation [11]. However, the original QSS simulation can't identify it during the tracing. Furthermore, trajectory sensitivity proposed in Chapter 6 could detect the true long-term saddle node bifurcation in the CQSS simulation.

4.3 Device Limits Implementation in Equilibrium Tracing

Voltage collapse often occurs as a consequence of some devices hitting their limits in a heavily stressed power system. Therefore it is very important to adequately address system limits in the voltage stability

study. For a synchronous generator, its real power output limit, armature current limit and field current limit, are especially critical on the voltage stability. In this work, we take full advantage of the DAE formulation to accurately implement all these three limits.

The reactive power output of a generator is dependent on its terminal voltage, which is controlled by the generator AVR. Hence under normal conditions, the generator reactive power output can be adjusted by regulating the AVR reference voltage. However, once the generator field current limit is reached, the AVR will lose its ability to maintain the generator terminal voltage, and the reactive power output can no longer be regulated. In [45], it has been shown that the field current limit and the armature current limit both could be accurately represented by implementing the AVR output limits $V_{ri,max}$.

From the model we applied in this research, it can be concluded that the state variable V_{ri} (AVR output) is proportional to the generator field current. Thus the field current limit $I_{fd,max}$ can be directly implemented by enforcing the fixed AVR output limit.

The maximum limit for the generator reactive output with respect to the armature current limit can be determined as:

$$Q_{gi,max} = \sqrt{V_i^2 I_{ai,max}^2 - P_{gi}^2} \tag{4.7}$$

Therefore, when the current reactive power output Q_{gi} is greater than its allowed limit $Q_{gi,max}$, it means that the armature current limit has been exceeded. To keep the armature current below its limit, we can impose the AVR output limit to reduce the reactive power output.

Since the system's equilibrium solution varies when the AVR output limit is enforced, an iterative scheme is applied to update $V_{ri,max}$ at each continuation step so that the armature current can stay within limit.

Once the AVR reaches its output limit, either due to the generator field current limitation or due to the armature current limitation, the state variable V_{ri} will immediately become a control input staying at its maximum value. The closed-loop control becomes an open-loop control. Accordingly, the corresponding equation should be dropped. The Jacobian matrix for equilibrium computation also needs to be modified by removing one row and one column. Similar modifications are needed when a governor hits its output limit.

Obviously, null $d\lambda$ still signifies the system's singularity even after the AVR and governor limits are reached. Actually, the proposed approach can handle any device limit as long as the limit can be enforced by limiting a variable that explicitly appears in (3.2) and (4.1).

4.4 Consideration of Load Change with Respect to Time

It is known that QSS analysis separates the whole DAEs of power system to two-step implementation: the first step is to solve the equilibrium of the fast-dynamics ((3.2) and (4.1)) with respect to x and y and the second is related to long-term dynamics where the time step change is considered. More specifically, in this time step, z_D is updated according to some control logic practiced in the power system. In Figure 4.1, the transition time step $t_{k+1} - t_k$ is determined by the shortest internal delay or sampling period of the long-term control and protecting devices (z_D), such as OLTCs. Continuation method introduces the load level λ as continuation parameter to easily trace the system's equilibrium. The physical meaning of λ represents the influence of the load change on the system's voltage stability. During the time process dictated by OLTC actions, the load also varies according to its time-characteristics. Its time function is indicated as $\lambda(t)$ in the CQSS analysis. An approach should be found to appropriately consider how λ changes in the determined time interval $t_{k+1} - t_k$, so as to meet its time function both at t_k and t_{k+1}.

As known before, the implementation of continuation method depends on the following factors:

- Predictor
- Corrector
- Step size control

The prediction and correction at time step t_k can be made respectively as follows:

$$(\overline{x}_{k+1}, \overline{y}_{k+1}, \overline{\lambda}_{k+1}) = (x_k, y_k, \lambda_k) + \sigma_k * [\ dx \quad dy \quad d\lambda\ ]^T \tag{4.8}$$

$$(x_{k+1}, y_{k+1}, \lambda_{k+1}) = (\overline{x}_{k+1}, \overline{y}_{k+1}, \overline{\lambda}_{k+1}) + [\ \Delta x \quad \Delta y \quad \Delta\lambda\ ]^T \tag{4.9}$$

If λ is taken as continuation parameter, then $\Delta\lambda$ is equal to zero in the correction stage. Furthermore, λ_{k+1} and λ_k have been known according to its time function and the transition time step $t_{k+1} - t_k$ decided by z_D. Then the step size σ_k can be obtained as follows:

$$\sigma_k = (\lambda_{k+1} - \lambda_k)/d\lambda \tag{4.10}$$

At each time step, this step size should be re-calculated to fit the load variation in this period.

When the current operating point of the system is very close to the SNB point, the choice of continuation parameter will be one of the x or y variables in order to avoid the divergence of the simulation. Then the calculation of the step size σ_k will be a little different. From (4.8) and (4.9),

$$\overline{\lambda}_{k+1} = \lambda_k + \sigma_k * d\lambda \tag{4.11}$$

$$\lambda_{k+1} = \overline{\lambda}_{k+1} + \Delta\lambda \tag{4.12}$$

where $d\lambda$ and $\Delta\lambda$ can be obtained from the predictor and corrector stage respectively. From (4.11) and (4.12),

$$\lambda_{k+1} = \lambda_k + \sigma_k * d\lambda + \Delta\lambda \tag{4.13}$$

Therefore, the equation for computing $sigma_k$ is written as:

$$\sigma_k = \frac{\lambda_{k+1} - \lambda_k - \Delta\lambda}{d\lambda} \tag{4.14}$$

In fact, it is the common formula for calculating the general step size in continuation method. Note that the Jacobian used in the corrector stage depends on the state variables obtained from the predictor stage. However, in order to apply $d\lambda$ and $\Delta\lambda$ to compute the step size, the same Jacobian is used in both the predictor and the corrector at first. After the approximate step size is obtained, we update the Jacobian in the corrector, get the new $\Delta\lambda$ by solving (4.6) and calculate the step size again by using (4.14). This procedure will be repeated until the error between the updated $\Delta\lambda$ and the old one is within some tolerance. By this approach, the change of the load level with the time can be successfully considered in continuation method.

4.5 CQSS Simulation for Scenario One on a Small Test System

Next, we will show the relevant numerical results on a small test system step by step from Chapter 4 to Chapter 7. This small system provides a better and clearer understanding of the proposed method in each chapter. In Chapter 8, the whole simulation procedure, with all the relevant steps, will be demonstrated on the New England system to give the complete scope of this work. In this chapter, the configuration of a small test system and simulation results for Scenario One are presented first.

4.5.1 Test System

The one-line diagram of this small system is shown in Figure 4.2 [5]. The parameters of this system are presented in Table 4.1 and 4.2.

Between Bus1 and Bus4, there are a total of four lines. Each of them has the same reactance. The power factor for the generators and the load, is the same, 0.9975. The system model is introduced in Chapter 3.

4.5.2 QSS Simulation for Scenario One

The disturbance simulated for Scenario One is the three-line tripping between Bus1 and Bus4. Before the contingency, the system's total load is $P = 2700MW$. The post-contingency system load

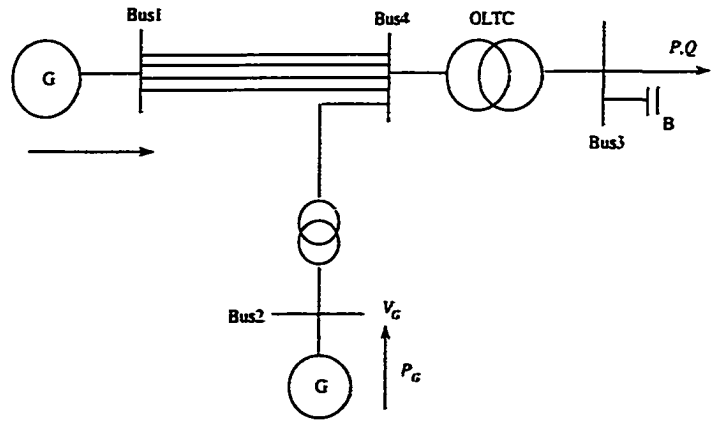

Figure 4.2 One-line diagram of a small test system [5]

Table 4.1 Bus data of the small test system

Bus no.	Bus type	$V(p.u.)$	θ	Shunt$(p.u.)$
Bus1	slack	1.08	0.00	0
Bus2	PV	1.01	-11.22	0
Bus3	PQ	1.00	-13.88	6
Bus4	PQ	1.00	-14.02	0

Table 4.2 Branch data of the small test system

From bus	To bus	Branch type	$X(p.u.)$	r	r^{min}	r^{max}
1	4	0	0.027700	0.0000	0.0000	0.0000
2	4	1	0.016000	1.0400	0.0000	0.0000
4	3	2	0.004000	1.0000	0.8000	1.1000

is $P = 2460MW$ due to the constant impedence load characteristic at Bus3. The load self-restoration mechanism is not considered and only the OLTC's actions to restore the voltage are taken into account. For this system, the initial fast transient caused by the disturbance dies out soon after, showing that the short-term dynamics are stable. Thus a short-term equilibrium is first established, with V_4 settling down to $0.9437p.u.$.

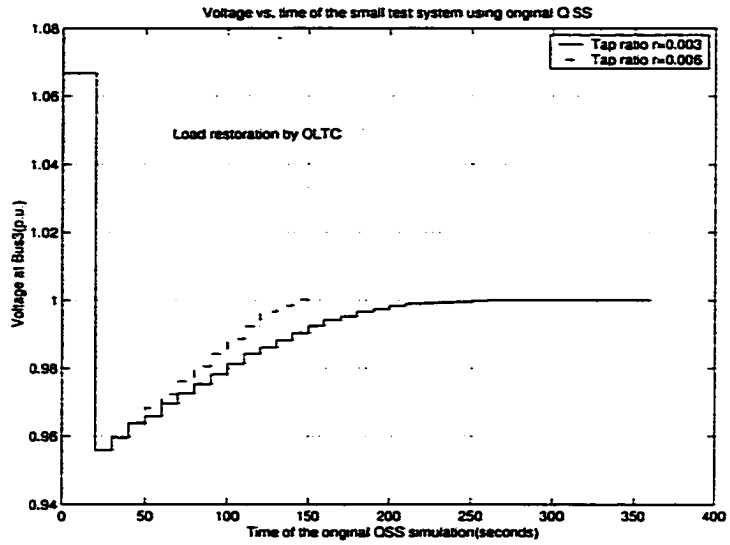

Figure 4.3 Voltage vs. time by using the original QSS simulation

For this contingency, the voltage curve at Bus3 is shown in Figure 4.3 by using the original QSS simulation. At first, the post-contingency base case is successfully established, which shows that the voltage at Bus3 has declined. At $t = 20s$, the OLTC is activated to restore the load to the pre-contingency value. However, when the load is fully recovered, the system reaches a stable long-term equilibrium and the voltage at Bus3 is well maintained around the reference value. In the figure, two curves represent different tap step sizes. The smaller the step size, the longer the time the system takes to recover. After the load restoration has been accomplished by the OLTC, the system will settle down at B' (Figure 1.2 in Chapter 1).

4.5.3 CQSS Simulation for Scenario One

4.5.3.1 Equilibrium tracing: λ as continuation parameter

In order to find the system's SNB point, we will increase the load continuously afterwards. The system's slow evolution to this point is considered in two steps. Therefore, combined with the continuation method, the original QSS simulation will be modified as follows:

- **Step One: During the load restoration**

  After the contingency, the OLTC tries to restore the voltage at Bus3. Figure 4.4 shows the voltages at Bus3 and Bus4 before the complete restoration is achieved. It can be observed that the voltage at Bus3 gradually increases due to the OLTC's actions. Note here, the larger step size of the OLTC's ratio is used from the original QSS simulation. At $t = 140s$, the system's load level returns to its pre-contingency value, which also means that the load model becomes constant power to some extent. Voltages at buses other than Bus3 decrease according to the restored load. Up to this point, if there is no other interruption in the system, it could be concluded that the system has reached its long-term equilibrium. The OLTC also reaches its steady state.

- **Step Two: After the complete restoration**

  After the restoration, other slow dynamics, namely, load change with respect to time, may drive the system to instability. It is assumed that the system's total real power load increases by $5MW$ at time interval $t = 5s$ for the simulation. Two generators pick up the load by the same participation factor as the base case. By adjusting the step size in the predictor, we can trace the system's trajectory continuously. Table 4.3 gives the different real power loads of the system at different time steps. While the load increases slowly, V_3 drops. Then the OLTC is re-activated and tries to regulate the voltage variation. Figure 4.5 shows the voltage curves with respect to time after the complete restoration is achieved. At first, the OLTC could maintain the voltage very well. However, when the generators reach their limits at $t = 470s$, the OLTC's capability on the voltage regulation is significantly weakened even though it is within the limits.

When using the CQSS simulation, we can obtain the PV curves shown in Figure 4.6. It is clear that the system reaches the SNB point due to the load increase, though the OLTC attempts to keep the voltage at Bus3 unchanged.

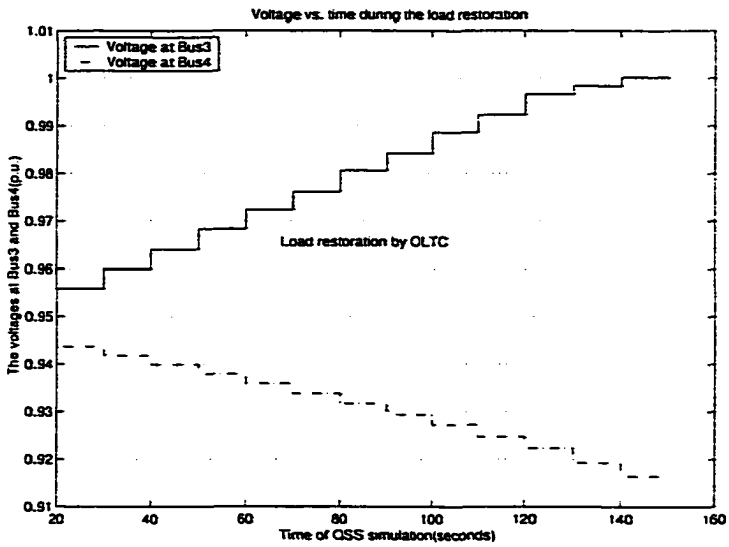

Figure 4.4 Voltage change vs. time during the load restoration

Table 4.3 Step size based on the load increase

Time(s)	$P_l(MW)$	Step size
150	2720.00	0.4876
200	2770.00	0.4723
250	2820.00	0.4432
300	2870.00	0.4273
350	2920.00	0.3992
400	2970.00	0.3227

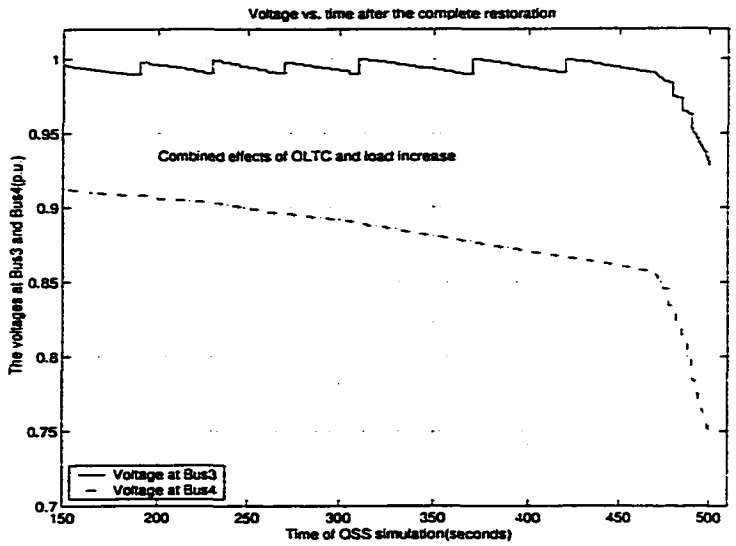

Figure 4.5 Voltage change vs. time after the complete restoration

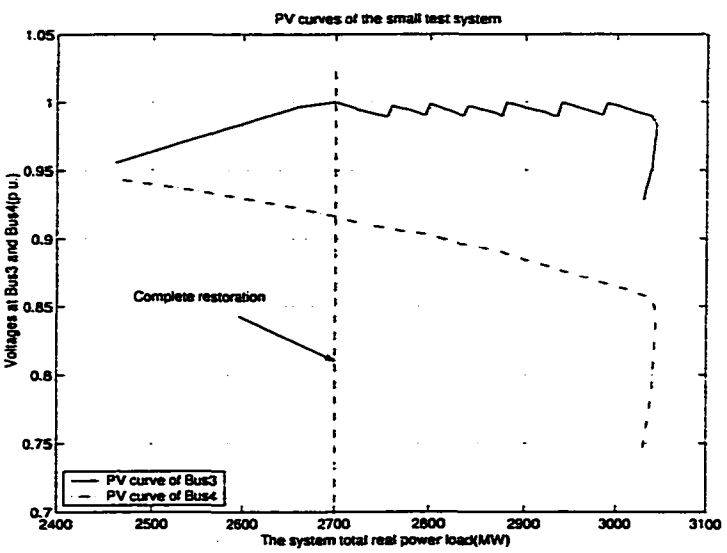

Figure 4.6 PV diagram by using the CQSS simulation

4.5.3.2 Bifurcation identification by continuation parameter

For the CQSS simulation based on load parameter λ. two methods can be used to identify the bifurcation points. In this chapter. first continuation parameter is applied. As discussed before. null $d\lambda$ implies J_{xy} singular and actually represents the singularity-induced bifurcation of the system.

Usually. we use a relatively large step size to trace the system's equilibrium point until the negative $d\lambda$ is detected at an operating point. then change the tracing direction and continue the process with a smaller step size up to the upper portion of the PV curve where a very small positive $d\lambda$ could be easily detected. Table 4.4 shows the values of $d\lambda$ in the last five steps. In these steps. one state variable other than λ is selected as the continuation parameter. These values indicate that null $d\lambda$ has been reached between $t = 475s$ and $t = 480s$.

Table 4.4 $d\lambda$ in the last five steps

Time(s)	460	465	470	475	480
$d\lambda$	0.023164	0.023086	0.022971	0.022883	-0.023634

4.6 Concluding Remarks

The basic idea of the CQSS simulation has been introduced in this chapter. The consideration of the load change with respect to time has been solved through the selection of the step size. In this chapter. we concentrate only on using continuation method to deal with z_D. Load restoration represented by z_C in the long-term voltage dynamics will be addressed in the next chapter.

5 A NEW APPROACH TO LOAD RESTORATION

5.1 Introduction to Load Restoration

In the last few years, many research efforts have been devoted to developing steady-state and dynamic models for aggregate loads [47, 48, 49, 50, 51, 52, 53]. However, there still exist problems of accurately modeling the loads due to several reasons which include:

- Large number of load components;
- Some load devices not directly accessible to the electric utility;
- Changing load composition with time of day, week, seasons, weather, and through time;
- Lack of precise information on the composition of the load;
- Uncertainties regarding the characteristics of many load components, particularly for large voltage or frequency variations.

Additionally, one of the approaches in voltage stability studies that appears the most promising, is the evaluation of the system's response to typical perturbations, such as a line tripping or a generator outage, especially when the system is close to critical conditions. For such a contingency, the dynamics of various load components and control mechanisms tend to restore load power to a certain level. This process is referred to as load restoration. Figure 5.1 shows the general procedure of the load restoration by PV diagram and Figure 5.2 [50] shows the load response with respect to time.

In the load restoration simulation, loads are generally treated as smooth differential equations, where the power consumed by the load at any time depends upon the instantaneous value of a load state variable. Often, the steady-state load dynamics are characterized by algebraic equations, which do not depend on the load state variable. The transition from transient (short-term) load characteristics towards the steady-state (long-term) load characteristics is driven by load dynamics. Typical dynamic load components with the state and demand variables, include induction motors, loads behind OLTCs and thermostatic loads.

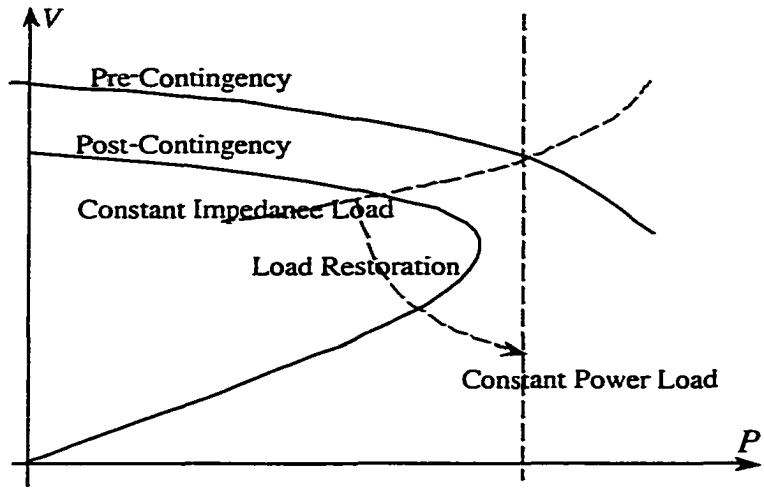

Figure 5.1 Illustration of load restoration by PV diagram

Quasi-Steady-State analysis sometimes incorporates thermostatic load self-restoration (Appendix H) which is represented by the differential equation associated with z_C in the long-term time scale. The equilibrium of the system's fast dynamics should be recalculated after the integration of the load state variable, which may significantly increase the computation burden since one more equilibrium is calculated. Furthermore, discrete transitions are "synchronized" at times dictated by the step size while the continuous-type components change during the whole transition period defined by the time step. These two types of variables on the same time scale are considered alternatively. Finally, the singularity-induced bifurcation [11] encountered in the simulation can't be readily identified by the original QSS analysis. In this research, we propose a new way to consider load restoration by introducing continuation method. It eliminates the need to include the differential equation in the simulation and simplifies the whole tracing procedure. In addition, the equilibrium of fast dynamics is calculated only once. The continuous type component and discrete transition are considered simultaneously after updating the discrete type variable and reforming the Jacobian matrix. Moreover, the SIB point will be easily found by the change of the continuation parameter.

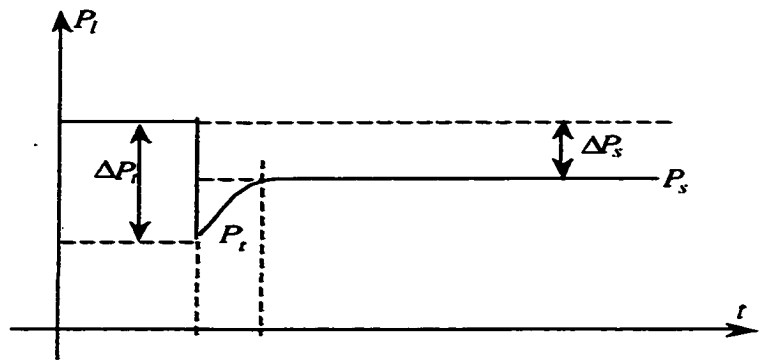

Figure 5.2 Load restoration vs. time

5.2 Consideration of Load Restoration in Quasi-Steady-State Analysis

The power consumed by the additive load model in the short term (P_t) is given by [5] for QSS analysis:

$$P_l = P_{l0}((\frac{V}{V_0})^{\alpha_T} + z_P) \tag{5.1}$$

$$Q_l = Q_{l0}((\frac{V}{V_0})^{\beta_T} + z_Q) \tag{5.2}$$

For the long-term time scale, the load characteristic (P_s) becomes:

$$P_l = P_{l0}(\frac{V}{V_0})^{\alpha_S} \tag{5.3}$$

$$Q_l = Q_{l0}(\frac{V}{V_0})^{\beta_S} \tag{5.4}$$

The following equations [5] depict the generic load restoration dynamics:

$$T_P \dot{z}_P = -z_P + (\frac{V}{V_0})^{\alpha_S} - (\frac{V}{V_0})^{\alpha_T} \tag{5.5}$$

$$T_P \dot{z}_Q = -z_Q + (\frac{V}{V_0})^{\beta_S} - (\frac{V}{V_0})^{\beta_T} \tag{5.6}$$

Usually, the additive model is initialized with $z_P = z_Q = 0$. When the loads reach the steady state,

$$z_P = (\frac{V}{V_0})^{\alpha_S} - (\frac{V}{V_0})^{\alpha_T} \tag{5.7}$$

$$z_Q = (\frac{V}{V_0})^{\beta_S} - (\frac{V}{V_0})^{\beta_T} \tag{5.8}$$

where α_S, α_T, β_S and β_T are load exponents in different time scales.

In this thesis, a continuation-based approach will be proposed to deal with the load restoration in QSS simulation instead of using differential equations (5.5) and (5.6). It will be shown that this method is not only physically reasonable but also numerically efficient. First, we look for the reason why the proposed method could be applied here.

The sensitivities of real and reactive powers with respect to voltage can be obtained respectively as in [5]:

$$\frac{dP_l}{dV} = \alpha P_{l0}(\frac{V}{V_0})^{(\alpha-1)}\frac{1}{V_0} \tag{5.9}$$

$$\frac{dQ_l}{dV} = \beta Q_{l0}(\frac{V}{V_0})^{(\beta-1)}\frac{1}{V_0} \tag{5.10}$$

By rearranging the above expression and evaluating the sensitivity at $V = V_0$, we can find:

$$\frac{dP_l/P_{l0}}{dV/V_0} = \alpha \tag{5.11}$$

$$\frac{dQ_l/Q_{l0}}{dV/V_0} = \beta \tag{5.12}$$

Thus the normalized sensitivity of real or reactive power with respect to voltage is equal to the corresponding load exponent by using the exponential load model. Generally, the load exponents α_T and β_T are larger than α_S and β_S, which means that the transient characteristic of the load is more voltage sensitive. It further implies that the sensitivity of the load power to voltage varies continuously during the load restoration procedure. In some sense, the load obeys an exponential model that changes from the transient α_T to the steady-state α_S exponent. In practice, the aggregate behavior of a number of thermostatic loads has a transient voltage characteristic with an exponent of two (constant impedance), whereas after some time the steady-state voltage characteristic is close to constant power.

If load dynamics are considered completely, the differential equation related to the load state variable should be analyzed and included in QSS simulation. Numerical integration is used to solve the whole system DAEs. However, QSS analysis gives "snapshots" of the equilibrium of fast dynamics instead of the smooth solution curve of the differential and algebraic equations. Compared to the OLTC action, thermostatic load restoration belongs to "slow dynamics" even though both of them are treated in the same time scale. We assume that at each short-term equilibrium, the load dynamics still stay in a time-dependent exponential state, so that we need not monitor the change of the load state variable by integrating its differential equation. If load restoration is considered as a procedure in which sensitivities change with the time, the following equations are proposed to describe it:

$$P_l = P_{l0}(\frac{V}{V_0})^{\alpha(t)} \tag{5.13}$$

$$Q_l = Q_{l0}(\frac{V}{V_0})^{\beta(t)} \tag{5.14}$$

where $\alpha_S \leq \alpha(t) \leq \alpha_T$ and $\beta_S \leq \beta(t) \leq \beta_T$.

At each time step where the equilibrium of the system's fast-dynamics is found, the exponential load model at this equilibrium is also assumed. In (5.13) and (5.14), there is no z_P and z_Q. However, the load dynamics still need to be considered while computing $\alpha(t)$ and $\beta(t)$ in the simulation.

D. J. Hill et al. solved the load state variable as a time dependent exponential function. Based on their derivations, we will show how to relate (5.13) and (5.14) to the original differential equations (5.5) and (5.6). In [50] and [51], another form of the additive load model is given as below:

$$T_P\dot{P}_l + P_l = P_S(V) + k_P(V)\dot{V} \tag{5.15}$$

Setting derivatives to zero gives the steady-state model:

$$P_l = P_S(V) \tag{5.16}$$

We can rewrite (5.15) as:

$$T_P\dot{P}_l + P_l = P_S(V) + T_P\frac{d}{dt}(P_T(V)) \tag{5.17}$$

where $P_T(V) = \frac{1}{T_P}\int_0^V k_P(\sigma)d\sigma + c_0$ and c_0 is a constant.

This can be converted to the following form by introducing the state variable:

$$\dot{x_P} = -\frac{1}{T_P}x_P + N(V) \tag{5.18}$$

$$x_P = T_P(P_l - P_T(V)) \tag{5.19}$$

$$N(V) = P_S(V) - P_T(V) \tag{5.20}$$

where $P_S = P_{l0}(V/V_0)^{\alpha_S}$ and $P_T = P_{l0}(V/V_0)^{\alpha_T}$ for the exponential load model. By setting $x_P = T_P P_{l0} z_P$, we can transform (5.18) to (5.5) and (5.19) to (5.1) respectively.

The above set of equations is solved analytically. The expression for x_P, which is the response to the voltage step from V_0 to V_1, can be obtained as follows:

$$x_P(t) = T_P N(V_1) + T_P[N(V_0) - N(V_1)]e^{\frac{-(t-t_0)}{T_P}} \tag{5.21}$$

Then from (5.19),

$$\begin{aligned} P_l(t) &= P_S(V_1) + [P_S(V_0) - P_T(V_0) - P_S(V_1) \\ &+ P_T(V_1)]e^{\frac{-(t-t_0)}{T_P}}, t > t_0 \end{aligned} \tag{5.22}$$

In this research, we further assume $P_S = P_{l0}$, then:

$$P_l(t) = P_{l0} + \left[P_{l0}(\frac{V_l}{V_0})^{\alpha_T} - P_{l0}\right] e^{\frac{-(t-t_0)}{T_P}} \tag{5.23}$$

By equating (5.23) and (5.13), the relation between $\alpha(t)$ and the changes of load dynamics could be established:

$$\alpha(t) = \log_{(\frac{V}{V_0})}\left(1 - e^{\frac{-(t-t_0)}{T_P}} + (\frac{V}{V_0})^{\alpha_T} e^{\frac{-(t-t_0)}{T_P}}\right) \tag{5.24}$$

Note that here V is adjusted during the load restoration simulation. Equation (5.24) can be used to predict $\alpha(t)$ at each time step. $\alpha(t)$ is selected as the continuation parameter while continuation method is applied for QSS analysis. Based on the above derivation, the new method is a very close approximation to the original differential equations. The introduction of the continuation parameter ($\alpha(t)$) establishes a link between generic load self-restoration and QSS simulation conveniently. Details will be presented in the following sections.

5.3 Parameterization of Load Exponents in QSS Simulation

In this section, the influence of parameterization on the continuation technique is described at first [54].

We demonstrate the concepts through the algebraic equation from the system DAEs, which is:

$$0 = g(y, \lambda) \tag{5.25}$$

The j-th continuation step starts from (an approximation of) a solution (y^j, λ_j) of (5.25) and attempts to calculate the solution (y^{j+1}, λ_{j+1}) for the next λ, namely, λ_{j+1},

$$(y^j, \lambda_j) \rightarrow (y^{j+1}, \lambda_{j+1}) \tag{5.26}$$

With *predictor-corrector* methods, the step $j \rightarrow j+1$ is split into two steps:

$$(y^j, \lambda_j) \longrightarrow (\overline{y}^{j+1}, \overline{\lambda}_{j+1}) \longrightarrow (y^{j+1}, \lambda_{j+1}) \tag{5.27}$$

In general, the predictor $(\overline{y}, \overline{\lambda})$ is not a solution of (5.25). The predictor merely provides an initial guess for corrector iterations that hone in on a solution of (5.25).

The distance between two consecutive solutions (y^j, λ_j) and (y^{j+1}, λ_{j+1}) is called the *step size*. In addition to (5.25), we need a relation that identifies the location of a solution on the branch. This identification is related to the kind of *parameterization* strategy chosen to trace the branch.

Different parameterizations correspond to different directions. The most obvious parameter is the control variable λ.

If another variable γ is chosen as the parameter, the solution of $g(y,\lambda)$ depends on γ. For a particular value of γ, the system $g(y,\lambda)=0$ consists of n equations for the $n+1$ unknown (y,λ). If the parameterization is established by one additional scalar equation.

$$p(y,\lambda,\gamma)=0 \tag{5.28}$$

we can formulate an extended system:

$$G(Y,\gamma) := \begin{pmatrix} g(y,\lambda) \\ p(y,\lambda,\gamma) \end{pmatrix} = 0 \tag{5.29}$$

which consists of $n+1$ scalar equations for the $n+1$ unknowns $Y=(y,\lambda)$. The general setting (5.29) includes all types of parameterization.

Solving (5.29) for specified values of γ yields information on the dependence $y(\gamma),\lambda(\gamma)$.

In (5.29) the parameterizing equation $p(y,\lambda,\gamma)=0$ is attached to the given system of (5.25). This allows us to apply Newton method to (5.29); in this way the desired parameterization is imposed on (5.25) automatically. Alternatively, some side conditions can be imposed on the iterations when applying Newton method.

Any of the components $y_i (i=1,....,n)$ can be admitted as a parameter, including $y_{n+1}=\lambda$. This comes to the parameterizing equation as follows:

$$p(y,\eta) := y_k - \eta \tag{5.30}$$

with an index $k, 1 \le k \le n+1$, and a suitable value of η. The index k and the parameter $\eta = y_k$ are locally determined at each continuation step (y^j,λ_j) in order to keep the continuation feasible. This kind of parameterization has been called *local parameterization*. With $Y=(y,\lambda)$, (5.29) is written as:

$$G(Y,\eta,k) = \begin{pmatrix} g(Y) \\ y_k - \eta \end{pmatrix} = 0 \tag{5.31}$$

It is easy to find a suitable index k and parameter value η. A continuation algorithm based on tangent predictors determines k such that:

$$|z_k| = max|z_1|,....,|z_n|,|z_{n+1}| \tag{5.32}$$

This choice picks the component of the tangent z that is maximal. After an index k is fixed, an appropriate value η must be determined. A value of η depends on the index k, on the location of the current solution on the branch (i.e., on j), and on the desired step size σ.

Local parameterization looks promising in the voltage stability problem and is often applied. In local parameterization, the local original set of equations is augmented by one equation that specifies the value of one of the state variables. In the original CPF, the selection of the continuation parameter is generally the load parameter. To find the solution to the augmented set of equations over a range of the load parameter, a step-by-step process might be used whereby the load parameter is increased by small amounts. The solution along a given path is found for each value of the load parameter. Local parameterization allows not only the added parameter but also the state variables to be used as the so-called continuation parameter. If this parameter is chosen correctly, the Jacobian of this augmented set of equations will remain nonsingular and the solution process will be well conditioned.

For a given contingency, the CQSS simulation will be applied to trace the system's PV curve, to find the equilibrium of the fast dynamics and to implement controls so as to achieve or enhance the system's stability. Generally, the load is chosen as the continuation parameter since it can be fully recovered to the pre-contingency value in Scenario One. Then the system continues to approach the SNB point if the load is increased. In Scenario Two, the total system load power can't be completely restored to the pre-contingency long-term level. During the load restoration process motivated by the OLTCs and the thermostatic load self-control mechanism, the system reaches the post-contingency SIB point and the voltage collapses. Therefore, it is not appropriate to increase the load any more and is reasonable to re-select the continuation parameter.

A typical load restoration procedure in a power system is from constant impedance load to constant power load. In order to simulate it, α or β is chosen as the continuation parameter. How it changes is determined by the whole set of DAEs defined for the CQSS simulation, the change of load components with respect to time (the prediction of $\alpha(t)$ as we proposed before) as well as the predictor-corrector scheme in continuation method. With parameterization of the load exponent, the system undergoes continuous evolution directed by the change of aggregate load components and types.

To simplify the problem, we assume that there is some dependence between $\alpha(t)$ and $\beta(t)$ and choose α as the continuation parameter.

Imagine the equilibrium trajectory of the system DAEs as a small particle moving along the branch. Also imagine a rope attached to the particle. Different parameterizations correspond to the different directions in which the rope can be pulled. If the pulling direction is normal to the branch, the tracing will encounter difficulties at this point. In this case, the load exponent is selected as the parameter as illustrated in Figure 5.3. The dashed lines correspond to the short-term load characteristics. Direction1 intersects the branch at the long-term SNB point with an angle smaller than 90°. Direction2 is normal

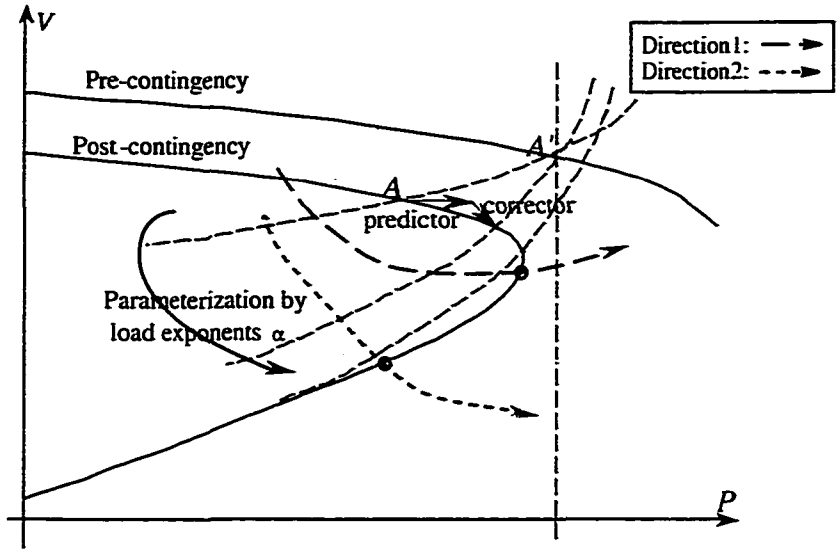

Figure 5.3 Load exponent as continuation parameter in PV diagram

to the branch at the SIB point [11]. How these directions intersect the PV curve is determined by the exact solutions of the DAEs under the parameterization of the load exponent. If it is Direction1, the SNB point can be solved without any computational difficulty by using this parameter directly. If it is close to Direction2, however, the continuation parameter should be changed according to the system's state. This will be discussed in the next section.

5.4 Implementation Issues

Referring to the continuation method applied in Chapter 4, where λ is chosen as the parameter to consider the load change, the state variables here are obtained under the parameterization of α to take into account load restoration. The major difference between them primarily comes from f_α and g_α in the system's Jacobian used for the predictor and corrector which are shown as follows:

$$-\begin{bmatrix} f_x & f_y & f_\alpha \\ g_x & g_y & g_\alpha \\ & e_k^T & \end{bmatrix}\begin{bmatrix} dx \\ dy \\ d\alpha \end{bmatrix} = \begin{bmatrix} 0 \\ 0 \\ \pm 1 \end{bmatrix} \tag{5.33}$$

and

$$-\begin{bmatrix} f_x & f_y & f_\alpha \\ g_x & g_y & g_\alpha \\ & e_k^T & \end{bmatrix}\begin{bmatrix} \Delta x \\ \Delta y \\ \Delta\alpha \end{bmatrix} = \begin{bmatrix} f \\ g \\ 0 \end{bmatrix} \tag{5.34}$$

We can find the sensitivities of load powers with respect to the load exponent which are given below:

$$\frac{dP_l}{d\alpha} = P_{l0}(\frac{V}{V_0})^\alpha \log(\frac{V}{V_0}) \tag{5.35}$$

$$\frac{dQ_l}{d\alpha} = Q_{l0}(\frac{V}{V_0})^\beta \log(\frac{V}{V_0})\frac{d\beta}{d\alpha} \tag{5.36}$$

where $d\beta/d\alpha$ is known before the calculation based on our assumption. These two equations also represent the major difference between f_λ (resp. g_λ) and f_α (resp. g_α).

From (5.35) and (5.36) together with (5.9) and (5.10), we know that the total load power variation depends on two major factors: one is the load bus voltage magnitude behind the OLTC and the other is the load exponent representing the load components and types. The driving force for voltage collapse stems from the OLTCs' action and the load self-restoration procedure.

There are two kinds of bifurcations which can be identified in load restoration. One is the singularity-induced bifurcation [11] and the other is the long-term saddle node bifurcation. Here we only address the former.

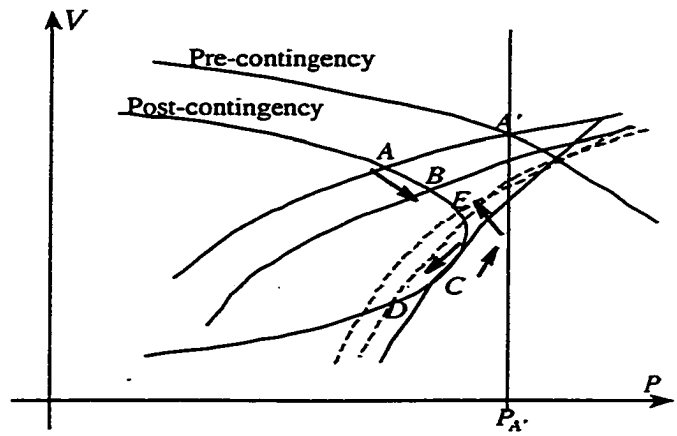

Figure 5.4 Tracing around the bifurcation point

It has been known that load exponents decrease from two (constant impedance load) to zero (constant power load) monotonically. Considering that (V/V_0) is generally less than one during load restoration since the system is under a severe condition. (5.35) and (5.36) become negative. It means that a decrease in α results in an increase in P_l. Now we define the decrease of α as the positive direction whereas the increase of α is the negative direction for the simulation. $d\alpha$ is positive before α reaches its minimum, and negative afterwards. Furthermore, since α is introduced to parameterize the system DAEs, null $d\alpha$ indicates some kind of singularity of the system's Jacobian. This can be shown as follows.

If null $d\alpha$ is detected in the predictor at some time step, (5.33) will reduce to:

$$\underbrace{\begin{bmatrix} f_x & f_y \\ g_x & g_y \end{bmatrix}}_{J_{xy}} \begin{bmatrix} dx \\ dy \end{bmatrix} = \begin{bmatrix} 0 \\ 0 \end{bmatrix} \tag{5.37}$$

$[dx \;\; dy]^T$ is not a null vector since one component of it should be ± 1. Then (5.37) implies the singularity of J_{xy}. From Appendix A and D, it infers the singularity of long-term dynamics. A classical scenario in the power system operation is that a long-term instability induces a short-term saddle node bifurcation. Thus it is reasonable to identify the instability point by equivalently detecting null $d\alpha$ during the tracing. It is an easier way to identify the singularity-induced bifurcation in the long-term time scale.

When the system approaches this point, there may be no intersection of the PV curve and the load characteristic curve if the step size is large. A similar method used for the previous CPF, that is, choosing another variable instead of load exponent as the continuation parameter, is also applied here. Then the tracing can resume.

In Scenario Two, an unsolvable case occurs at the operating point A' (Figure 5.4), which means the network characteristic no longer crosses the long-term load characteristic in the post-contingency configuration. The pre-contingency operating point A' jumps to A just after the disturbance. Then under the OLTC and load restoration effects, the operating point moves along the post-contingency PV curve. Point C is referred as the critical point for the singularity-induced bifurcation. When using the load exponent as the continuation parameter, α and β decrease continuously from A to C. However, in order to avoid the singularity of J_{xy}, another variable is selected as the parameter around C. So the solution may be located on the lower part of the curve, namely, D. At this point, negative $d\alpha$ is detected. After this, by properly adjusting the step size, we can identify C. It is illustrated in Figure 5.4. Meanwhile, the load exponent at a specific time is known through (5.24). How to relate load exponents to time can be solved by the similar approach that we have described for λ in Chapter 4.4.

5.5 CQSS Simulation for Scenario Two on a Small Test System

The simulation results for Scenario Two will be shown as follows. There are totally three cases presented. The first case doesn't apply continuation method since it only considers tap dynamics. In this case, we reproduce the results given in [5] to understand the OLTC's effects on voltage stability. The other two cases use continuation method, including generic load restoration in the simulation.

The contingency simulated for Scenario Two is the generation loss at Bus2 and the two-line tripping between Bus1 and Bus4 simultaneously. Before the contingency, the system is operated at a total real power load of $4600MW$. Real power generation at Bus2 is lost by $600MW$ during this severe disturbance. According to the short-term load characteristic, the post-contingency base case condition is established. However, the voltage behind the OLTC decreases to 0.92p.u., thus resulting in the system's total load of $3900MW$. After that, the driving force of system evolution is the OLTC actions and/or the load self-restoration procedure.

5.5.1 Case One: Only Considering Tap Dynamics

In this case, the load is represented with an exponential model ((5.13) and (5.14)) and the local generator is operated at 85% of maximum turbine power. The evolution of the system after the contingency is illustrated in Figure 5.5, which shows the voltage at Bus4, the transmission-side bus of the OLTC transformer feeding the load.

The short-term dynamics of the system are stable just after the contingency. Once the base case is obtained, the mechanism driving the system's response comes from the OLTC, which tries to restore the load-side voltage by lowering the tap ratio r. The operation of the OLTC starts just after the contingency, and continues at $5s$ intervals. This results in a further reduction of the transmission-side voltage V_4. At about $t = 340s$, the OLTC has reached its limit and the voltage decline stops, since no other dynamic mechanism is involved.

We observe the response of the load-side voltage V_3 and the OLTC ratio r in Figure 5.6. As seen in this figure, the response of the load voltage exhibits two radically different patterns. Before the generator limitation each tap movement produces the intended effect of raising the secondary voltage. After the limitation of the generator, the tap changes have initially almost no effect on V_3, and subsequently they even produce the reverse effect by lowering it. Several aspects of this unstable OLTC operation have been investigated in [55, 56, 57, 58].

In order to get a deeper understanding of the long-term instability mechanism, the system's PV curves is shown in Figure 5.7. In these curves, V_4 is plotted as a function of the transmitted power P

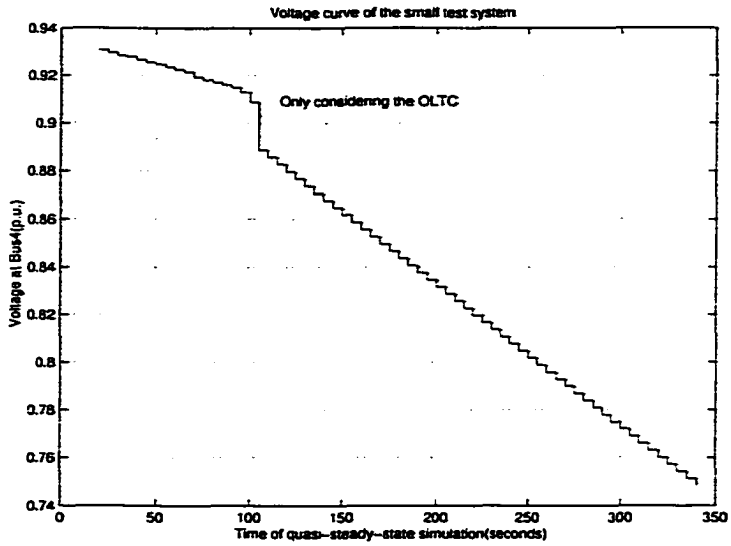

Figure 5.5 Voltage at Bus4 vs. time in Case One

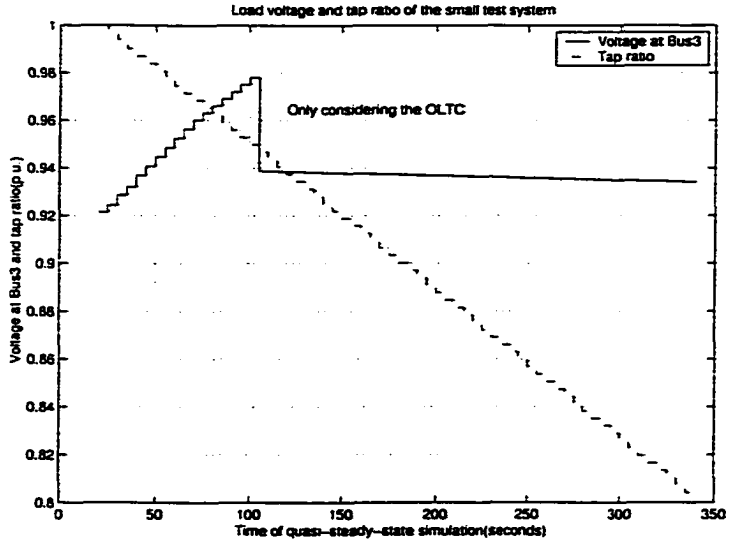

Figure 5.6 Voltage at Bus3 and tap ratio vs. time in Case One

through the OLTC. All the curves are drawn considering the short-term dynamics at equilibrium. Three network PV curves (pre-disturbance and post-disturbance (two curves)) are shown. These curves have been obtained by varying r continuously, solving the short-term equilibrium equations and recording the values of V_4 and P.

Before the disturbance the system operates at point A. The disturbance causes the network characteristic to shrink. Consequently, the system operates at the short-term equilibrium point A' corresponding to the current value of the tap. Subsequent OLTC actions bring the system to point B. At this point the generator reaches its limit and the system's PV curve has irregularity and the voltage jumps to B'. From there on, the OLTC keeps on decreasing the tap until it finally reaches its limit at D.

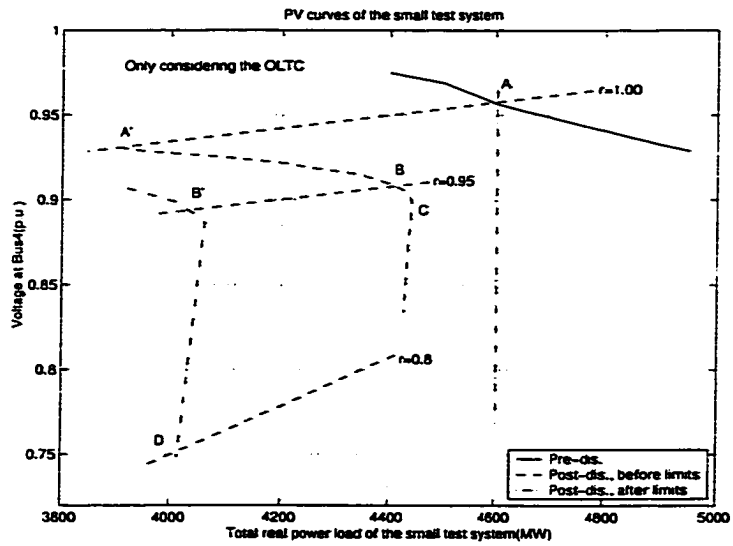

Figure 5.7 PV curves in Case One

Note that during the transition, C is identified as the saddle node bifurcation point. After this point, both voltage and load restoration by the OLTC fail.

The nature of instability is revealed by observing that the long-term load characteristic, which is the vertical line passing through the pre-disturbance operating point A, does not intersect the network PV curve after the contingency. This is a clear case of long-term instability, for which the long-term equilibrium equations corresponding to the final system configuration, have no solution.

Another two cases will be discussed in the following.

5.5.2 Case Two: Considering Both Tap and Thermostatic Load Dynamics

5.5.2.1 Equilibrium tracing: α as continuation parameter

In Case One, we saw a case of long-term instability, which ended up with the OLTC reaching its limit and the system settling down at unacceptably low voltages. The final outcome of the long-term instability due to the non-existence of the equilibrium after some disturbances, was the pseudo-stabilization at low voltage because of the OLTC limitation. This should not be mistaken for a stable steady state. Since only the OLTC is considered in Case One, it can't represent all the dynamics involved in the system. Other load recovery mechanisms may become active driving the voltage decline further towards a collapse. It is reasonable to consider the final operating condition as unstable, since any attempt to restore the load will drive the system to further degradation.

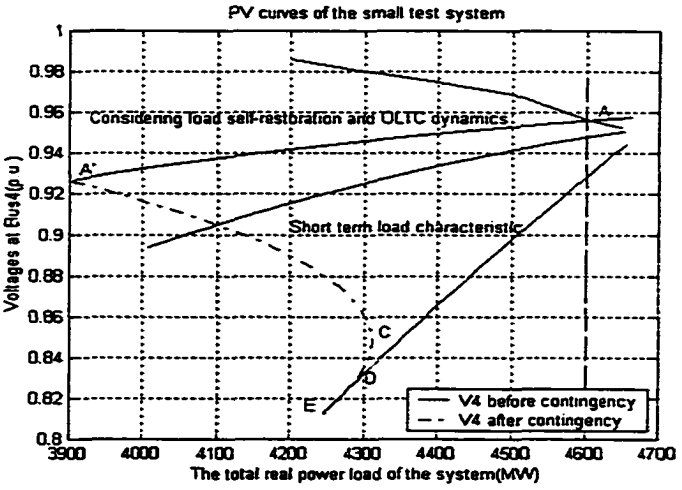

Figure 5.8 PV curves in Case Two

Now, we give one more example in which both tap dynamics and load self-restoration mechanisms are considered. It is essential to take into account load self-restoration effects which will continue to degrade the system's condition after the OLTC hits the limit. In this case, the system encounters a loss of short-term equilibrium after the long-term instability. The initial conditions of the system are modified by reducing the local generator active production to 75% rated turbine power. Therefore, the maximum power that can be transferred to the load slightly decreases, as can be observed by comparing the PV curves shown in Figure 5.8 with those in Figure 5.7. The operating point follows the path AA'

(with contingency), $A'C$ (OLTC and load self-restoration), C (the long-term saddle node bifurcation point of the network characteristic), D (OLTC limits) and E (the short-term saddle node bifurcation point induced by the long-term dynamics). Note that there is no generator limit reached in this case. No long-term equilibrium exists after the contingency. Furthermore, Figure 5.9 shows that the whole load restoration procedure is accelerated due to the OLTC actions which try to restore V_3. The increase of Bus3's voltage is due to the influence of the OLTC. Since the system is so close to the SIB point, however, even the OLTC can't fully recover Bus3's voltage to its reference value.

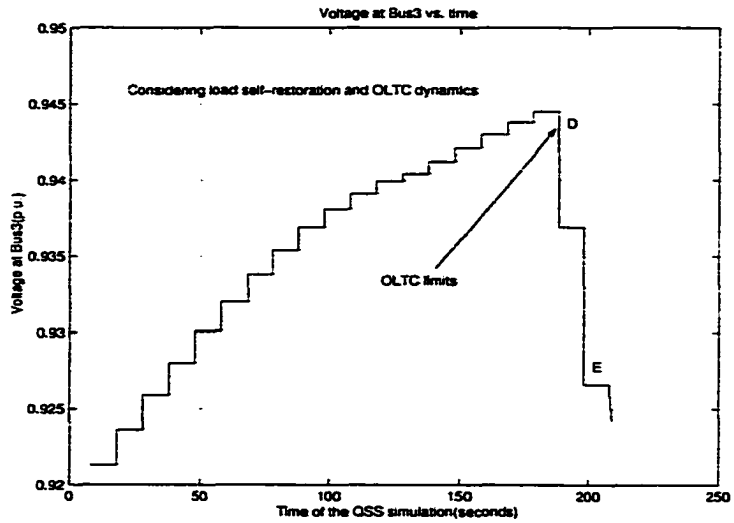

Figure 5.9 Voltage at Bus3 vs. time in Case Two

5.5.2.2 Identification of the Singularity-Induced Bifurcation

In Case Two, the post-contingency network characteristic does not intersect the short-term load characteristic after the OLTC is blocked while load self-restoration is still active. The system loses the short-term equilibrium, which constitutes singularity-induced bifurcation.

This bifurcation can be readily identified by null $d\alpha$. Table 5.1 shows how continuation parameter α changes in the last five steps. The sequence of events is shown in Figure 5.10 where the simulated response of the voltage at Bus4 is plotted as a function of time. As the OLTC keeps reducing the tap ratio, the generator eventually loses synchronism at about $t = 200s$. The loss of synchronism is obvious in Figure 5.11 showing the response of generator rotor angle at Bus2. The out-of-step relay will then

trip the generator. The final outcome of such a case is likely to be a blackout of the load area, caused by the tripping of the remaining line due to overload.

While in Case One, the limited range of the OLTC tap ratio somehow contained the long-term instability allowing some time for control actions, in this case, all the corrective measures have to be taken before the instability of short-term dynamics initiates a collapse.

Table 5.1 $d\alpha$ in the last five steps

Time(s)	160	170	180	190	200
$d\alpha$	-0.03317	-0.03228	-0.03130	-0.03016	0.02787

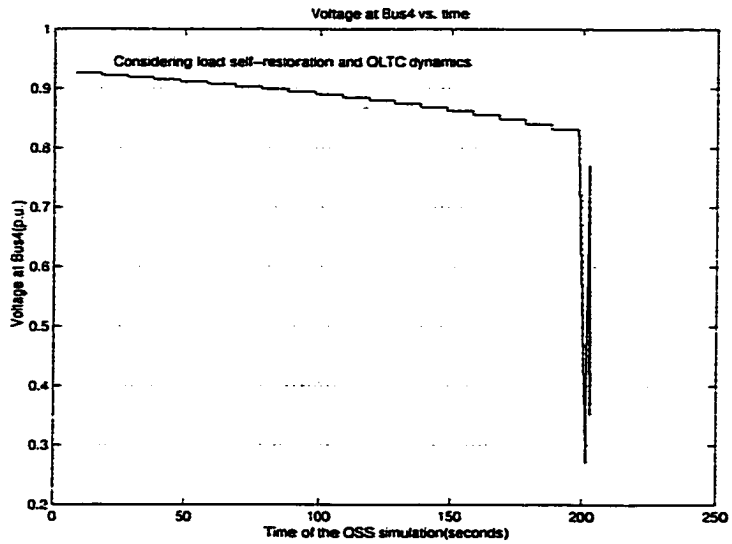

Figure 5.10 Voltage at Bus4 vs. time in Case Two

5.5.3 Case Three: Verification of the Continuation-Based Load Restoration

If the system has a relatively high critical voltage, the long-term SNB point is usually crossed before OLTCs reach their limits. In such a situation, load self-restoration effects are often "hidden" behind OLTC effects. They become significant if the OLTC is blocked.

In this section, the OLTC is treated as a regular transformer and only the load self-restoration dynamics are considered. In order to focus on the load dynamics, the generator limit is not taken into account here. The load restoration procedure begins with load exponents $\alpha(t_0) = \beta(t_0) = 2$ just after

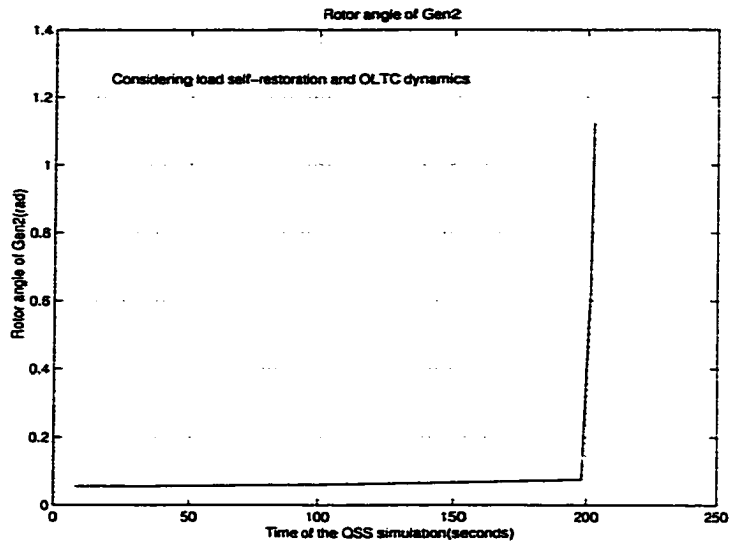

Figure 5.11 Generator angle at Bus2 vs. time in Case Two

the contingency and then the load slowly becomes constant power characteristic at steady-state, where $\alpha(t_{cc}) = \beta(t_{cc}) = 0$.

At $t = 0s$, the restoration begins with the total real power load power at $P = 3900MW$. The test system undergoes a voltage collapse after $t = 620s$ when the real power load is around $4450MW$, if no emergency control actions are performed. By using the load exponent as the continuation parameter to trace the system's trajectory after the contingency, Figure 5.12 shows Bus3's PV curve. Among the voltages at all buses, the voltage at Bus3 is the lowest one without the OLTC regulation. The maximum power (C) that the transmission system can deliver is $4460MW$ because of the specific load model. Figure 5.13 gives the comparison of the load response with respect to the time by using the proposed method and the differential representation of the load restoration procedure. As they apply the method for predicting $\alpha(t)$ or $\beta(t)$ at each time step, these two methods are very similar. The time constants T_P and T_Q equal $300s$ in the simulation. For the additive load model, the state variables z_P and z_Q in the differential representation are initialized to zero. However, when using integration methods (here the Euler method is used) to solve the system's short-term equilibrium after the contingency, the divergence of the power flow at such an equilibrium is considered as the bifurcation point. By introducing continuation method with α as the parameter, this SIB point (E) can be readily identified.

If no other dynamics are involved, thermostatic load restoration is a relatively slow procedure according to the applied time constants. It degrades the system's operating conditions more and more and finally results in the loss of the short-term equilibrium.

In this case, null $d\alpha$ is used to identify the singularity of J_{xy}, which implies the short-term saddle node bifurcation due to load restoration dynamics. At this point, the short-term load characteristic is tangent to the network PV curve. Table 5.2 gives the $d\alpha$ values in the last five steps.

In the above three cases, voltage collapse of the system could be observed through the curves obtained by the simulation. However, the exact identification of the long-term saddle node bifurcation can be achieved by trajectory sensitivity, which provides a characterization of any short-term equilibrium point making up the trajectory. The relevant results will be presented in Chapter 6.

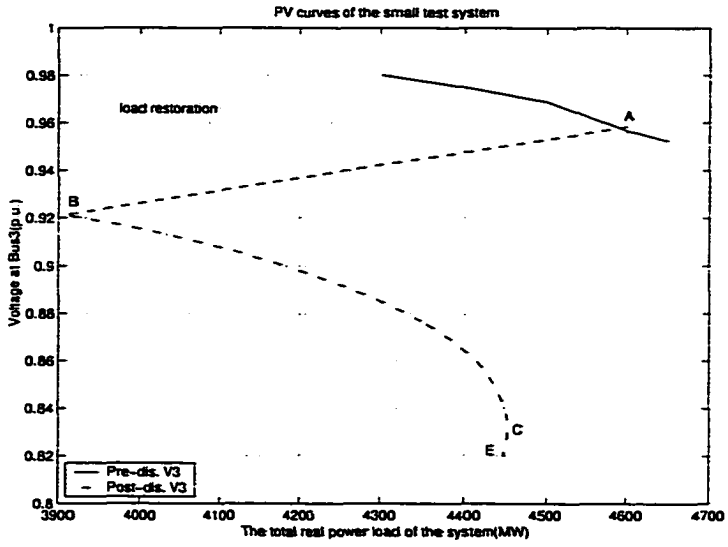

Figure 5.12 PV curves in Case Three

5.6 Concluding Remarks

In this chapter, the load restoration procedure in QSS simulation is solved by the parameterization strategy of continuation method. Compared to the numerical integration, it provides a simpler way to deal with this complicated process reasonably and efficiently.

The next chapter presents the application of trajectory sensitivity for voltage stability control.

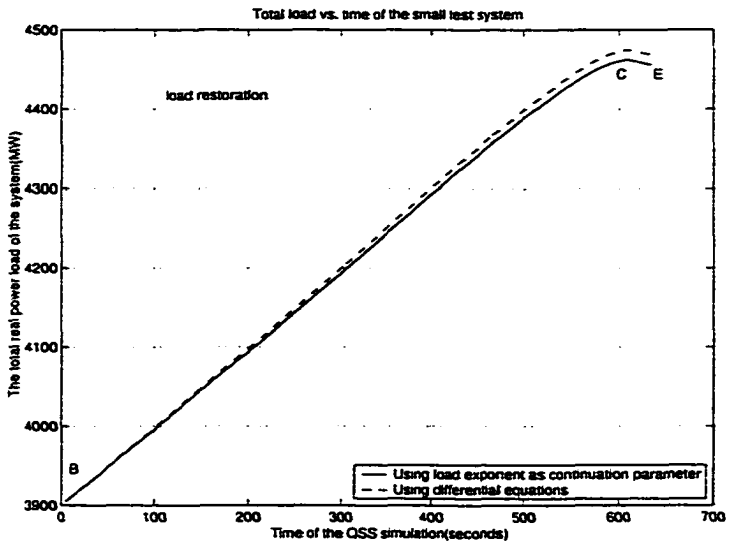

Figure 5.13 The system total real power load vs. time in Case Three

Table 5.2 $d\alpha$ in the last five steps

Time(s)	580	590	600	610	620
$d\alpha$	-0.026980	-0.026874	-0.026782	-0.026601	0.024925

6 TRAJECTORY SENSITIVITY FOR VOLTAGE STABILITY CONTROL

Sensitivity factors are well-known indices used in utilities throughout the world to detect voltage stability problems and to devise control measures. There is a rich literature on this topic which has been used in the past mainly for parameter identification in adaptive control systems. By using sensitivity techniques, useful information about the relationship between state, control and dependent variables can be established. Under normal operating states, sensitivity analysis provides information about how different parameters influence stability. Certain control measures can be designed in order to prevent the system from instability. Should the system be in an emergency state under disturbances, effective controls must be applied to pull the system back to a normal state. Sensitivity analysis is suitable for evaluating the effectiveness of the controls.

Trajectory sensitivity [36] can be defined as the sensitivity of the system's time-dependent state variables of the ODEs or DAEs to the parameters, especially the control variables. Pai et al. applied trajectory sensitivity for the power system dynamic security assessment [37, 59, 60, 61, 62]. According to their research, trajectory sensitivity functions of the post-fault system with respect to parameters, are computed by using the simultaneous implicit method. The authors presented trajectory sensitivity theory on the ODEs and DAEs briefly along with a motivating example. It has been shown that trajectory sensitivity is very robust and independent of unstable equilibrium point calculations and model complexity.

In voltage stability research, trajectory sensitivity is not commonly used. Van Cutsem proposed the idea of QSS analysis for the long-term dynamics of the system. The time information is incorporated by implementing the change of discrete-type long-term variables which are essentially represented by difference equations. QSS analysis provides a good basis for the application of trajectory sensitivity to voltage stability.

In previous chapters, continuation method has been extended to solve the system equations in QSS simulation. During the PV curve tracing, it is very helpful to know the sensitivity information of the

system's state variables to the control measures.

The whole system DAE model for voltage stability is different from the model for transient angle stability research. Although the derivation proposed in [37] can be applied here in a similar way, it does need some modifications. In this research, we solve the trajectory sensitivity at each equilibrium along the PV curve in the CQSS analysis. One application of trajectory sensitivity at such an equilibrium is to identify the long-term saddle node bifurcation. Also trajectory sensitivity can be used for implementing controls to enlarge the system's stability margin. Two different methods are applied to solve trajectory sensitivity.

6.1 Basic Theory of Trajectory Sensitivity [36]

Consider the n-dimensional nonlinear dynamic system of the following form:

$$E\dot{x} = f(t, x, \mu) \tag{6.1}$$

$$x(t_0) = x_0 \tag{6.2}$$

where x is an n-dimensional vector of state variables, μ is an m-dimensional vector of time independent system parameters and E is an (n, n) matrix of constant coefficients. Most frequently the matrix E assumes the form:

$$E = \begin{bmatrix} 0 & 0 \\ 0 & I^{(s)} \end{bmatrix} \tag{6.3}$$

where $I^{(s)}$ is the identity diagonal matrix of order s.

We define the (n, m) matrix $S(t)$ of sensitivity functions as:

$$S(t) = \frac{\partial x(t)}{\partial \mu} \tag{6.4}$$

This matrix satisfies a set of DAEs that can be derived by partial differentiation of (6.1) with respect to parameter vector μ:

$$ES'(t) - J(t)S(t) = \frac{\partial}{\partial \mu} f(t, x(t), \mu) \tag{6.5}$$

$$S(t = t_0) = \frac{\partial x_0(\mu)}{\partial \mu} \tag{6.6}$$

where the matrix $J(t)$ is defined as:

$$J(t) = \frac{\partial}{\partial x} f(t, x(t), \mu) \tag{6.7}$$

The most striking feature of these sensitivity equations is that they are linear, irrespective of the linearity or nonlinearity of the state equation (6.1). The problem studied here is the numerical computation of the matrix $S(t)$ from (6.5).

Equation (6.1) along with (6.5) forms a set of $(n+n*m)$ differential equations whose solution yields $S(t)$. After the sensitivity function is found, the state trajectories can be computed without integrating the differential equations again. This is because the solution $x(t,\mu)$ can be approximated as:

$$x(t,\mu) = x(t,\mu_0) + S(t) * (\mu - \mu_0) \tag{6.8}$$

This is true for the small variation in μ.

6.2 Mathematical Development of Trajectory Sensitivity Analysis [63]

First, consider the solution of state and sensitivity equations (6.1) and (6.5) as a single system. In this approach, the Jacobian matrix of the total system in (6.1) and (6.5) is needed. If we partition the sensitivity matrix $S(t)$ into column vector as:

$$S(t) = [s_1(t) \mid s_2(t) \mid ... \mid s_m(t)] \tag{6.9}$$

where

$$s_i(t) = \frac{\partial x(t)}{\partial \mu_i} \qquad i = 1, 2, ..., m \tag{6.10}$$

then the Jacobian matrix $J_a(t, x(t), S(t), \mu)$ of the total system in (6.1) and (6.5) [63] is:

$$J_a(t) = \begin{bmatrix} J(t) & 0 & 0 & \cdots & 0 \\ \dot{J_1}(t) & J(t) & 0 & \cdots & 0 \\ \dot{J_2}(t) & 0 & J(t) & \cdots & 0 \\ \vdots & & & & \\ \dot{J_m}(t) & 0 & 0 & \cdots & J(t) \end{bmatrix} \tag{6.11}$$

where

$$\dot{J_i}(t) = \frac{\partial J(t)}{\partial x(t)} s_i(t) + \frac{\partial J(t)}{\partial \mu_i} \qquad i = 1, 2, ..., m \tag{6.12}$$

The evaluation of J_a is a formidable calculation, however, it is a natural requirement of Newton iteration on the total equation system (6.1) and (6.5). A simpler and quicker approach is applied to solve (6.1) before (6.5) at each time step, as shown below, then the calculation of $\dot{J_i}(t)$ is not required.

Let $\tilde{x}^{(r)}(t)$ be the local interpolant of $x(t)$ obtained in r Newton iterations of a j-th order integrator within a given time step. Then the next iteration will give the interpolant $\tilde{x}^{(r)}(t) + \Delta\tilde{x}^{(r)}(t)$ that satisfies the following linearized form of (6.1):

$$E(\tilde{x}'^{(r)}(t) + \Delta\tilde{x}'^{(r)}(t)) = f(t, \tilde{x}^{(r)}(t), \mu) + J(t, \tilde{x}^{(r)}(t), \mu)\Delta\tilde{x}^{(r)}(t) + O(h^j) \tag{6.13}$$

hence the correction $\Delta\tilde{x}^{(r)}$ satisfies:

$$E\Delta\tilde{x}^{'(r)}(t) - J^{(r)}(t)\Delta\tilde{x}^{(r)}(t) = f(t, \tilde{x}^{(r)}(t), \mu) - E\tilde{x}^{'(r)}(t) + O(h^j) \tag{6.14}$$

when the standard Newton method with $J^{(r)}(t)$ updated for each iteration is used. If $\Delta\tilde{x}^{(r)}(t)$ converges to zero with increasing r, then $J^{(r)}(t)$ converges to $J(t)$, and (6.14) becomes formally similar to (6.5). Therefore, we can defer consideration of (6.5) until $\tilde{x}^{(r)}(t)$ has converged to $x(t)$ at the current value of t. Then we can update the sensitivity solution $S(t)$ directly by the use of (6.5) that has the same coefficients as (6.14) but a different, now computable, right-hand side function. More specifically, the correction $\Delta\tilde{s}_i(t)$ is computed in a single iteration by solving:

$$E\Delta\tilde{s}_i^{'}(t) - J(t)\Delta\tilde{s}_i(t) = -E\tilde{s}_i^{'(p)}(t) + J(t)\tilde{s}_i^{(p)}(t) + \frac{\partial}{\partial\mu}f(t, \tilde{x}(t), \mu) + O(h^j) \qquad i = 1, 2, \ldots, m \tag{6.15}$$

in which $\tilde{s}_i^{(p)}(t)$ is the predicted value of $\tilde{s}_i(t)$ via a j-th order predictor formula.

The vector $\tilde{s}_i(t)$ can be calculated at the current t as follows:

$$\tilde{s}_i(t) = \tilde{s}_i^{(p)}(t) + \Delta\tilde{s}_i(t) \qquad i = 1, 2, \ldots, m \tag{6.16}$$

On completion of the update, the local truncation error is tested and, if necessary, the step size h and the approximate order j are adjusted to achieve the specified accuracy for $x(t)$ and $S(t)$.

6.3 Practical Issues of Stability Analysis and Equilibrium

Before explaining the application of trajectory sensitivity for voltage stability, some practical issues associated with the eigen-analysis in this research are discussed first.

The prerequisite to a stability test is the existence of an equilibrium. Generally, the eigenvalues of a linearized system at an equilibrium are calculated to obtain more information about the system's stability. In this research, we divide time scales to the long term and the short term. Strictly, the short-term (resp. long-term) stability should be analyzed at the short-term (resp. long-term) equilibrium. QSS approximation can be considered as a time domain simulation method to get a succession of short-term equilibrium points varied by the long-term dynamics. Moreover, these short-term equilibria are stable before the system reaches the SIB point, a fact which has been reasonably verified by the previous research [28, 64, 65] through testing on the practical power systems. Basically, we want to confirm if the system is stable or unstable by examining eigenvalues of a linearization about this approximation trajectory. Alternately, various linear sensitivity indicators might be used as computationally efficient approximations to stability information obtained from an eigen-analysis. In this work,

we apply trajectory sensitivity evaluated at some points of the simulated system trajectory to test the long-term stability. In this context, the motion of the system along the trajectory is being driven by time variations of one or more system parameters or exogenous inputs, i.e., $\lambda(t)$. The linearization that describes local behavior of deviations of the state from this trajectory, is itself a time-varying linear system. We no doubt realize that even a full eigen-analysis that displays all eigenvalues with strictly negative real parts, is not adequate to rigorously guarantee stability of such a time-varying system.

It might be expected that several requirements need to be met for this technique to be applicable, as we translate these general theoretical observations to a practical context.

First, the dynamics of the "fast" states must indeed have their time scales well separated from the dynamics that are assumed slow, and these fast dynamics must be stable and converge rapidly to the quasi-equilibrium predicted by setting their right hand sides to zero. A heuristic test of these properties might be to check that the eigenvalues of the sub-block of the linearized dynamics associated with these states, has all eigenvalues "far" into the left half plane with all complex pairs showing good damping. In effect, this is the basic assumption for QSS analysis.

Another assumption to guarantee stability of a time-varying system from a sequence of "quasi-equilibrium" linearizations has been the subject of many works in the literature [66]. In brief, we need one of two conditions on the time-varying inputs driving the evolution of the system: their time rate of change must be sufficiently slow (where slow is measured relative to time constants of all the system's dynamics), or they must be sufficiently small in magnitude (where the size of the allowable perturbation relates to the region of attraction about the nominal trajectory).

In order to achieve the above conditions, we calculate and interpret sensitivities in the following ways:

- Identification of a long-term equilibrium can be achieved by observing if the load has been fully recovered by the OLTCs or the self-restoration mechanism. Based on such an equilibrium, eigen-analysis can be used.

- Load margin calculation using λ as the parameter (for Scenario One): An increase in demand is imposed on the system and trajectory sensitivities are checked at regular time intervals. From the viewpoint of the system's operation, the rate of change in load increase can be considered "smooth" with respect to the system's dynamics. This means that the system's evolution can be considered close to a succession of long-term equilibrium points. Negative eigenvalues, hence, can be interpreted as one stable long-term equilibrium. However, these equilibria are just the

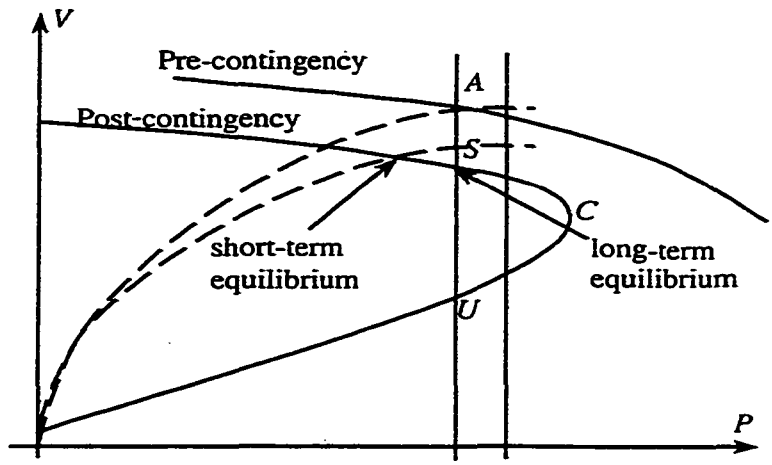

Figure 6.1 Long-term equilibrium by using load parameter λ

approximations since the OLTC dynamics may be still involved to move the simulated trajectory a little away from the exact long-term equilibrium trajectory.

Note that in this research the voltage collapse proximity index is the load power margin. The sensitivities are used only to determine the local stability while stressing the system at large. It is shown in Figure 6.1.

- Large-disturbance calculation using α as the parameter (for Scenario Two): we calculate the sensitivities along the system's trajectory with the sole aim to identify the SNB point where the trajectory sensitivity is larger than a certain threshold value. This corresponds to the point where the trajectory hits the long-term stability boundary. In this case, we do not interpret negative eigenvalues as the stability of a long-term equilibrium, for the simple reason that this long-term equilibrium does not exist any more.

  However, for the particular long-term dynamics of concern here, each point of the trajectory can be considered fictitiously as the long-term equilibrium point corresponding to the modified tap changer voltage set-points (this would shift the long-term load characteristic line to the left up to crossing the PV curve at some point). The stability can be checked by slightly disturbing the tap ratio. It is shown in Figure 6.2.

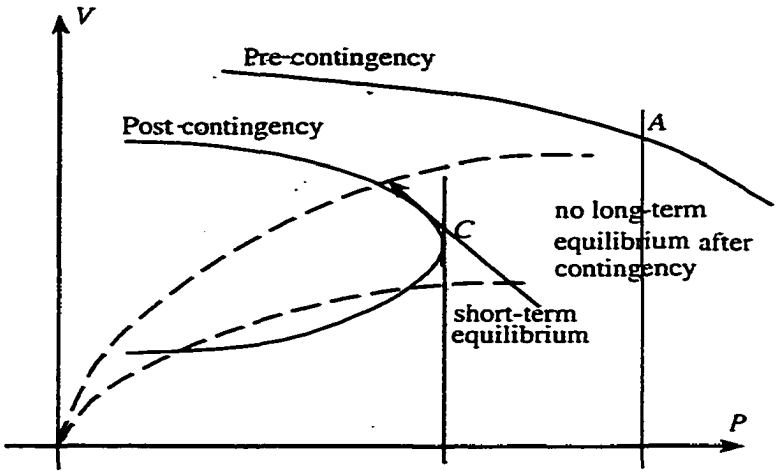

Figure 6.2 Long-term equilibrium by using load exponent α

6.4 Trajectory Sensitivity for Voltage Stability Study

In this research, the CQSS analysis is used to solve the whole system DAEs and trajectory sensitivity is calculated at each short-term equilibrium during the simulation. Note that only the sensitivity at such equilibrium is computed so that trajectory sensitivity is not truly continuous "trajectory" along with the time. Furthermore, continuation method is applied to solve the system equations. The tracing procedure counts on the continuation parameter step by step. According to continuation method, the whole system DAEs are augmented by one parameterized equation which is:

$$p(x, y, z, \lambda, \mu) = 0 \tag{6.17}$$

Then the following DAE system including original and sensitivity equations can be obtained:

$$0 = f(x, y, z, \lambda, \mu) \qquad x(t_0) = x_0 \tag{6.18}$$

$$0 = g(x, y, z, \lambda, \mu) \qquad y(t_0) = y_0 \tag{6.19}$$

$$\dot{z} = h(x, y, z, \lambda, \mu) \qquad z(t_0) = z_0 \tag{6.20}$$

$$0 = p(x, y, z, \lambda, \mu) \qquad \lambda(t_0) = \lambda_0 \tag{6.21}$$

$$0 = \frac{\partial f}{\partial x}w_1 + \frac{\partial f}{\partial y}w_2 + \frac{\partial f}{\partial z}w_3 + \frac{\partial f}{\partial \lambda}w_4 + \frac{\partial f}{\partial \mu} \qquad w_1(t_0) = 0 \tag{6.22}$$

$$0 = \frac{\partial g}{\partial x}w_1 + \frac{\partial g}{\partial y}w_2 + \frac{\partial g}{\partial z}w_3 + \frac{\partial g}{\partial \lambda}w_4 + \frac{\partial g}{\partial \mu} \qquad w_2(t_0) = 0 \tag{6.23}$$

$$\dot{w}_3 = \frac{\partial h}{\partial x}w_1 + \frac{\partial h}{\partial y}w_2 + \frac{\partial h}{\partial z}w_3 + \frac{\partial h}{\partial \lambda}w_4 + \frac{\partial h}{\partial \mu} \qquad w_3(t_0) = 0 \tag{6.24}$$

$$0 = \frac{\partial p}{\partial x}w_1 + \frac{\partial p}{\partial y}w_2 + \frac{\partial p}{\partial z}w_3 + \frac{\partial p}{\partial \lambda}w_4 + \frac{\partial p}{\partial \mu} \qquad w_4(t) = 0 \tag{6.25}$$

where μ is a vector of control variables, or the system paramcter. And w_1, w_2, w_3, w_4 are defined as follows:

$$w_1 = \frac{\partial x}{\partial \mu} \tag{6.26}$$

$$w_2 = \frac{\partial y}{\partial \mu} \tag{6.27}$$

$$w_3 = \frac{\partial z}{\partial \mu} \tag{6.28}$$

$$w_4 = \frac{\partial \lambda}{\partial \mu} \tag{6.29}$$

From the continuation method and the characteristics of trajectory sensitivity, $\frac{\partial p}{\partial x} = \frac{\partial p}{\partial y} = \frac{\partial p}{\partial z} = \frac{\partial p}{\partial \mu} = 0$, and $\frac{\partial p}{\partial \lambda} = 1$. Evaluation of trajectory sensitivity at each equilibrium goes along with the change of λ, which is chosen as the continuation parameter in the simulation. λ does not depend on the control measures and its sensitivity with respect to the controls must be equal to zero at each equilibrium except at the SNB point. Therefore, it should be pre-defined that $w_4 = 0$.

We can solve (6.18-6.25) by using the methodology introduced in Chapter 6.2. Applying small-disturbance analysis to (6.18-6.20), the following equation will be obtained:

$$\begin{bmatrix} 0 \\ 0 \\ \Delta \dot{z} \end{bmatrix} = \begin{bmatrix} f_x(t) & f_y(t) & f_z(t) \\ g_x(t) & g_y(t) & g_z(t) \\ h_x(t) & h_y(t) & h_z(t) \end{bmatrix} \begin{bmatrix} \Delta x \\ \Delta y \\ \Delta z \end{bmatrix} = J(t) \begin{bmatrix} \Delta x \\ \Delta y \\ \Delta z \end{bmatrix} \tag{6.30}$$

where $J(t)$ is the Jacobian matrix that is evaluated at each short-term equilibrium.

Based on the notations introduced before, we can define:

$$s_i(t) = \begin{bmatrix} w_{1i}(t) \\ w_{2i}(t) \\ w_{3i}(t) \end{bmatrix} \qquad i = 1, 2, ..., m \tag{6.31}$$

Then the functions associated with sensitivity in (6.22-6.24) can be written as:

$$E\dot{s}_i(t) - J(t)s_i(t) = \frac{\partial}{\partial \mu_i} \begin{bmatrix} f \\ g \\ h \end{bmatrix} \tag{6.32}$$

We can apply small-disturbance analysis to (6.32) to get:

$$E\Delta\dot{s_i}(t) = J(t)\begin{bmatrix} dx \\ dy \\ dz \end{bmatrix} + J(t)\Delta s_i(t) \tag{6.33}$$

where

$$J_i(t) = \frac{\partial J(t)}{\partial [x \;\; y \;\; z]^T}\begin{bmatrix} \frac{\partial x}{\partial \mu_i} \\ \frac{\partial y}{\partial \mu_i} \\ \frac{\partial z}{\partial \mu_i} \end{bmatrix} + \begin{bmatrix} f_{x\mu_i} & f_{y\mu_i} & f_{z\mu_i} \\ g_{x\mu_i} & g_{y\mu_i} & g_{z\mu_i} \\ h_{x\mu_i} & h_{y\mu_i} & h_{z\mu_i} \end{bmatrix} \tag{6.34}$$

It is not necessary to calculate $J_i(t)$ at each time step. The central idea here is that (6.18-6.21) will be solved first, then (6.22-6.25) will be considered for the reason which has been mentioned before. We defer the calculation of (6.22-6.25) until $[x \;\; y \;\; z]^T$ is solved at the current t. After the Jacobian matrix has been updated based on the converged $[x \;\; y \;\; z]^T$ at the present time step, the corrections $\Delta\tilde{s_i}(t)$ can be calculated by solving the following equation only once:

$$E\Delta\tilde{s_i}'(t) - J(t)\Delta\tilde{s_i}(t) = -E\tilde{s_i}'^{(p)}(t) + J(t)\tilde{s_i}^{(p)}(t) + \frac{\partial}{\partial \mu_i}\begin{bmatrix} f \\ g \\ h \end{bmatrix} \tag{6.35}$$

where $\tilde{s_i}^{(p)}$ is the predicted value of $\tilde{s_i}(t)$.

s_i can be solved by applying either a partitioned scheme to (6.35) or a simultaneous scheme directly to (6.22-6.24). In a partitioned scheme, the differential equations and algebraic equations are solved separately and alternatively, perhaps by using iterations. In a simultaneous scheme, all the equations are solved at the same time. In order to gain a better understanding of trajectory sensitivity in an analytical way, first the simultaneous single-step implicit method is used, then:

$$0 = f_x w_{1i}^{k+1} + f_y w_{2i}^{k+1} + f_z w_{3i}^{k+1} + f_{\mu_i} \tag{6.36}$$

$$0 = g_x w_{1i}^{k+1} + g_y w_{2i}^{k+1} + g_z w_{3i}^{k+1} + g_{\mu_i} \tag{6.37}$$

$$w_{3i}^{k+1} = w_{3i}^{k} + h\beta_0(h_x w_{1i}^{k+1} + h_y w_{2i}^{k+1} + h_z w_{3i}^{k+1} + h_{\mu_i}) \tag{6.38}$$

where k is the time step.

Considering that w_{3i}^{k} is used in the predictor-corrector method, we get:

$$(J(t) - cE)s_i = E[s_i'^{(p)}(t) - cs_i^{(p)}(t)] - \frac{\partial}{\partial \mu_i}\begin{bmatrix} f \\ g \\ h \end{bmatrix} = R_i(t) \tag{6.39}$$

where c is a constant that depends on step-size history. Here, $c = 1/h\beta_0$, where β_0 is the coefficient representing that the applied numerical integration is an implicit method.

More specifically, (6.39) can be expressed as follows:

$$s_i = \begin{bmatrix} f_x & f_y & f_z \\ g_x & g_y & g_z \\ h_x & h_y & h_z - cI \end{bmatrix}^{-1} (R_i) = J_{sen}^{-1} R_i \tag{6.40}$$

In this research, since $h_z = 0$, then,

$$J_{sen} = \begin{bmatrix} & & 0 \\ & J_{xy} & \\ & & g_z \\ 0 & h_y & -cI \end{bmatrix} \tag{6.41}$$

where J_{xy} evaluated at the long-term SNB point is generally nonsingular.

According to Schur's formula,

$$det(J) = det(J_{xy}) det\left(0 - \begin{bmatrix} 0 & h_y \end{bmatrix} J_{xy}^{-1} \begin{bmatrix} 0 \\ g_z \end{bmatrix}\right) = det(J_{xy}) det(J') \tag{6.42}$$

We know that at the long-term SNB point, $det(J) = 0$ and $det(J_{xy}) \neq 0$, then $det(J') = 0$ which means J' has a zero eigenvalue. Now,

$$det(J_{sen}) = det(J_{xy}) det(-cI + J') \tag{6.43}$$

Assuming that J' has distinct eigenvalues, we transform it to the Jordan Form and observe that each eigenvalue of J', including the zero eigenvalue, is reduced by c. The reason is that $-cI$ keeps unchanged in the transformation. Therefore, by appropriately selecting c, J_{sen} can be a nonsingular matrix since the zero eigenvalue at the long-term SNB point becomes nonzero. The real part of other eigenvalues at this point are negative since we assume that angle stability has been achieved and Hopf bifurcation of voltage stability doesn't happen. Generally, c is a positive value so that the real part of any other eigenvalue becomes more negative. The zero eigenvalue still dominates the sensitivity calculation.

Several comments can be made on the trajectory sensitivity in the long-term time scale simulation based on the above derivation.

- Trajectory sensitivity is derived from a set of equations related to the short-term equilibrium modified by the long-term dynamics in the CQSS simulation. It is evaluated at such an equilibrium. In Scenario One, the short-term equilibrium can be considered also as an approximation of

a long-term equilibrium. It gives the system's stability information. In Scenario Two, it is used only to identify the long-term SNB point but gives no indication whether the system is voltage stable or not.

- At the long-term SNB point, $J(t)$ is singular. Sensitivities which are directly calculated from $J(t)^{-1}$ becomes infinity. Though it may be taken as an indicator of the instability, we lose the true sensitivity information or we can't be sure if the infinity comes from the pure numerical problem. J_{sen} however can be used to calculate trajectory sensitivity readily, even at the SNB point.

- When the system approaches the SNB point, $J(t)$ becomes more and more ill-conditioned. It means that at least one eigenvalue is getting closer to the origin through the real axis of the complex plane. By calculating J_{sen}, we "push" these eigenvalues back to the left part of the plane and a little away from the origin. However, the trend of becoming ill-conditioned still exists. Sensitivities calculated from J_{sen} become larger and larger along the equilibrium trajectory, though they don't become infinity at the SNB point. Therefore, they can be utilized to measure the stress on the system's stability. A threshold value for trajectory sensitivity could be set as the criterion of the long-term saddle node bifurcation.

- The approach to solve trajectory sensitivity introduced next is to apply a partitioned scheme which is similar to QSS analysis. From the calculation, we know that w_1 and w_2 can be considered as the exact sensitivity at a long-term equilibrium, while w_3 is the approximated sensitivity at such an equilibrium since it is modified a little by the difference equation.

6.5 Solving Trajectory Sensitivity in the CQSS Analysis

Another way to solve trajectory sensitivity is the partitioned scheme. In QSS analysis, it is known that: $h_x = 0, h_z = 0$ and $f_z = 0$. Now we rewrite (6.35) as:

$$-\begin{bmatrix} f_x & f_y & 0 \\ g_x & g_y & g_z \end{bmatrix}\begin{bmatrix} \Delta\tilde{w}_{1i}(t) \\ \Delta\tilde{w}_{2i}(t) \\ \Delta\tilde{w}_{3i}(t) \end{bmatrix} = \begin{bmatrix} f_x & f_y & 0 \\ g_x & g_y & g_z \end{bmatrix}\begin{bmatrix} \tilde{w}_{1i}^{(p)}(t) \\ \tilde{w}_{2i}^{(p)}(t) \\ \tilde{w}_{3i}^{(p)}(t) \end{bmatrix} + \begin{bmatrix} f_{\mu_i} \\ g_{\mu_i} \end{bmatrix} \tag{6.44}$$

$$\Delta\tilde{w}_{3i}'(t) - h_y\Delta\tilde{w}_{2i}(t) = -\tilde{w}_{3i}'^{(p)}(t) + h_y\tilde{w}_{2i}^{(p)}(t) \qquad \text{since } h_{\mu_i} = 0 \tag{6.45}$$

In order to use the Jacobian matrix which has been formed in the CQSS analysis, two procedures that separate the sensitivity calculation associated with fast dynamics and slow dynamics are implemented.

Since $[x \;\; y \;\; z]^T$ is the converged solution at the current time step when we calculate trajectory sensitivity, we don't need to update the Jacobian matrix again. First, for (6.44), $[\Delta\tilde{w}_{1i} \;\; \Delta\tilde{w}_{2i}]^T$ is updated at the same time we temporarily assume that $\Delta\tilde{w}_{3i} = 0$. Then (6.44) becomes:

$$-\begin{bmatrix} f_x & f_y & f_\lambda \\ g_x & g_y & g_\lambda \\ & e_k^T & \end{bmatrix}\begin{bmatrix} \Delta\tilde{w}_{1i}(t) \\ \Delta\tilde{w}_{2i}(t) \\ \Delta\tilde{w}_{4i}(t) \end{bmatrix} = \begin{bmatrix} f_x & f_y & f_\lambda \\ g_x & g_y & g_\lambda \\ & e_k^T & \end{bmatrix}\begin{bmatrix} \tilde{w}_{1i}^{(p)}(t) \\ \tilde{w}_{2i}^{(p)}(t) \\ \tilde{w}_{4i}(t) \end{bmatrix} + \begin{bmatrix} f_{\mu_s} \\ g_{\mu_s} + g_z\tilde{w}_{3i}^{(p)} \\ 0 \end{bmatrix} \tag{6.46}$$

where $\tilde{w}_{3i}^{(p)}$ is the predicted value of w_{3i} at the current time step. Secondly, $\Delta\tilde{w}_{3i}'$ is calculated by using (6.45) and $\tilde{w}_{3i}'$ is updated. Then, $\tilde{w}_{3i}$ can be obtained by the Backward Euler method. Finally, (6.46) is applied again to get more accurate values for $[\tilde{w}_{1i} \;\; \tilde{w}_{2i}]^T$ by using $\tilde{w}_{3i}$ instead of the predicted value.

Note that the definition of w_{4i} which has been discussed before is related to the continuation parameter. In addition, in order to keep $w_{4i} = 0$ during the whole tracing procedure (it has been set to zero at the very beginning of the tracing), k should always be the number of the last row or column of the Jacobian matrix. Actually, in the last step, if we left-multiply the inverse of the Jacobian matrix to both sides of (6.46), then:

$$\begin{bmatrix} \tilde{w}_{1i}^{(p)}(t) \\ \tilde{w}_{2i}^{(p)}(t) \\ \tilde{w}_{4i}(t) \end{bmatrix} + \begin{bmatrix} \Delta\tilde{w}_{1i}(t) \\ \Delta\tilde{w}_{2i}(t) \\ \Delta\tilde{w}_{4i}(t) \end{bmatrix} = \begin{bmatrix} \tilde{w}_{1i}(t) \\ \tilde{w}_{2i}(t) \\ \tilde{w}_{4i}(t) \end{bmatrix} = -\begin{bmatrix} f_x & f_y & f_\lambda \\ g_x & g_y & g_\lambda \\ & e_k^T & \end{bmatrix}^{-1}\begin{bmatrix} f_{\mu_s} \\ g_{\mu_s} + g_z\tilde{w}_{3i}(t) \\ 0 \end{bmatrix} \tag{6.47}$$

From (6.47), we know that $[\tilde{w}_{1i} \;\; \tilde{w}_{2i}]^T$ at the current step can be obtained directly after the calculation of $\tilde{w}_{3i}$.

The solvability of this equation depends on the singularity of the augmented Jacobian that is used in the equilibrium-tracing procedure. Generally, the selection of k is appropriate and the augmented Jacobian matrix can be applied to calculate trajectory sensitivity directly. When the system approaches the long-term SNB point, the augmented Jacobian matrix becomes ill-conditioned if we still choose the last row or column of the matrix as the continuation parameter to keep $w_4 = 0$. In order to overcome this problem, a variable other than λ is selected as the parameter to find the solution of the DAEs. Fortunately, at the long-term SNB point, the sensitivity of the load to the controls need not be fixed as zero any more. It has been defined as margin sensitivity ([15] and [67]). Based on margin sensitivity (Appendix C), we can identify and implement the most effective controls.

Trajectory sensitivity is derived from the short-term equilibrium accompanied by the slow change of long-term dynamics. Whereas margin sensitivity is based on the condition of a long-term equilib-

rium (the SNB point) and also evaluated at such an equilibrium. In brief, trajectory sensitivity is quasi-steady-state while the original margin sensitivity comes from the absolute steady-state analysis. However, for the same reasons that have been discussed for the eigen-analysis of an equilibrium, we know that trajectory sensitivity at the long-term SNB point in Scenario One is almost the same as margin sensitivity. Hence it could be applied in the control problem to maintain a certain stability margin. In this research, margin sensitivity is a subset of trajectory sensitivity at the long-term SNB point by introducing λ through continuation method.

Since J_{sen} is not the exact Jacobian associated with the long-term dynamics, it is nonsingular at the long-term SNB point. Trajectory sensitivity at the SNB point can be calculated readily. At the SIB point, sensitivity calculation uses the augmented Jacobian after the converged solution has been obtained. Though J_{xy} is singular, the augmented Jacobian is not. The sensitivity information at the SIB point can still be calculated by using the augmented Jacobian matrix since $w_4 = 0$ is no longer a constraint.

Now, with all the tools and techniques available, we can mitigate long-term voltage instability as proposed in Chapter 7.

6.6 Trajectory Sensitivity Application for a Small Test System

6.6.1 Trajectory Sensitivity Application in Scenario One

During the simulation, trajectory sensitivity at each equilibrium is calculated to obtain the sensitivity information of the system's state variable with respect to different control parameters. This is useful when we implement controls to increase the system's stability margin. For this small system, there are totally 25 state variables and 6 control parameters. Trajectory sensitivity at each time step could constitute a $25 * 6$ matrix. With respect to each control, the largest state variable sensitivity is called peak value. Normalization of the sensitivity may be applied here. Table 6.1 gives the peak value of the sensitivity with respect to governor generation setting, AVR reference voltage, shunt capacitance and load shedding at time interval $t = 100s$.

6.6.1.1 Identification of the long-term saddle node bifurcation

Figures 6.3 and 6.4 show sensitivities evaluated at all trajectory points. As expected, they tend to large positive values and then switch to large negative values as the long-term SNB point is crossed. Figure 6.3 refers to the peak value of trajectory sensitivity with respect to AVR reference voltage and

governor generation setting while Figure 6.4 refers to the peak value of the sensitivity with respect to load shedding and shunt capacitance. At the SNB point, all sensitivities change sign together. This result is similar to the one shown in [38]. However, trajectory sensitivity provides all the state variable sensitivity information, and could be applied in the control implementation shown in the next chapter.

Table 6.1 Peak values of trajectory sensitivity with respect to different controls

Time(s)	P_{gs01}	P_{gs02}	V_{ref1}	V_{ref2}	B_{sh3}	P_{l03}
150	0.10652	0.09223	0.2583	0.2430	0.12292	0.4750
250	0.10675	0.09237	0.2585	0.2431	0.12304	0.4751
350	0.10704	0.09262	0.2588	0.2432	0.12311	0.4752
450	1.80869	1.67420	4.0742	3.2833	4.58740	8.2652
470	132.9743	120.4982	235.8964	220.4571	128.4892	300.3421

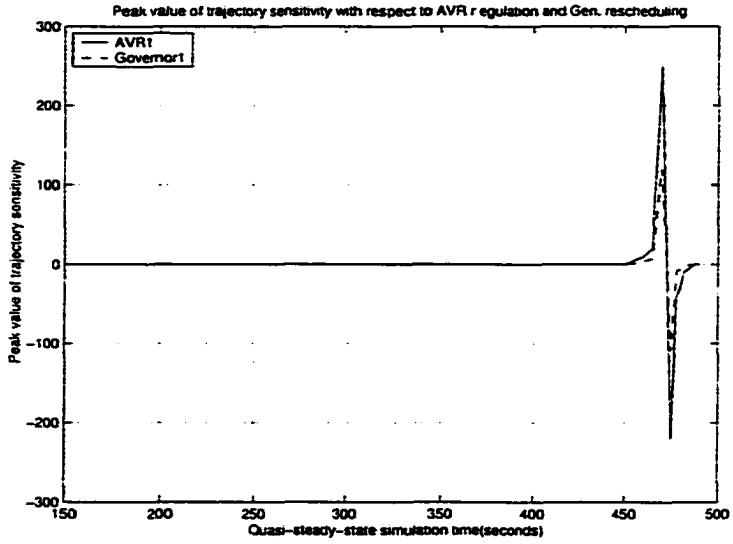

Figure 6.3 Peak values of trajectory sensitivity wrt. V_{ref} and P_{gs0} vs. time

6.6.1.2 Margin sensitivity at the long-term saddle node bifurcation point

At the SNB point, w_4 in the trajectory sensitivity need not be zero any more. It is called margin sensitivity, which is very important for the selection of control measures. In this example, control variables are governor generation setting (P_{gs01} and P_{gs02}), AVR reference voltage (V_{ref1} and V_{ref2}), shunt capacitance (B_{sh3}) and load shedding (P_{l03}). Figures 6.5-6.8 give the margin estimation with

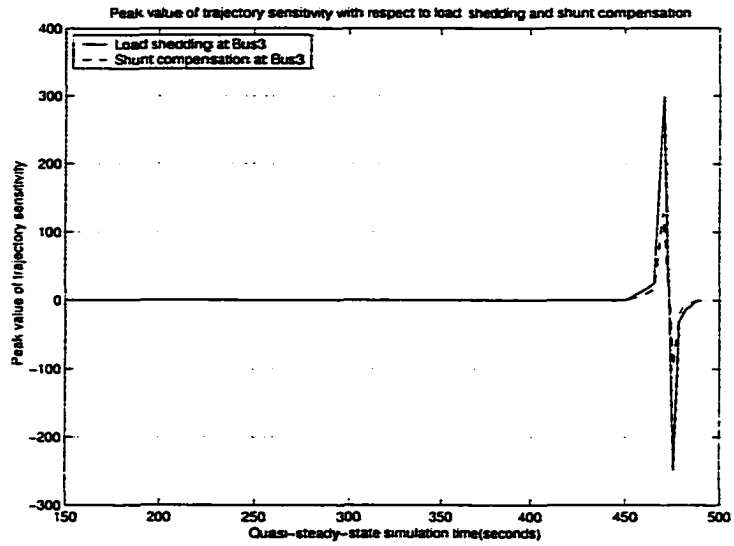

Figure 6.4 Peak values of trajectory sensitivity wrt. P_{l0} and B_{sh} vs. time

respect to these parameters.

6.6.2 Trajectory Sensitivity Application in Scenario Two

6.6.2.1 Identification of the long-term saddle node bifurcation in Case One

Trajectory sensitivity provides the sensitivity of each state variable with respect to four different control parameters selected in this research, which are generation rescheduling (P_{gs0}), AVR regulation (V_{ref}), shunt compensation (B_{sh}) and load shedding (P_{l0}). The peak value of trajectory sensitivity is the primary consideration to determine the long-term SNB point. By evaluating this sensitivity along the system's trajectory, a dramatic increase is observed at $t = 300s$, where a change in sign follows. This corresponds to an equilibrium point approaching then crossing the SNB point. The obtained sensitivities are listed in Table 6.2.

Table 6.2 Peak values of trajectory sensitivity wrt. four controls in Case One

Time(s)	P_{l03}	B_{sh3}	V_{ref2}	P_{gs01}
270	0.49524	0.13498	0.32629	0.09827
280	8.73264	3.47428	6.67434	2.86432
290	17.43258	6.98334	13.47828	5.73288
300	323.72334	137.45922	257.97343	126.89234
310	-282.86323	-102.78932	-200.86231	-98.35629

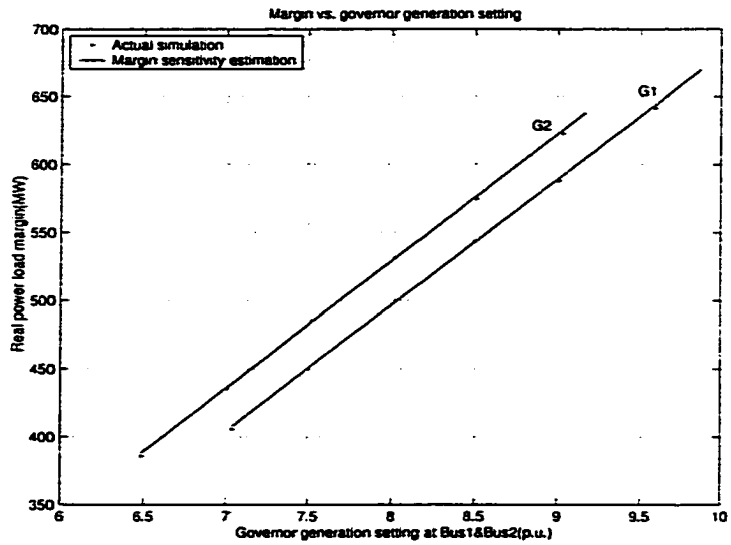

Figure 6.5 Load margin vs. governor generation setting

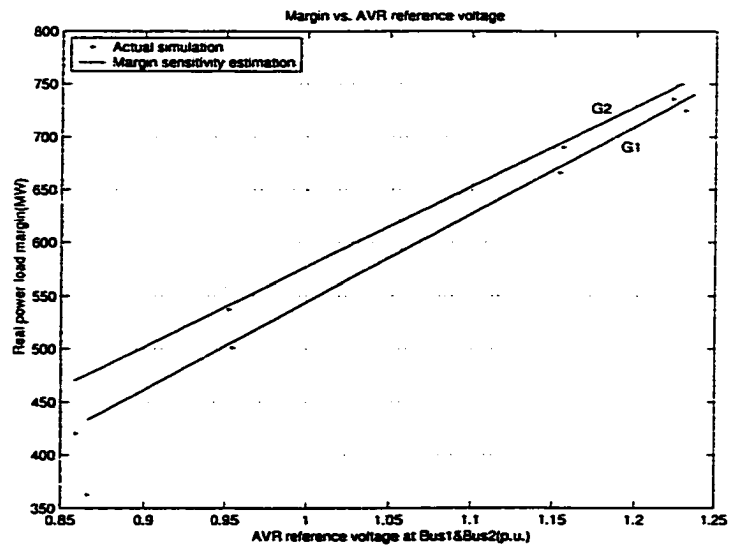

Figure 6.6 Load margin vs. AVR reference voltage

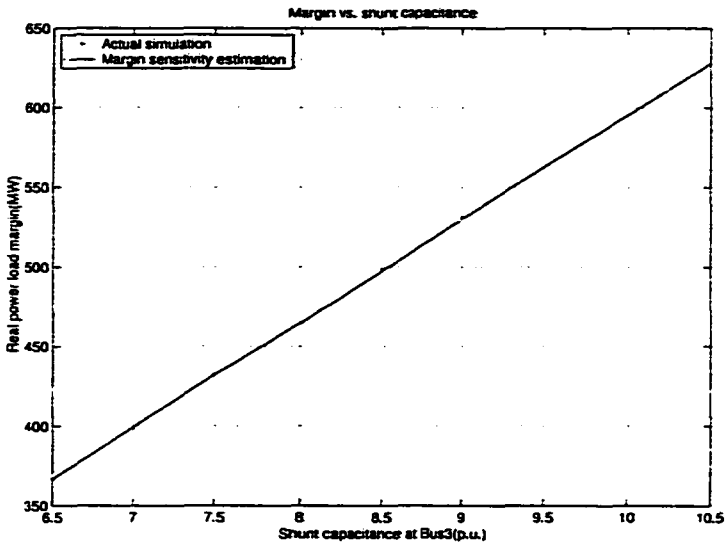

Figure 6.7 Load margin vs. shunt capacitance

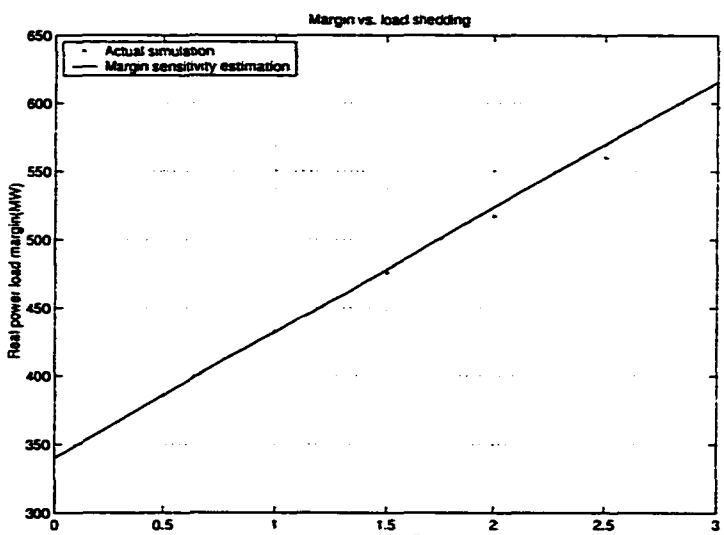

Figure 6.8 Load margin vs. load shedding

6.6.2.2 Identification of the long-term saddle node bifurcation in Case Two

Table 6.3 shows the peak values of trajectory sensitivity with respect to the selected controls at time interval $t = 30s$. It is observed that when $t = 150s$, the sensitivities increase drastically and change the signs afterwards. We identify this time step as the long-term SNB point. Around $t = 200s$, the OLTC reaches its limit and is blocked. The load dynamics become significant which results in a total system collapse. It is the singularity-induced bifurcation that has been identified by $d\alpha$ in Chapter 5.

In this case, there is a clear distance between the long-term SNB point and the SIB point because two different dynamics are considered here.

Table 6.3 Peak values of trajectory sensitivity wrt. four controls in Case Two

Time(s)	P_{l03}	B_{sh3}	V_{ref2}	P_{gs01}
30	0.46327	0.13982	0.32393	0.09978
60	0.46362	0.14024	0.32467	0.10036
90	0.46376	0.14073	0.32456	0.10098
120	5.79232	2.97708	5.08234	1.83635
150	330.99238	136.08827	305.97432	115.9737
180	-19.89837	-12.96381	-17.63595	-10.7563

6.6.2.3 Identification of the long-term saddle node bifurcation in Case Three

The calculation of trajectory sensitivity by applying the simultaneous implicit method involves the whole system Jacobian matrix, whose singularity in turn indicates the long-term voltage instability if J_{xy} is nonsingular. In this research, continuation method is also used to calculate trajectory sensitivity by a partitioned scheme. It needs to evaluate J_{xy} which mainly considers the short-term components and the network configuration. Table 6.4 gives the peak values of trajectory sensitivity with respect to selected control actions at the equilibrium with time interval $t = 100s$.

Table 6.4 Peak values of trajectory sensitivity wrt. four controls in Case Three

Time(s)	P_{l03}	B_{sh3}	V_{ref2}	P_{gs01}
200	0.45628	0.11875	0.28674	0.08423
300	0.45637	0.11882	0.28762	0.08474
400	0.48973	0.12576	0.29612	0.08568
500	3.81494	1.19832	2.85322	1.06142
600	320.97634	131.81729	283.86120	117.83414
610	-294.68334	-95.68423	-223.62315	-82.87662

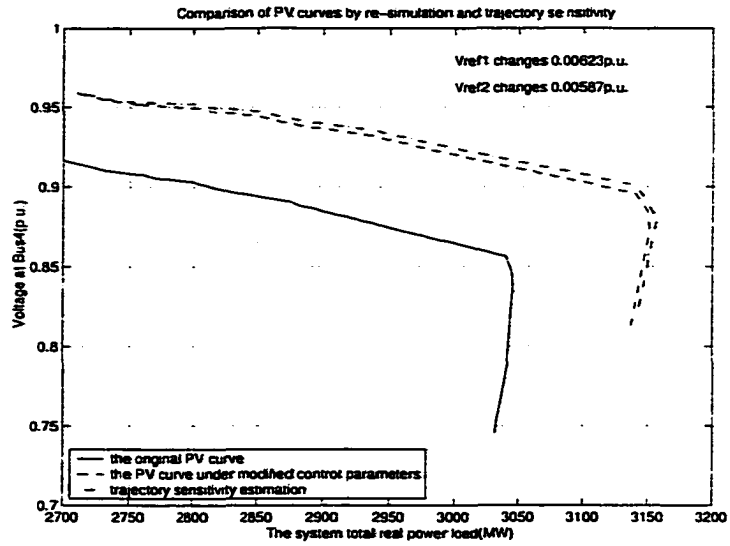

Figure 6.9 Comparison of the PV curves under the changes of V_{ref1} and V_{ref2}

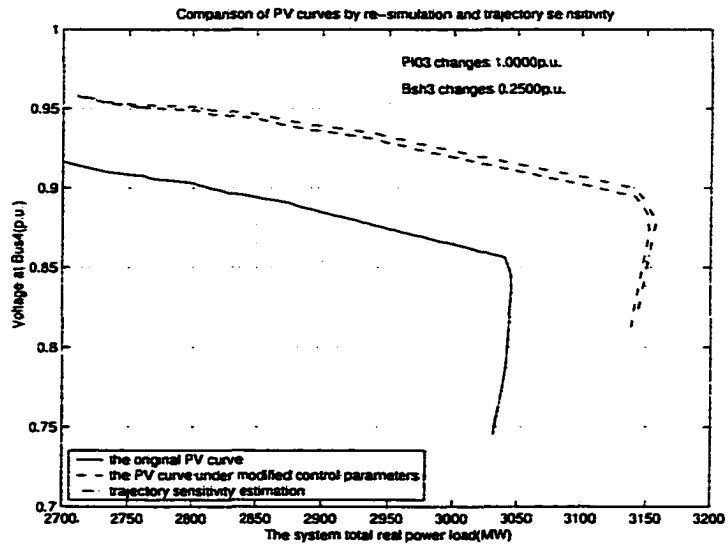

Figure 6.10 Comparison of the PV curves under the changes of P_{l03} and B_{sh3}

It could be observed that the long-term SNB point and the SIB point which has been detected in Chapter 5 (Table 5.2) are very close in this case.

6.6.3 Trajectory Sensitivity for Control Actions

Next, we will show another application of trajectory sensitivity for voltage controls. The system's PV curve could be obtained by the CQSS simulation under a set of control parameters. At each equilibrium on the PV curve, trajectory sensitivity of the state variable with respect to each control is calculated. If the control setting is changed, the new state variable could be obtained by using trajectory sensitivity immediately. Then we can get each new equilibrium on the new PV curve without re-tracing it under modified control variables. By excluding the small error due to the linear sensitivity analysis, this method is computationally-fast compared to the simulation. If a system is very large, it could save a lot of time. It should be noticed however that all the values need to be stored in the computer. The calculation speed is improved at the expense of the large memory. Two cases are given in the following figures which depict the system's PV curves under selected control parameters. Figure 6.9 compares the PV curves through the two different methods by changing V_{ref1} and V_{ref2}, whereas Figure 6.10 gives the comparison of the curves if P_{l03} and B_{sh3} have been modified. The changes of control parameters are also shown in the figures.

7 CONSIDERATION OF CONTROL ACTIONS TO MITIGATE LONG-TERM VOLTAGE INSTABILITY

7.1 Corrective Actions to Restore the Long-Term Voltage Stability

In this research, the objective of corrective control is to restore a long-term equilibrium. It is assumed generally that the load characteristic just after contingency is constant impedance. For this scenario, the base case for the CQSS tracing could be obtained by the power flow solution. However, there is another very special case where the post-contingency load characteristic is constant power load. For such a case, a large amount of load should be shed arbitrarily to get the post-contingency base case [68]. Even for a constant impedance load characteristic, there may not exist an intersection with the PV curve just after the contingency. This could be tackled also in the same way as we deal with the constant power load to get the base case and implement the controls.

Here, corrective control focuses on load shedding, which appears to be the main line of defense against severe disturbances. Load shedding raises fundamental questions such as when, where and how much of the load should be shed.

We notice that shedding load affects the following three curves:

1. The network PV curve: load shedding will enlarge the system's margin if both real power and reactive power load dynamics are considered [12];
2. The long-term load characteristic: load shedding will move the long-term load characteristic to the left (such as from P_A to P_S in Figure 7.1);
3. The short-term load characteristic: load shedding will change this characteristic as well (Appendix E).

Correspondingly, there are both *pre-shedding* and *post-shedding* curves shown in the figures.

7.1.1 Corrective Action: When to Act

Given a specific load-shedding amount, load shedding must take place fast enough to prevent the system from reaching the collapse point. If the control is delayed too much, the system may exit the region of attraction (Appendix E) of the post-control stable equilibrium and lose stability. This process is illustrated in Figure 7.1. In the figure, the dash-dotted line corresponds to the pre-shedding short-term load characteristic while the dashed line is the post-shedding short-term load characteristic.

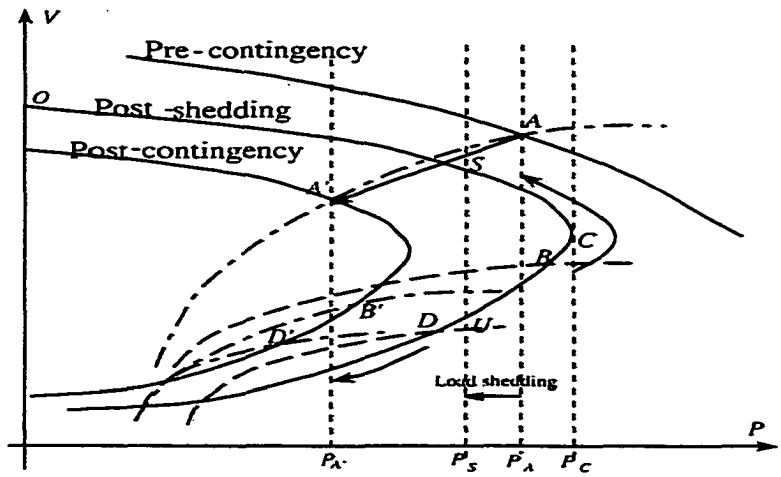

Figure 7.1 Corrective action mechanism by PV curve

Assume a load with an impedance-type short-term characteristic restoring to constant power in the long term. A is a pre-disturbance long-term equilibrium. This severe contingency results in a post-disturbance PV curve that does not intersect the long-term load characteristic $P = P_A$. After the disturbance, the load responds instantaneously with its short-term characteristic and the operating point jumps to A'. Since, at this point, the network real power supply $P_{A'}$ is less than P_A according to the additive load model ((5.1), (5.3) and (5.5)):

$$\begin{aligned} T_P \dot{z}_P &= -z_P + (\frac{V}{V_0})^{\alpha_S} - (\frac{V}{V_0})^{\alpha_T} \\ &= P_s(V)/P_{l0} - P_t(V)/P_{l0} \\ &= (P_A - P_{A'})/P_{l0} > 0 \end{aligned} \tag{7.1}$$

The load dynamics will try to draw more real power by increasing the state variable z_P. This

is equivalent to increasing the load admittance or load current according to different short-term load characteristics. It drives the operating point to a lower voltage. If the load demand and network supply imbalance persists, the system will continuously operate on the intersection of the post-contingency PV curve and the drifting short-term load curve with a monotonically decreasing voltage. This is shown in the figure by a series of dash-dotted short-term load characteristics. Corrective control action yields a new post-shedding PV curve where S represents the stable long-term equilibrium while U represents the unstable long-term equilibrium after the shedding. It has been known that the region of attraction of S is the portion $O-S-C-U$ of the PV curve. In order for the system to be attracted to S, the operating point just after the control should fall in the region of attraction of this equilibrium (Appendix E).

- If the control action takes place at B' and right after this action the operating point is B: Since at this point the load power is larger than P_S ($P_s(V) - P_t(V) < 0$), the load then draws less power by decreasing z_P and as a result, the operating voltage is increased. The dynamic process continues until the power imbalance is reduced to zero, namely a new long-term equilibrium S is reached.
- If the control action is taken at D', where the post-control operating point is D: The load power at D is smaller than P_s. A monotonic voltage collapse is the ultimate end.

Note that in both cases, the control actions are instantaneous and take no time to perform.

7.1.2 Corrective Action: Where to Act

Control actions need the identification of the most effective locations for the implementation. Especially for corrective control, a major concern is to decide which loads are more appropriate to act on to achieve minimal shedding.

Figure 7.2 [30, 69, 70] gives more insight on voltage collapse by the system portrait in the load power space. Here P_1 and P_2 are the real powers of the different loads. The short-dashed line refers to the pre-contingency configuration, the long-dashed line refers to the post-control configuration and the solid line refers to the the post-contingency condition. $\mathbf{S^0}$ is the long-term equilibrium point to which a stable trajectory $\mathbf{S(t)}$ converges. In the load power space, there exists a feasible set outside which the system has no long-term equilibrium. In the figure, the feasible set of post-contingency is limited by a hypersurface Σ. Each point of Σ corresponds to a saddle-node bifurcation of the DAE system. In practice, different points of Σ correspond to different scenarios under consideration.

Assuming that the disturbance takes place at $t = 0$, the system experiences a jump from $\mathbf{S(0^-) = S^0}$ to $\mathbf{S(0^+)}$ which is within the feasible set due to the load sensitivity to voltage. Then the smooth

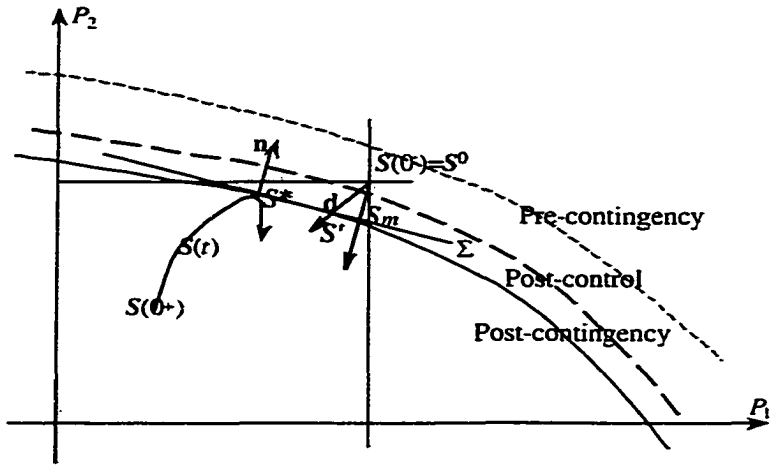

Figure 7.2 System portrait in load space

increases in demand (load restoration) push S to go out of the feasible set. However, after hitting the hypersurface Σ, S(t) can't go any further. In a large-disturbance scenario, loss of generation or transmission equipment causes Σ to shrink so significantly that S^0 ends up outside the post-contingency boundary.

All the possible SNB points form the stability boundary. In Figure 7.2, S^* means the current long-term SNB point on Σ and n is the normal vector to Σ at S^*.

In Appendix C, it is observed that the normal vector is nothing but the negative measure of ISPS (σ_p) [71] vector corresponding to the zero eigenvalue of A_{sys} at saddle node bifurcation. The negative sign means that a decrease of the load in the direction of n leads to regaining the operating equilibrium in Scenario Two.

The aim of corrective control is to restore an equilibrium through different load-shedding strategies, which show up in the load space as different directions. Along each direction there is a different distance between S^0 and the boundary. Corrective control actually looks for a way of restoring equilibrium that minimizes this distance.

The unsolvability of a post-contingency case can be quantified also by Euclidean distance. In [26] and [27], a cost function associated with the power flow mismatch equations is defined and solved. The solution can be thought of as the "best possible" solution to power flow equations. The saddle node

point S_m in the load space corresponding to this solution, is verified as the closest point on Σ to S^0. The direction to this point is then just $-(S^0 - S_m)$, which is parallel to the normal vector at S^*.

It has been verified that left eigenvector associated with the zero eigenvalue of J_{total} approximates the direction of the shortest line segment joining S^0 to the stability boundary. Normal vector to Σ at S^*, is just ζJ_μ where ζ is the left eigenvector corresponding to the trivial eigenvalue of J_{total}. J_μ is the Jacobian of h, f and g, with respect to the parameter μ. Hence, the normal vector defines the most critical direction in the load space.

Since S^0 is an element of the normal ray emanating from S_m, the "optimal" direction to move back to Σ is in the opposite direction to the normal, that is, the measure of ISPS.

7.1.3 Corrective Action: Amount Issue

In Chapter 7.1.1, we have seen that for a given amount of load shedding, there is a time limit for the implementation. Now we will investigate how the amount of load shedding to restore a long-term equilibrium changes with the shedding time t_s. t_s is defined as the elapsed time between the disturbance and the shedding action.

Assume the system takes a specific time t_s from A' to D' (Figure 7.3). PV curves and load characteristic curves shift while implementing load shedding at D'. Accordingly, the intersections between them change with the different amounts of load shedding. The pre-shedding and post-shedding long-term load characteristics are defined as $P_{s,old}$ and $P_{s,new}$ respectively, whereas $P_{t,old}$ and $P_{t,new}$ correspond to the pre-shedding and post-shedding short-term load characteristics. In Figure 7.3, when the system is operated on the lower portion of the PV curve, if $P_{t,new} \geq P_{s,new}$ at t_s, then the load shedding is successful since the system's state is within the region of attraction of the stable long-term equilibrium (S). The additional requirement, that $P_{t,new} > P_{t,old}$, should be met. Load shedding increases bus voltage where the load is going to be shed, which in turn increases the load according to the voltage-dependent short-term load characteristic.

The implementation procedure to determine the amount of load shedding for a given shedding delay t_s can be found in [12, 72].

1. *Step One:* Get the current short-term state which has been solved by the CQSS simulation using the load powers $P_{t,old}$ and $Q_{t,old}$ at t_s when load shedding is going to be performed (D' in Figure 7.3);

2. *Step Two:* Arbitrarily assign new values of the load power, $P_{t,new}$ and $Q_{t,new}$ (D in Figure 7.3), to the location where load is going to be shed. Note here $P_{t,new} > P_{t,old}$ should be imposed;

3. *Step Three:* Calculate the new voltage $V_{t,new}$ at the load by the power flow program. This new voltage must be higher than the current voltage, otherwise go back to *Step Two* and choose larger load values $P_{t,new}$ and $Q_{t,new}$.

4. *Step Four:* Calculate the short-term change in load powers, ΔP_t and ΔQ_t, according to the short-term load characteristic due to the voltage change:

$$\Delta P_t = \frac{P_{l0}}{V_0^{\alpha(t_s)}}(V_{t,new}^{\alpha(t_s)} - V_{t,old}^{\alpha(t_s)}) \tag{7.2}$$

5. *Step Five:* Calculate the amount of load that needs to be shed so that voltages and load powers after load shedding correspond to $P_{t,new}$:

$$P_{t,shed} = P_{t,old} - P_{t,new} + \Delta P_t \tag{7.3}$$

Then,

$$\frac{P_{t,new}}{P_{t,old} + \Delta P_t} = 1 - \frac{P_{t,shed}}{P_{t,old} + \Delta P_t} \tag{7.4}$$

The remaining proportion of the load after load shedding is defined as r_P. If the voltage change stems from the load shedding, r_P must fulfill:

$$r_P = \frac{P_{t,new}}{P_{t,old} + \Delta P_t} \tag{7.5}$$

The same applies to reactive power. This formula can be used for any short-term load characteristic.

6. *Step Six:* Calculate the new long-term load powers, $P_{s,new}$ and $Q_{s,new}$ accordingly.

$$P_{s,new} = r_P P_{l0}(V_{t,new}/V_0)^{\alpha_s} \tag{7.6}$$

7. *Step Seven:* The load shedding is considered successful in the short term if $P_{t,new} > P_{s,new}$ and $Q_{t,new} > Q_{s,new}$. In the absence of these relationships, return to *Step Two* and choose new load values.

Actually, if $P_{t,new} = P_{s,new}$ at the nose point of the post-shedding PV curve, then the minimal load shedding is achieved. As illustrated in Figure 7.3, the whole post-shedding PV curve is unknown and only equilibrium points after the load shedding are obtained by the simulation. Therefore, the amount of load shedding depends on the time selected to shed the load.

Moving $\mathbf{S^0}$ back to the boundary in a direction that is exactly parallel to the normal vector is not always physically feasible due to certain practical problems in the system, for example, only a fraction of load at some buses may be interruptible. Corrective actions should take into account such problems.

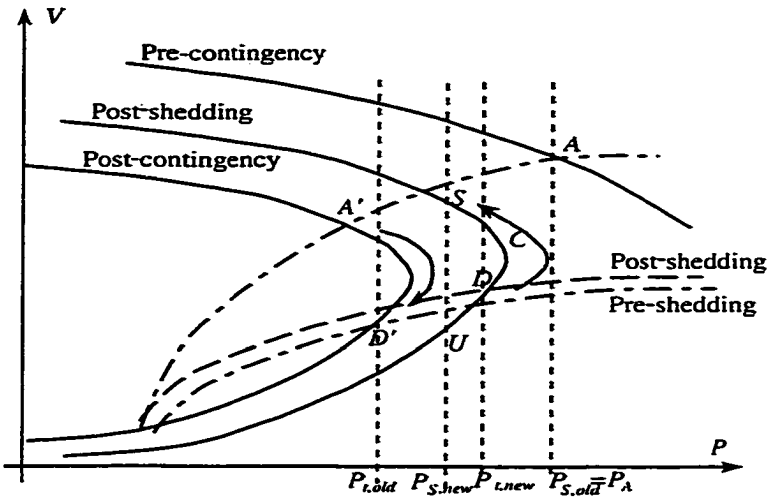

Figure 7.3 Illustration of load shedding at t_s

7.1.4 Margin Sensitivity for Corrective Action

It has been shown that margin sensitivity $\partial\lambda/\partial\mu$ (Appendix C) basically comes from σ_p at the SNB point. Margin sensitivity can be calculated only when the bifurcation occurs at a long-term equilibrium. It is used generally for evaluating the dependence of the margin change on the control variables. For corrective control, there is no long-term equilibrium just after the contingency. The post-contingency PV curve actually consists of a succession of the short-term equilibria driven by the load dynamics until the system reaches the singularity-induced bifurcation. The reason we apply it here, however, is that we presume the nose point of the post-shedding PV curve is also the long-term SNB point. The minimal load shedding would be achieved when the long-term load characteristic after the control is tangent to the nose point of the post-shedding PV curve.

Assume we have implemented load shedding successfully, so that the long-term SNB point is C (Figure 7.3). We may now want to find the best locations to enlarge the stability margin to A. This is the same as the situation in Scenario One, where the security of a solvable point can be quantified by using Euclidean distance in the load parameter space from the power-flow solution to the closest point on Σ. Assume that this solvable point is C, which actually is the nose point of the post-shedding PV curve, and the closest point on Σ is A, which is the pre-contingency operating point. Our aim is to obtain the distance between A and C at the lowest cost by using the most effective controls.

The nose point of the post-shedding PV curve is unknown to us, however, the location should be selected before the control is implemented. In practice, we assume initially that the load has a very large power factor, and load shedding is mostly applied to the real power load. Therefore, the post-shedding PV curve will be the same as the post-contingency PV curve [12, 73]. This is a close approximation to most loads observed in power systems. Hence, margin sensitivity (7.7), which is calculated at the SNB point of the post-contingency PV curve, could be directly applied to choose the control location. To achieve the minimal control, the shedding location corresponds to the largest entry in margin sensitivity with respect to load shedding.

$$\frac{\partial \lambda}{\partial \mu} = -\frac{\begin{bmatrix} v_h^T & v_f^T & v_g^T \end{bmatrix} \begin{bmatrix} h_\mu \\ f_\mu \\ g_\mu \end{bmatrix}}{\begin{bmatrix} v_h^T & v_f^T & v_g^T \end{bmatrix} \begin{bmatrix} h_\lambda \\ f_\lambda \\ g_\lambda \end{bmatrix}} \tag{7.7}$$

7.1.5 Load Shedding: Implementation Steps

According to the above consideration, load shedding can be implemented as follows:

- Action One: For Scenario Two, simulate the post-contingency system response by using the CQSS approximation;
- Action Two: Identify the long-term bifurcation point and the short-term bifurcation point induced by long-term dynamics during load restoration. In the simulation, both t_{C_1} (the long-term SNB point) and t_E could be obtained (Figure 7.5);
- Action Three: Calculate margin sensitivity with respect to load shedding at the long-term SNB point (C_1) of the post-contingency PV curve. Choose the corresponding largest entry in the margin sensitivity as the control location;
- Action Four: Determine the amount of load shedding at this location for a given shedding delay t_s ($t_{C_1} < t_s < t_E$) according to the steps introduced in Chapter 7.1.3;
- Action Five: Repeat Action Four for various shedding delay t_s.

At first, both real power and reactive power load dynamics are considered, which makes a difference between the post-contingency PV curve and the post-shedding PV curve. In Figure 7.4 [5], A' is the

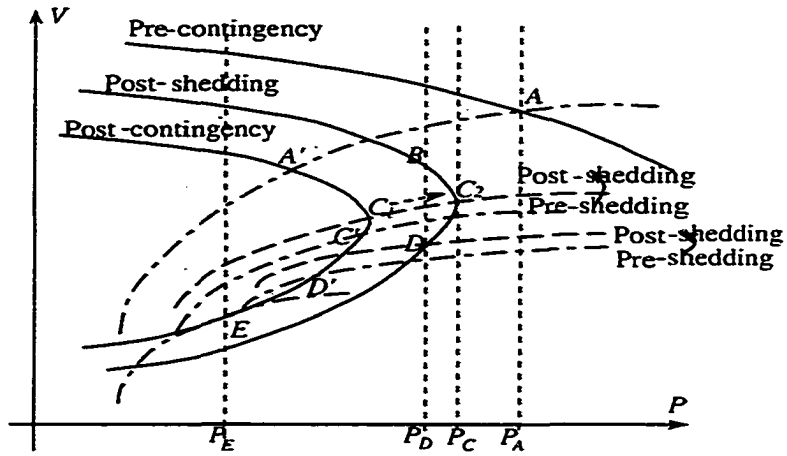

Figure 7.4 Effects of load shedding

post-contingency system operating point. C_1 and C_2 are the pre-shedding and post-shedding SNB points respectively. At $t = t_{C_1}$, C_1 is crossed during the simulation. At $t = t_E$, the instability (Appendix F) is encountered and the system collapses. Note that the ultimate time t_E for an action to be taken corresponds to the loss of stability of the short-term load dynamics.

Let C' be the operating point such that when shedding the amount $P_A - P_C$, the operating point is C_2 after load shedding. t'_C is the time taken to reach C' when no load is shed. When shedding at any time before t'_C, it is enough to shed the amount $P_A - P_C$: the system will be subsequently settled at the stable long-term equilibrium C_2.

After t'_C, the amount of necessary load shedding increases, since a large region of attraction is needed to compensate for a later action. When the load to be shed is $P_A - P_D$, the corresponding time limit for restoring equilibrium B is t'_D, where D' corresponds to the pre-shedding short-term load characteristic, such that the post-shedding one goes through D.

Given C' and D', C_2 and D can be obtained by the method proposed in Chapter 7.1.3. Figure 7.5 [69] illustrates the relationship between the shedding amount and the time delay. The above method is called the general load-shedding scheme.

We can then consider a conservative load-shedding scheme where only the real power load dynamics are taken into account. For a specific time delay t_s when the system is operated at D' (Figure 7.4),

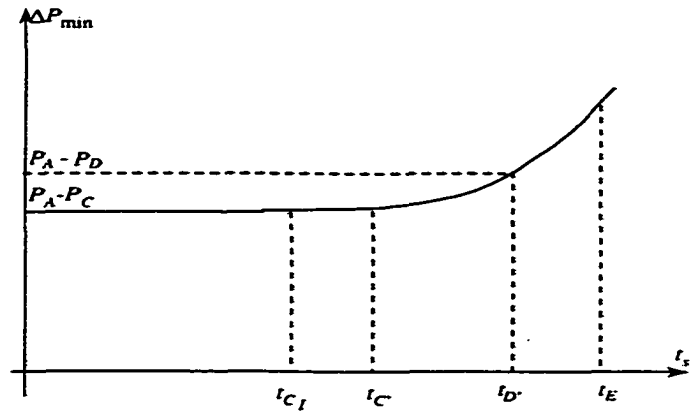

Figure 7.5 Load shedding vs. time

shedding load $P_A - P(D')$ is enough to bring the system back to the stable long-term equilibrium. By implementing this, $P_{t,new} > P_{t,old}$ is automatically fulfilled in this particular case and $P_{s,new} = P_{t,old}$. hence $P_{t,new} > P_{s,new}$. However, compared to the general load-shedding scheme, this load-shedding amount is larger.

Figure 7.6 gives the detailed implementation of load shedding to restore the system's long-term voltage stability.

7.2 Control Actions to Maintain a Sufficient Stability Margin

In Scenario Two, the load-shedding action could save the system from undergoing a voltage collapse. After this control, the system's solvability is restored. It does not ensure the system's voltage stability. however. since the load shedding is targeted to achieve a zero stability margin. The system's situation after corrective control in Scenario Two is similar to a case in Scenario One which a zero margin without any control. Therefore. it is necessary to implement further control actions to increase the system's stability margin and improve the system's operating conditions. Previous work on this topic has been introduced in Chapter 2.

The formulation of control actions to maintain a sufficient stability margin is:

$$Min \qquad f(x) = \sum_{i=1}^{m_{pg}} W_{P_{gs0i}} \Delta P_{gs0i} + \sum_{i=1}^{m_{vr}} W_{V_{refi}} \Delta V_{refi} + \sum_{i=1}^{n_b} W_{B_{shi}} \Delta B_{shi} + \sum_{i=1}^{n_{ls}} W_{P_{l0i}} \Delta P_{l0i} \qquad (7.8)$$

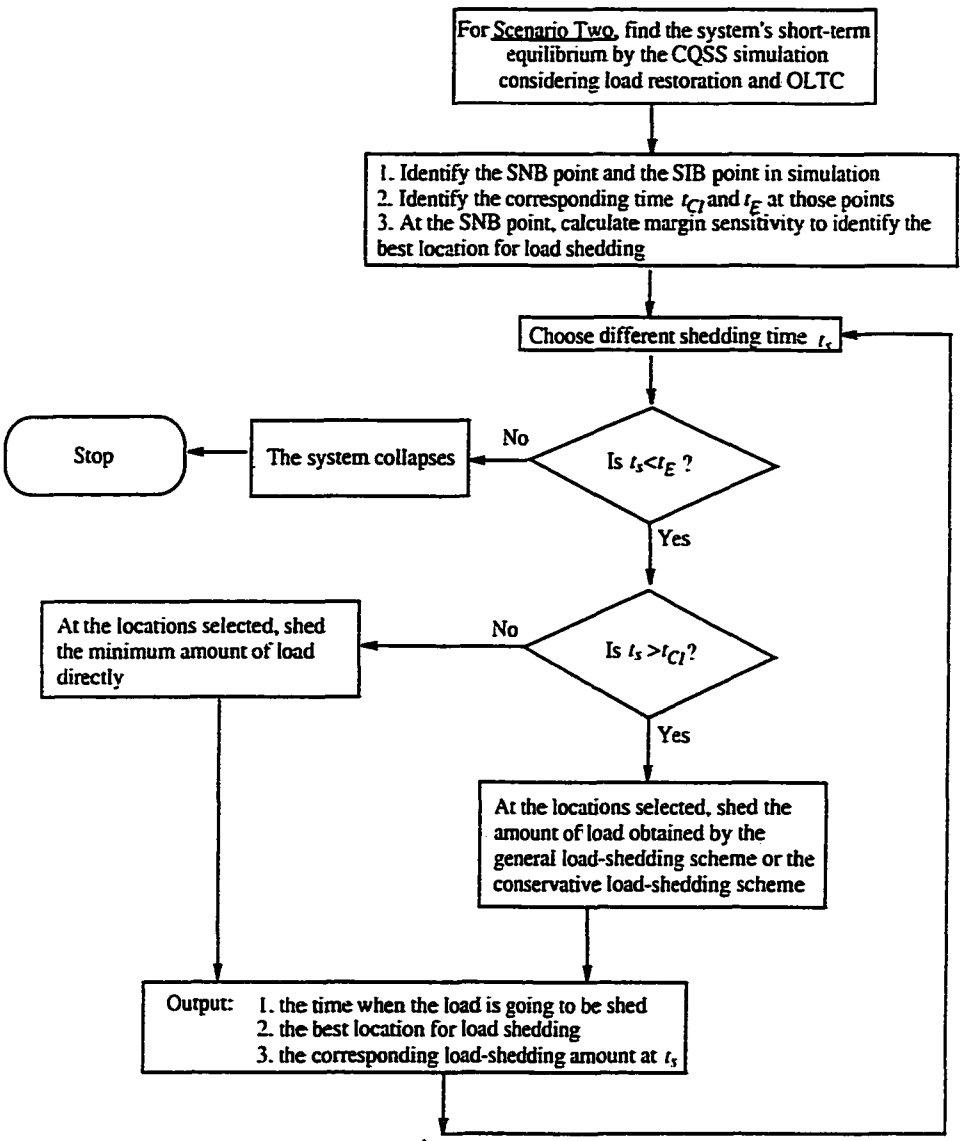

Figure 7.6 Flowchart of the detailed implementation of load shedding to restore the long-term stability

$$\textit{subject to} \quad 0 \le \sum_{i=1}^{m_{pg}} s^{V}_{P_{gs0_i}}(t_{ctr}) * \Delta P_{gs0i} + \sum_{i=1}^{m_{vr}} s^{V}_{V_{ref_i}}(t_{ctr}) * \Delta V_{refi} + \sum_{i=1}^{n_b} s^{V}_{B_{sh_i}}(t_{ctr}) * \Delta B_{shi} + \sum_{i=1}^{n_{ls}} s^{V}_{P_{l0_i}}(t_{ctr}) * \Delta P_{l0i} \le \epsilon_1 \tag{7.9}$$

$$\sum_{i=1}^{m_{pg}} s^{\lambda}_{P_{gs0_i}}(t_n) * \Delta P_{gs0i} + \sum_{i=1}^{m_{vr}} s^{\lambda}_{V_{ref_i}}(t_n) * \Delta V_{refi} + \sum_{i=1}^{n_b} s^{\lambda}_{B_{sh_i}}(t_n) * \Delta B_{shi} + \sum_{i=1}^{n_{ls}} s^{\lambda}_{P_{l0_i}}(t_n) * \Delta P_{l0i} + \lambda(t_n) \sum_{i=1}^{n} K_{lpi} P_{l0i} - \sum_{i=1}^{n_{ls}} \Delta P_{l0i} > x(\sum_{i=1}^{n} P_{l0i} + \sum_{i=1}^{n_{ls}} \Delta P_{l0i}) \tag{7.10}$$

$$\Delta P^{min}_{gs0i} \le \Delta P_{gs0i} \le \Delta P^{max}_{gs0i} \tag{7.11}$$

$$\Delta V^{min}_{refi} \le \Delta V_{refi} \le \Delta V^{max}_{refi} \tag{7.12}$$

$$\Delta B^{min}_{shi} \le \Delta B_{shi} \le \Delta B^{max}_{shi} \tag{7.13}$$

$$\Delta P^{min}_{l0i} \le \Delta P_{l0i} \le \Delta P^{max}_{l0i} \tag{7.14}$$

where $f(x)$ is the cost function representing the total control cost to be minimized. In (7.9) and (7.10), t_{ctr} is the time step where the control is implemented and t_n is the final time step where the SNB point is reached. ϵ_1 is the pre-specified positive value to maintain the voltage. x is the specific margin requirement. $s(t_{ctr})$ and $s(t_n)$ are trajectory sensitivities at t_{ctr} and t_n respectively. As mentioned before, w_4 in trajectory sensitivity at the long-term SNB point is margin sensitivity. The latter is included in $s(t_n)$ as $s^{\lambda}_{\mu}(t_n)$.

The real power generation rescheduling is implemented by ΔP_{gs0}, the generator secondary voltage control is performed by ΔV_{ref}, the shunt capacitance change is defined as ΔB_{sh} and the load shedding is denoted by ΔP_{l0}. M_{pg}, m_{vr}, n_b and n_{ls} respectively are the numbers of the most effective controls. W_i is the cost factor related to each control at bus i.

We describe each constraint and the implementation steps for control actions in the following:

- The first constraint requires that voltage magnitude V_i after the optimization be greater than the values before the optimization. Not all the buses are considered, since to do so is not realistic if the system is very large. To accommodate this constraint, some weak buses [1] are selected through the tangent vector obtained from the predictor. V_i is essentially an algebraic variable which is represented by y in the DAEs. It is linked with control variables by trajectory sensitivity which is defined as $[\partial x(t)/\partial \mu \;\; \partial y(t)/\partial \mu \;\; \partial z(t)/\partial \mu]^T$ based on the DAE formulation.

- The margin enhancement is implemented by the second constraint [74]. The original system

margin is:

$$P_{mrg} = \lambda(t_n) \sum_{i=1}^{n} K_{lpi} P_{l0i} \tag{7.15}$$

Then the margin increase corresponding to margin sensitivity is given as follows:

$$\Delta P_{mrg,ms} = \sum_{i=1}^{m_{pg}} s^{\lambda}_{P_{gs0i}}(t_n) * \Delta P_{gs0i} + \sum_{i=1}^{m_{vr}} s^{\lambda}_{V_{refi}}(t_n) * \Delta V_{refi} + \sum_{i=1}^{n_b} s^{\lambda}_{B_{shi}}(t_n) * \Delta B_{shi} + \sum_{i=1}^{n_{ls}} s^{\lambda}_{P_{l0i}}(t_n) * \Delta P_{l0i} \tag{7.16}$$

Meanwhile load shedding can increase the stability margin by:

$$\Delta P_{mrg,ld} = -\sum_{i=1}^{n_{ls}} \Delta P_{l0i} \tag{7.17}$$

The total margin after the control should meet the following requirement:

$$P_{mrg} + \Delta P_{mrg,ms} + \Delta P_{mrg,ld} > \varepsilon(\sum_{i=1}^{n} P_{l0i} + \sum_{i=1}^{n_{ls}} \Delta P_{l0i}) \tag{7.18}$$

since load shedding also influences the total load power at the base case. Constraint (7.10) is formulated according to the above derivation.

- This problem is solved based on the sensitivity information from the CQSS simulation:

  1. Firstly, the equilibrium of the system is traced until the SNB point has been reached. Note the equilibrium classification that has been discussed in Chapter 6. The CQSS analysis can readily identify a voltage collapse.
  2. Secondly, trajectory sensitivity of all the state variables with respect to each type of control is calculated at each equilibrium during the tracing.
  3. Thirdly, margin sensitivity is obtained directly from trajectory sensitivity at the long-term SNB point.
  4. Finally, the optimal or sub-optimal solution is obtained by linear programming after we select an operating point to implement controls (i.e., t_{ctr}) and formulate the optimization problem.

The equality constraints, i.e., power flow equations including the load change scenario, should generally be considered in the problem formulation. However, linear sensitivity analysis assumes that the equilibrium conditions are usually met so that the power flow equations are eliminated. Although it simplifies the optimization, linear analysis is not very accurate.

In Figure 7.7, the control information depends on the equilibrium where the controls are implemented as well as the SNB point. μ represents the vector including all the control variables. Applying trajectory sensitivity to the control problem has the following characteristics:

- Trajectory sensitivity takes into account the dependence of all the system's variables on the control parameters. Therefore, it is used in (7.9) so as to make the optimized system have a better voltage profile. In some cases, a larger margin may be achieved after optimization, which however would result in a much lower voltage. This constraint can be used to avoid such a situation.
- After the optimization, all the states corresponding to the improved margin can be obtained by trajectory sensitivity. Hence, we can directly get the post-control PV curve without tracing.
- The constraint (7.10) utilizes trajectory sensitivity to meet the system's security requirement by approximating the system's equilibrium status.
- Previous optimizations to increase the system's stability margin consider either the state variable constraint (e.g. voltage) or the margin constraint. In this research, we combine both of them.

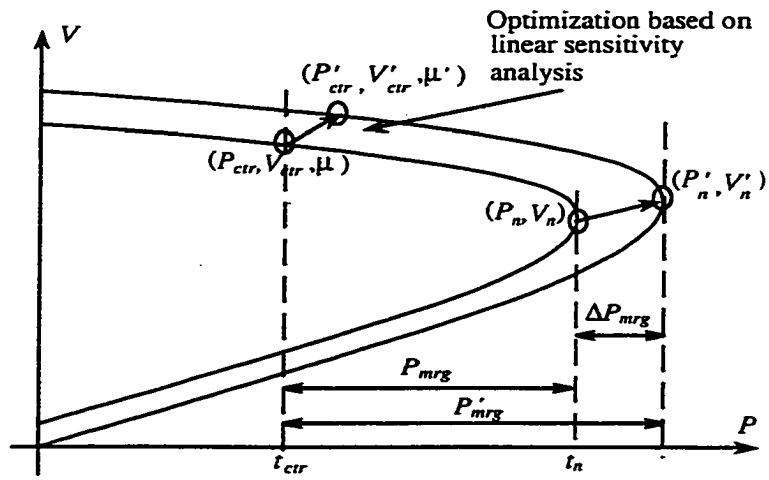

Figure 7.7 Illustration of control actions to increase the margin based on trajectory sensitivity

The same scenario is assumed for the optimized system while using trajectory sensitivity. Furthermore, the optimization has to be implemented within a certain range since trajectory sensitivity is essentially a linear index. Otherwise, nonlinear sensitivity derived from a higher order Taylor expansion or some iterative process may be needed to correct the optimized system. However, they are computationally expensive.

How fast the controls can take actions should also be considered when choosing specific control measures. For transient voltage stability, fast controls are required. Nevertheless, this research is focused on the long-term time scale, hence we have more choices in hand. Moreover, the control to increase the system's stability margin doesn't require the controllers to act very fast, so some slow-response controllers are appropriate. In contrast, when load shedding is implemented to restore the solvability, the response of the controllers should be much quicker in order to bring the system back to the secure operation. The time response characteristics of some general control measures are discussed in depth in [7].

The steps of control actions to increase the system's voltage stability margin are given in Figure 7.8.

7.3 Output Results of the Controls on a Small Test System

In this section, the simulation results of the control actions on the small test system are presented for Scenario Two and Scenario One respectively:

- Load shedding to restore the long-term stability for the system in Scenario Two;
- Control actions to maintain a certain stability margin for the system in Scenario One.

7.3.1 Load Shedding to Restore the Long-Term Voltage Stability

7.3.1.1 Margin sensitivity for load shedding

We focus on the load-shedding strategy based on Case Two in Scenario Two. In Chapter 5, the post-contingency PV curve has been obtained while considering both the tap dynamics and the load-self-restoration mechanism. This curve provides a basis for the corrective control analysis. However, at first, the reason why margin sensitivity, which should be calculated from the long-term equilibrium, can be applied for Scenario Two, is explained briefly below.

In Scenario Two, any short-term equilibrium on the trajectory before the long-term SNB point, has to be interpreted as follows: if this equilibrium were a long-term equilibrium, it would be stable. In the large-disturbance scenario, this point on the PV curve is not an equilibrium: there is no such equilibrium any longer, as already mentioned. By merely lowering the set-point V_2^0, one can figure out this point as a long-term equilibrium, with all system variables left at their current values. The total system Jacobian J_{total} has zero eigenvalue at the long-term SNB point. This means that for a smaller load demand P_0 or set-point V_2^0, the long-term load characteristic (a vertical line) is tangent to the PV

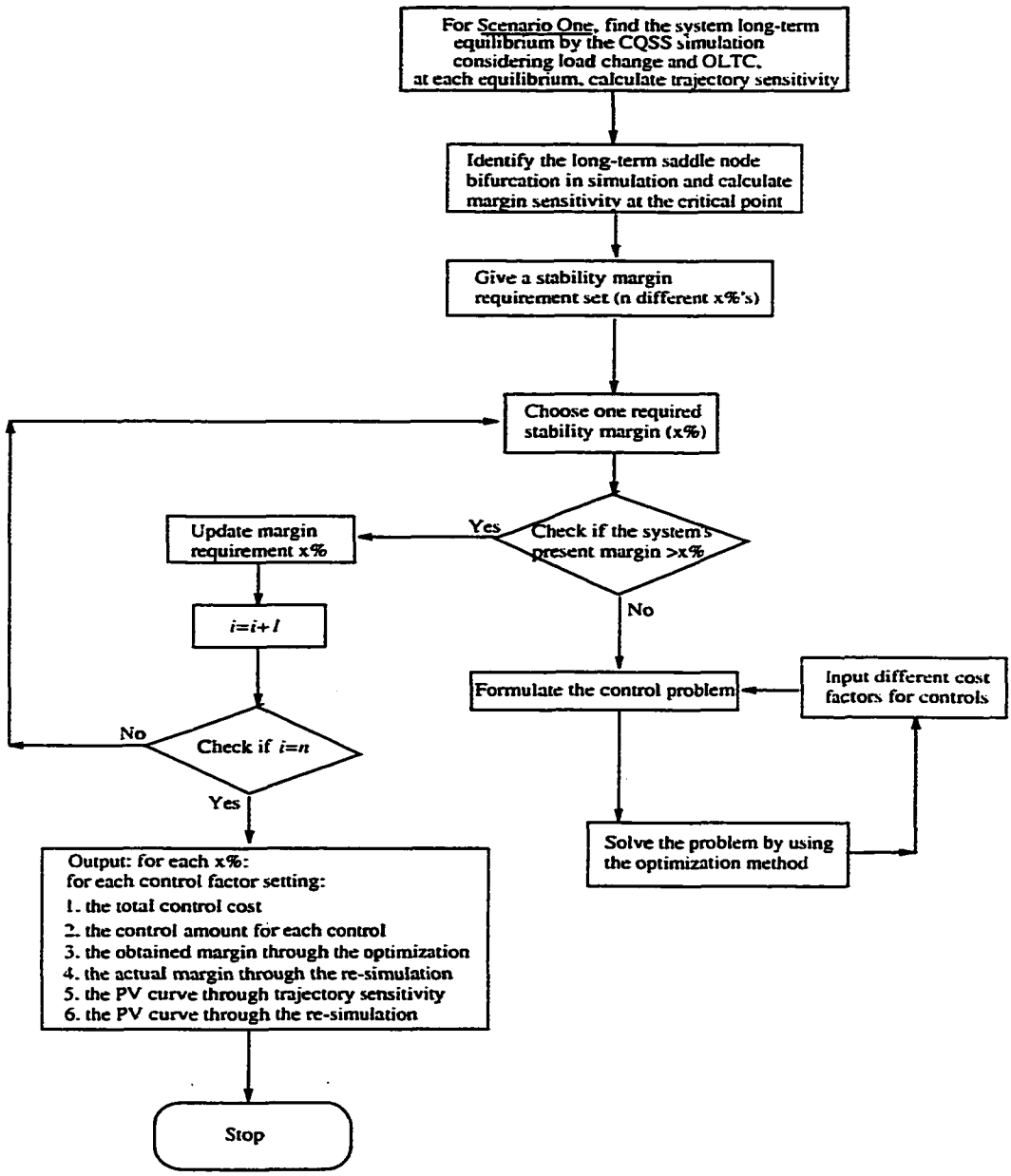

Figure 7.8 Flowchart of steps of the control actions to increase the stability margin

curve at this point. This point generally is also the maximum load point since both the tap changer dynamics and the load self-restoration mechanism try to restore the load to constant power.

We calculate margin sensitivity for the location selection of load shedding. Table 7.1 gives margin sensitivity with respect to the selected control variables of this small test system. Note that only one location can be chosen for load shedding in this system. According to this sensitivity, the most appropriate locations for implementing controls are selected. Table 7.1 shows that load shedding and AVR regulation are the most effective control measures to save the system.

Table 7.1 Margin sensitivity wrt. the selected control variables

Controls	Margin sensitivity
P_{gs01}	0.103244
V_{ref2}	0.328343
B_{sh3}	0.157323
P_{l03}	0.563432

7.3.1.2 Load-shedding schemes

- General load-shedding scheme: We implement the load-shedding scheme introduced before, step by step, and show the results as follows. Choosing different load-shedding time t_s, the loads which should be shed to bring the system back to the stable operation are listed in Table 7.2, as well as the different values of $P_{t,new}$, $P_{t,old}$ and $P_{s,new}$. Figure 7.9 gives the voltage changes at Bus3 and Bus4 with respect to time when shedding load at time instant $t = 170s$. As expected, voltages come back to acceptable values instead of collapsing. We also plot the minimum required load shedding as a function of time in Figure 7.10.

- Conservative load-shedding scheme: Given the time delay t_s, we directly shed load at Bus3 with $P_{s,old} - P(t_s)$. Compared to the above scheme, this value is a little larger. Figure 7.11 gives the voltage changes at the same buses as in Figure 7.9. It shows that the voltage is higher than the previous one due to the greater load shedding. Correspondingly, the load-shedding amount is plotted as a function of time in Figure 7.12. As expected, the amount is a little larger than the one in Figure 7.10.

Table 7.2 Different load shedding vs. shedding time

$t_s(s)$	$P_{t,new}(MW)$	$P_{t,old}(MW)$	$P_{s,new}(MW)$	$P_{shed}(MW)$
50	4300	4076.8732	4320.5027	279.49728
75	4300	4120.6255	4319.7626	280.23736
100	4300	4172.8974	4319.2002	280.79983
125	4300	4216.0036	4319.0268	280.97324
150(t_C)	4320	4298.9128	4318.5918	281.40822
160	4320	4318.7873	4317.0433	282.95671
170	4320	4300.9281	4306.8276	293.17243
180	4300	4280.7439	4282.8947	317.10532
190	4280	4261.9895	4251.9032	349.09682
200(t_E)	4260	4239.8798	4217.9343	382.06572

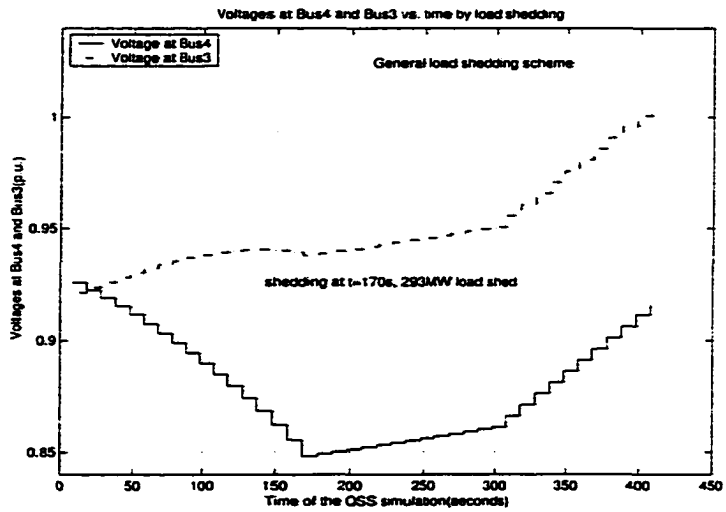

Figure 7.9 System response due to the general load-shedding scheme

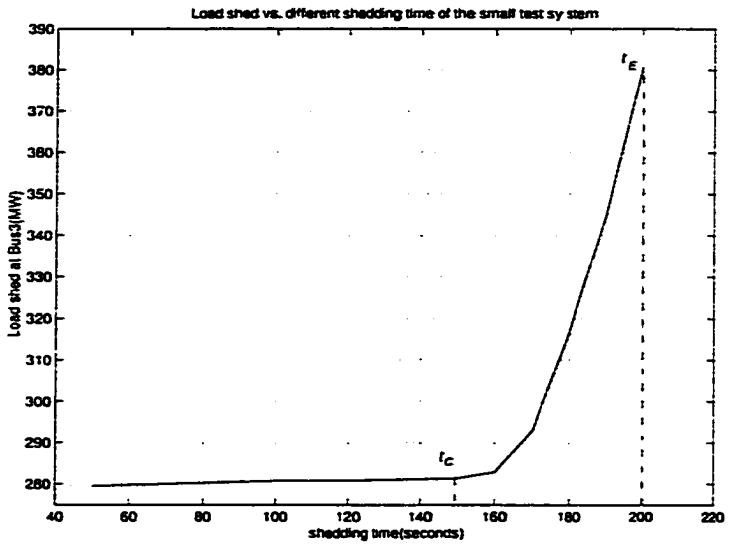

Figure 7.10 Load shedding vs. time in the general load-shedding scheme

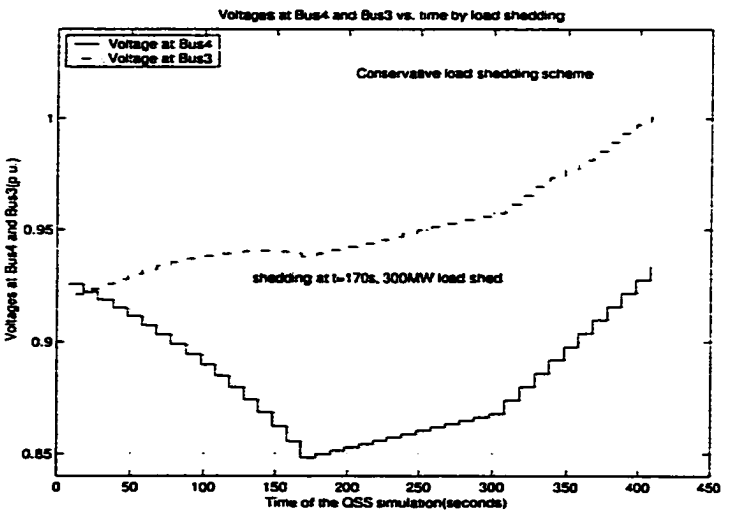

Figure 7.11 System response due to the conservative load-shedding scheme

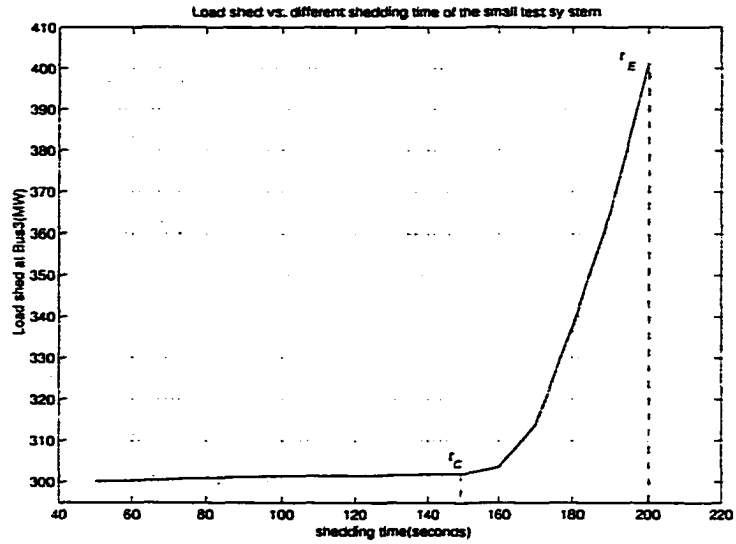

Figure 7.12 Load shedding vs. time in the conservative load-shedding scheme

7.3.2 Control Actions to Increase the Voltage Stability Margin

Referring to the CQSS simulation results for Scenario One in Chapter 4, we find that the system's stability margin is 12% of the base case load level. This margin may not be sufficient if the stability requirement is high. Therefore, control actions need be further implemented based on the same system conditions applied to the CQSS simulation. Here, the objective of the control is to increase its post-contingency voltage stability margin from 12% to 20% with minimum control cost. To achieve this, w_4 in the trajectory sensitivity at the SNB point has been computed for all the applicable control variables in Chapter 6. Table 7.3 lists the control actions of five different control schemes obtained by the proposed approach for different assumptions of control cost factors. The bold number in the table indicates the optimal control amount.

Scheme1 is derived by assuming that all the control actions have the same cost factor. Since margin sensitivities with respect to AVR reference voltages are much higher than those with other control variables, the obtained optimal control merely involves the changes of the most effective AVR reference voltages. Scheme2 gives another control strategy where the control costs for rescheduling real power generations are assumed to be the cheapest. Note that this scheme results in a slight system frequency decrease due to the speed droop characteristics of generator governors. Similarly, Scheme3 corresponds to shedding loads at Bus3 and adding shunt capacitance at this bus. Scheme4 performs the generator

secondary voltage control, combined with the addition of a shunt capacitance at Bus3. In Scheme5, load shedding is considered the only control action to enhance the margin. Table 7.4 gives the verified results of these control schemes with the CQSS simulation. Clearly, all of these control strategies have achieved the expected stability margin requirement. And most of them involve one or two control actions. The iteration number in the second column corresponds to the number of times that the linear optimization is performed by using MATLAB. It shows that the sensitivity-based linear optimization approach works quite reasonably for the control strategy design.

After the optimization, we can obtain the whole PV curve directly from the trajectory sensitivity calculated during the original tracing. Figure 7.13 compares the approximate PV curve without tracing and the exact PV curve by re-simulation under the modified control parameters in Scheme4. It is observed that these two curves coincide very well in the beginning. The small difference at the end of the curves comes from the cumulative error of trajectory sensitivity and the linearity of the sensitivity analysis.

Table 7.3 Changes of control variables in five control schemes

Scheme no.	Variables for the control	Weight factors	Control amount($p.u.$)
Scheme1	V_{ref1}	1.00	0.0121
	V_{ref2}	1.00	0.0134
	others	1.00	0.00
Scheme2	P_{gs01}	1.00	0.4073
	P_{gs02}	1.00	0.3134
	others	40.00	0.00
Scheme3	P_{l03}	1.00	−1.9838
	B_{sh3}	1.00	0.5
	others	40.00	0.00
Scheme4	V_{ref2}	10.00	0.0132
	B_{sh3}	1.00	1.5
	others	40.00	0.00
Scheme5	P_{l03}	1.00	−2.4796
	others	40.00	0.00

7.4 Concluding Remarks

A systematic approach has been proposed to mitigate the long-term voltage instability. Basically, we have talked about the CQSS simulation, which applies two different parameterization strategies to consider load increase in Scenario One and load restoration in Scenario Two respectively, trajectory

sensitivity, load shedding to restore the stability as well as control actions to increase the stability margin. From Chapter 4 to Chapter 7, the overall methodology is demonstrated through a small test system. In Chapter 8, the simulation results of a larger system, the New England 39-bus system, will be provided by applying the same procedure that has been tested on the small system.

Table 7.4 Voltage stability margin with five control schemes

Scheme no.	Iterations	Max. total load(MW)	Actual margin(%)	Error(%)
Scheme1	2	3241.2734	20.0471	0.0471
Scheme2	2	3239.6723	19.9879	-0.0121
Scheme3	1	3240.8982	20.0333	0.0333
Scheme4	2	3241.0832	20.0401	0.0401
Scheme5	2	3240.5929	20.0220	0.0220

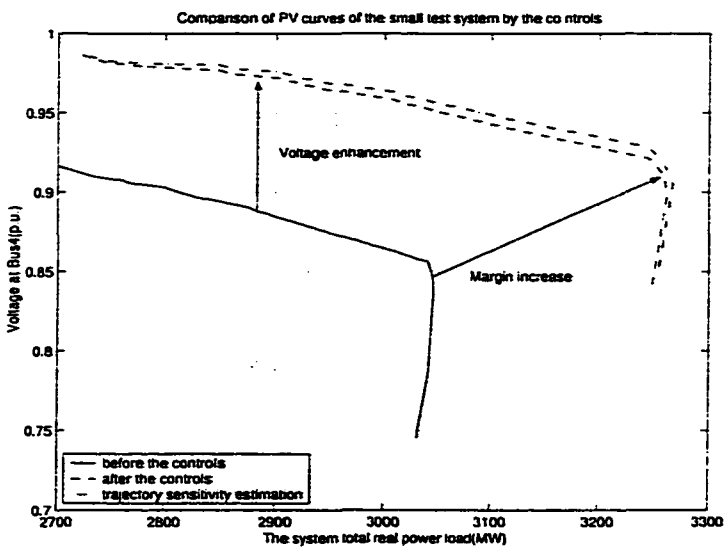

Figure 7.13 PV diagram comparison by tracing and trajectory sensitivity

8 NUMERICAL RESULTS ON THE NEW ENGLAND TEST SYSTEM

8.1 Overview of the Simulation Procedure

The proposed CQSS based approach to mitigate long-term voltage instability has been tested on a small test system. In this chapter, it is applied to the New England 39-bus system. This system is well known in voltage stability analysis. Tests on this system are involved in the following aspects:

- The CQSS simulation for Scenario One includes:
  - Tap implementation and load increase in the equilibrium tracing;
  - The long-term SNB identification by trajectory sensitivity and continuation parameter;
  - Margin sensitivity calculation at the long-term SNB point;
- The CQSS simulation for Scenario Two includes:
  - Tap implementation and load restoration in the equilibrium tracing;
  - The long-term SNB identification by trajectory sensitivity;
  - The SIB identification by continuation parameter;
- Load shedding to restore the system's solvability based on Scenario Two;
- Control actions to increase the voltage stability margin based on Scenario One;

All the programs are developed in Fortran language combined with Matlab.

8.2 Test System

The New-England 39-bus system is employed here to demonstrate the efficacy of the proposed methodology to mitigate the long-term voltage instability. The one-line diagram of this system and the complete data of this system can be found in Appendix G [75]. The overall modeling includes 39 buses and 48 lines.

The modeling consists mainly of the following:

- For the CQSS tracing for Scenario Two, all loads are modeled as thermostatic loads;
- For the CQSS tracing for Scenario One, before the complete restoration, only the buses after the OLTCs are modeled as constant impedance loads and the other buses are constant power loads. After the complete restoration, all the loads are constant power loads (Appendix E);
- Three OLTCs are installed between Bus2 and Bus3, Bus19 and Bus16, as well as Bus29 and Bus26;
- Each OLTC has an operating range of $0.8 - 1.1$, the step size of the tap ratio is set as 0.006;
- Each generator uses the two-axis dynamic model, considering the excitation control, the speed governor, the field and armature current limits as well as the real power generation limit, as described in Chapter 3;
- No generator is allowed to have terminal voltage higher than $1.1 p.u.$ especially when its secondary voltage control is utilized to increase system voltage stability;
- Shedding load means shedding both the real and reactive parts of the load, while maintaining a constant power factor;
- The minimum practically acceptable voltage stability margin of the system, is arbitrarily assumed to be 10%;
- The system's scenario for the CQSS tracing after the restoration in Scenario One is defined as: all the loads increase with constant power factors, and all the generators participate in the load pick-up at the same rate.

For the specific system scenario and under the normal conditions (without any contingency), the system has a voltage stability margin of $1257.1 MW$ for the base case at a total load level of $6142.2 MW$. The system's maximum load at the long-term saddle node bifurcation point is $7398.2 MW$. Therefore, the system at the base case has a sufficient stability margin 20% which is much larger than the required security level of 10%.

8.3 CQSS Simulation for Scenario One

8.3.1 Equilibrium Tracing: λ As Continuation Parameter

The contingency simulated for Scenario One in this case is the outage of the generator at Bus33 at the base case mentioned above. After the contingency, due to the voltage dependent short-term

load characteristic, the system's post-contingency base case can be established. At this point, the system's total real power load is $5980.3MW$. Hereafter, the CQSS simulation is adopted to obtain more information on the system's voltage stability.

- **Step One: During the load restoration**

  In this step, only tap dynamics are considered to restore the system's load to the pre-contingency level. The OLTCs begin their actions $20s$ after the contingency. The system's real power load is recovered to $6140MW$ when $t = 180s$. The voltages at the distribution-side buses of the OLTCs increase. Figure 8.1 shows the voltages at Bus2, Bus19 and Bus29 during the load restoration and Figure 8.2 gives the changes of voltages at Bus3, Bus16 and Bus26 with respect to time.

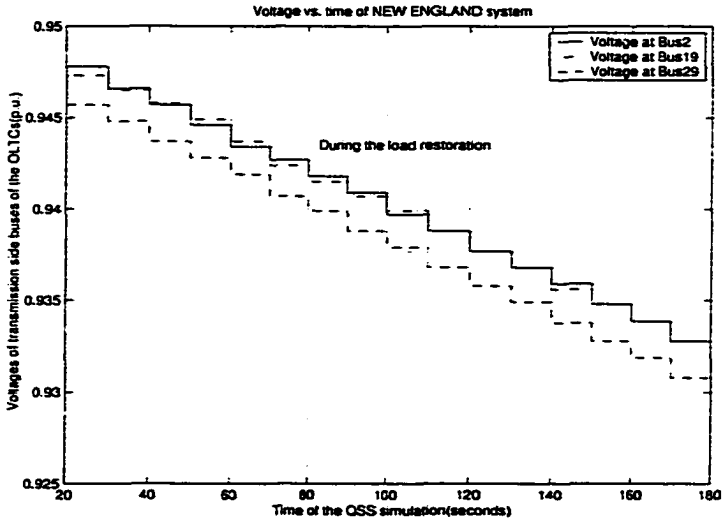

Figure 8.1 Transmission-side voltage change vs. time during the load restoration

- **Step Two: After the complete restoration**

  Once the complete restoration is achieved, the system settles down at a long-term equilibrium which is stable. For Scenario One, in order to identify the long-term voltage instability of the system, we have to increase the load and find out the maximum real power that the system can transfer. Therefore, load change with respect to time, is taken into account now. For this system, the real power load is assumed to be increased by $10MW$ each ten seconds.

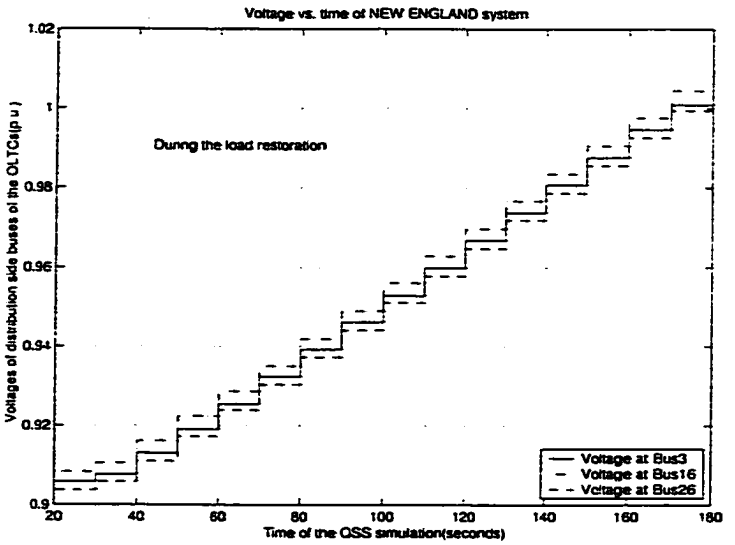

Figure 8.2 Distribution-side voltage change vs. time during the load restoration

Table 8.1 Step size based on the load increase

Time(s)	$P_t(MW)$	Step size
200	6160.00	0.39436
250	6210.00	0.39241
300	6260.00	0.39043
350	6310.00	0.38852
400	6360.00	0.38647
450	6410.00	0.38450
500	6460.00	0.38244

Again we assume that the system's load level at a specific time instant is known to us. By adjusting the step size in continuation method, we can trace the system's trajectory until the long-term SNB point is reached. The step size doesn't depend on the absolute value of the system's load power. Table 8.1 shows the real power loads and the step sizes at different time steps. Furthermore, while the load increases slowly, voltages at those buses on the distribution side of the OLTCs decrease. Then the OLTCs are re-activated and try to maintain the voltage. Figure 8.4 shows the voltage curves at these buses with respect to time after the complete restoration is achieved. Figure 8.3 gives the transmission-side voltages of the OLTCs. It is observed that the taps between Bus2 and Bus3 and between Bus16 and Bus26 reach their lower bounds at $t = 500s$ while the tap between Bus19 and Bus29 is blocked at $t = 520s$. After the limits, the OLTCs perform like regular transformers since they can't regulate voltage any more. When several generators hit their field current and armature current limits, the system finally collapses at $t = 580s$. When using the CQSS simulation, we can obtain the complete system PV curves shown in Figure 8.5.

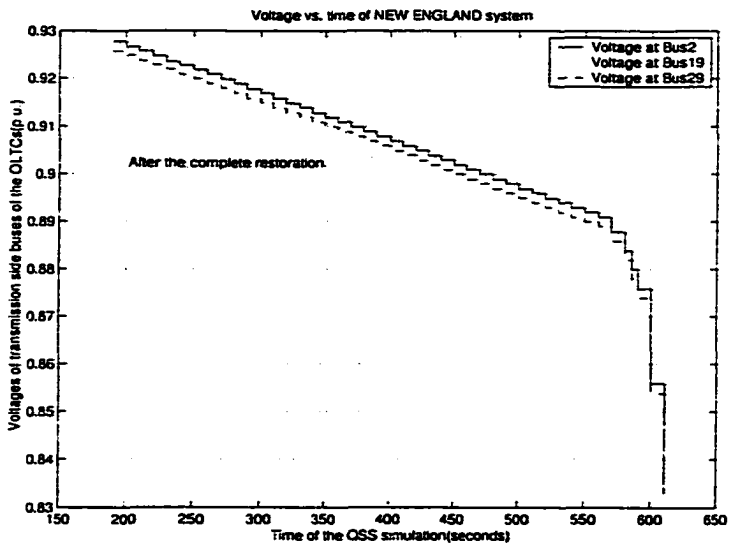

Figure 8.3 Transmission-side voltage change vs. time after the complete restoration

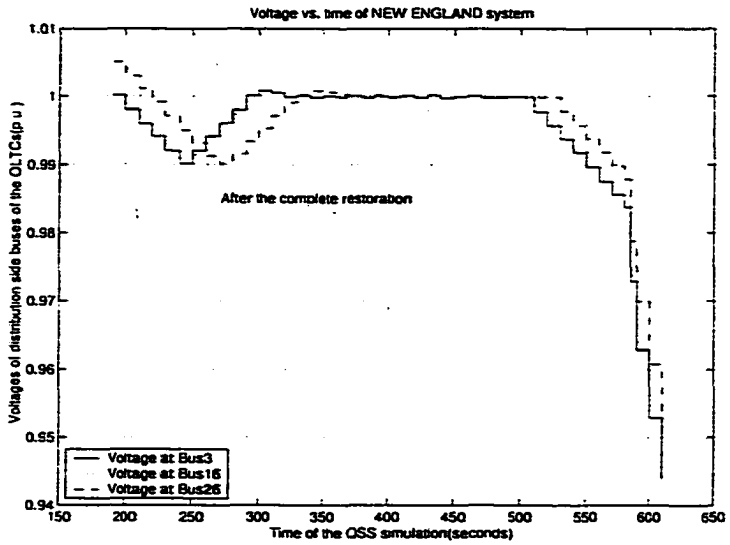

Figure 8.4 Distribution-side voltage change vs. time after the complete restoration

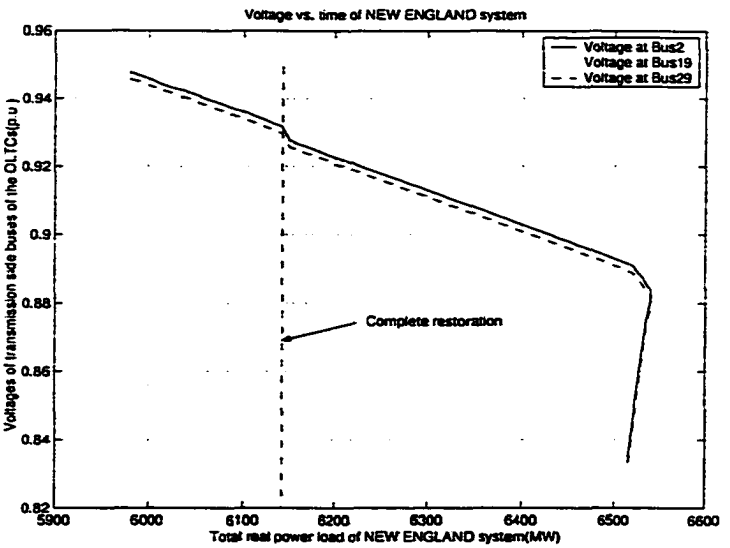

Figure 8.5 PV diagram by using the CQSS simulation

8.3.2 Identification of the SNB and SIB points

8.3.2.1 Identification of SNB by trajectory sensitivity

First, trajectory sensitivity proposed in Chapter 6 is applied here to identify the long-term SNB point. During the simulation, trajectory sensitivity is also calculated to obtain the control information of the system's state variable at time interval $t = 10s$. As shown before, it tends to a large positive value and then becomes a large negative value as the SNB point is crossed. Figure 8.6 shows the change of its peak value with respect to AVR reference voltage at Bus31 and Bus35 while Figure 8.7 shows the change of its peak value with respect to load shedding at Bus3 and Bus39. At the SNB point, all sensitivities change signs together.

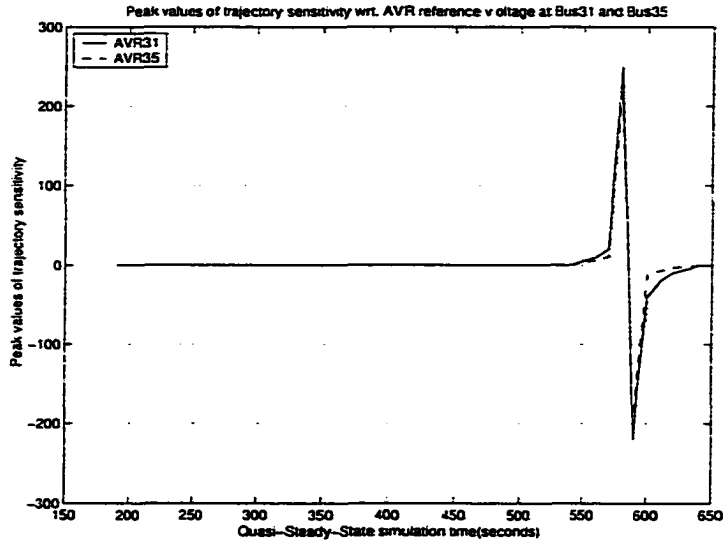

Figure 8.6 Peak values of trajectory sensitivity wrt. V_{ref} vs. time

8.3.2.2 Identification of SIB by continuation parameter

In the predictor, null $d\lambda$ implies the singularity of J_{xy}. Table 8.2 shows the values of $d\lambda$ in the last five steps. In these steps, one state variable other than λ is selected as the continuation parameter. For the New England system, the load parameter λ is zero after the complete restoration is achieved and it increases according to the step size until the bifurcation occurs at a load level of $6540MW$, where a nearly zero $d\lambda$ is detected.

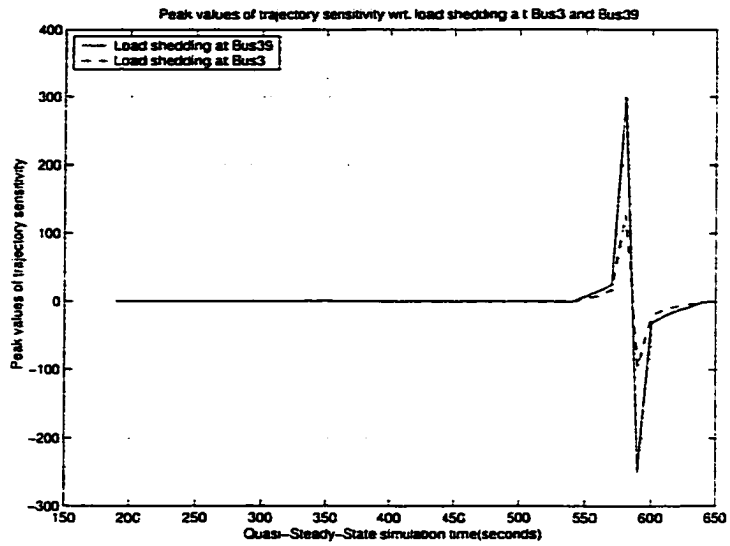

Figure 8.7 Peak values of trajectory sensitivity wrt. P_{l0} vs. time

Up to the saddle node bifurcation point, there are two generators (G30 and G32) hitting their armature current limits and two other generators (G31 and G35) hitting their field current limits. G35 also reaches its real power limit. Figure 8.8 shows the AVR responses of G30, G32 and G38, respectively. Clearly, the AVR output increases linearly until the armature current limit is reached; afterwards, it takes a sharp decline and stays on the AVR limit determined by the constant armature current limit. Figure 8.9 depicts another situation, where the AVR output is maintained at the constant limit after the generator hits its field current limit. This figure gives the AVR responses of G35, G31 and G36, while the field current limit is considered. The terminal voltages and the reactive power outputs of three generators (G35, G30 and G32) are respectively shown in Figure 8.10 and Figure 8.11. In the above figures, it is found that G32 reaches its limit at $t = 510s$, G30 gets to its limit at $t = 520s$, G31 hits its limit at $t = 540s$ and finally G35 attains its limit at $t = 560s$. It is observed that each generator experiences a gradual voltage drop before hitting its limit. Once the generator hits either the armature or the field current limit, however, a sharp voltage decline occurs.

Table 8.2 $d\lambda$ in the last five steps

Time(s)	550	560	570	580	590
$d\lambda$	0.04858	0.04761	0.04674	0.04583	-0.04758

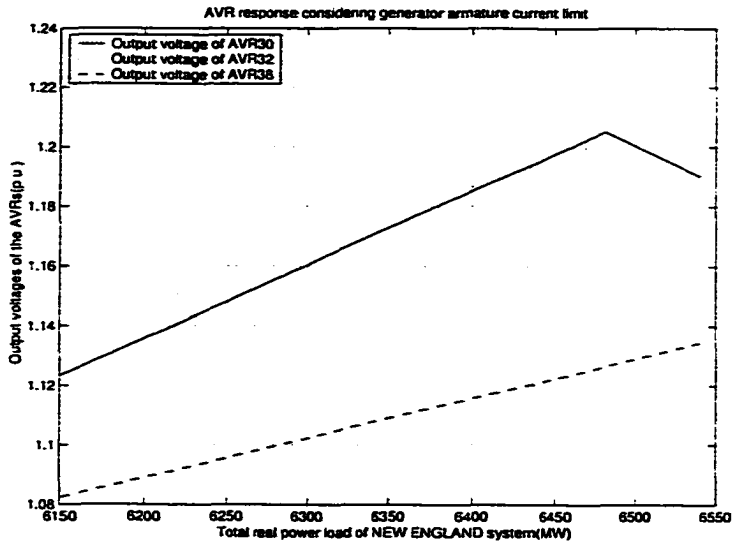

Figure 8.8 AVR responses of G30, G32 and G38 vs. the real power load

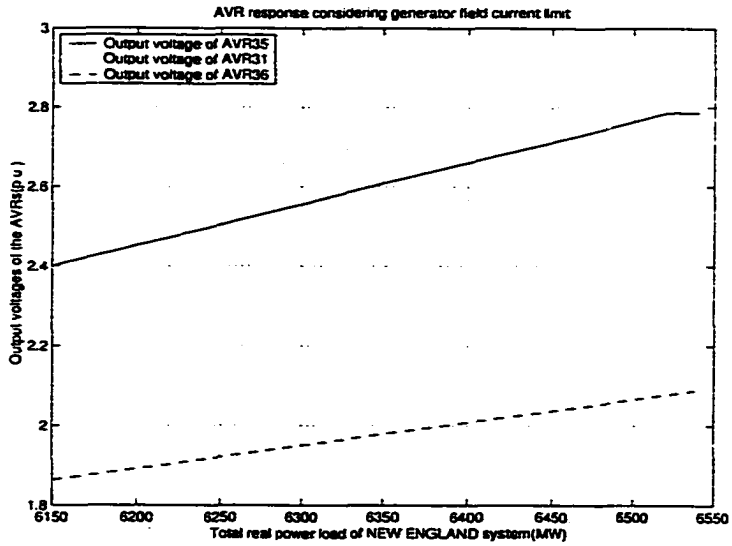

Figure 8.9 AVR responses of G35, G31 and G36 vs. the real power load

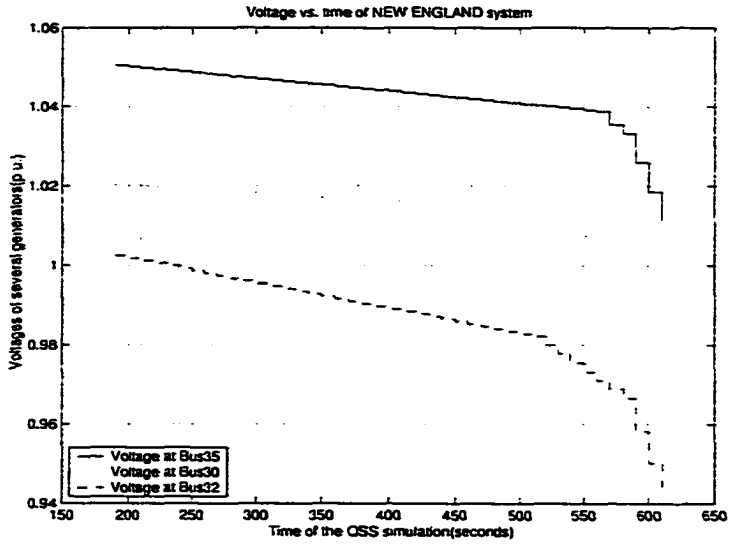

Figure 8.10 Terminal voltages of G35, G30 and G32 vs. time

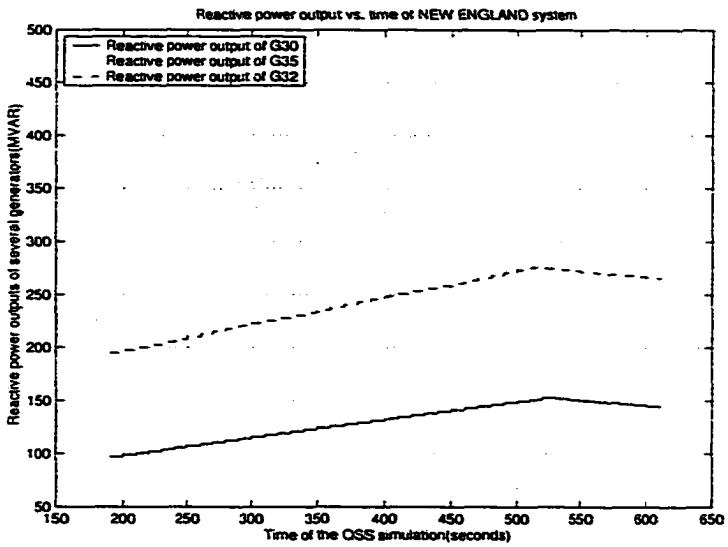

Figure 8.11 Reactive power outputs of G35, G30 and G32 vs. time

8.3.3 Margin Sensitivity at the Long-Term SNB Point

As mentioned before, trajectory sensitivity at the long-term SNB point can be related to margin sensitivity. Here, a set of parameters are selected to analyze their influence on the voltage stability limited transfer capability.

The governor generation setting P_{gs0} (Figure 8.12) determines the long-term contribution of the machine to the load increase of the system. Changing P_{gs0} will shift the governor's droop characteristic curve in a parallel direction. It has been previously observed that, by changing the settings, we can either get a surplus or a decrease of transfer margin. This reflects the dependence of the transfer margin on the generation-sharing scenario.

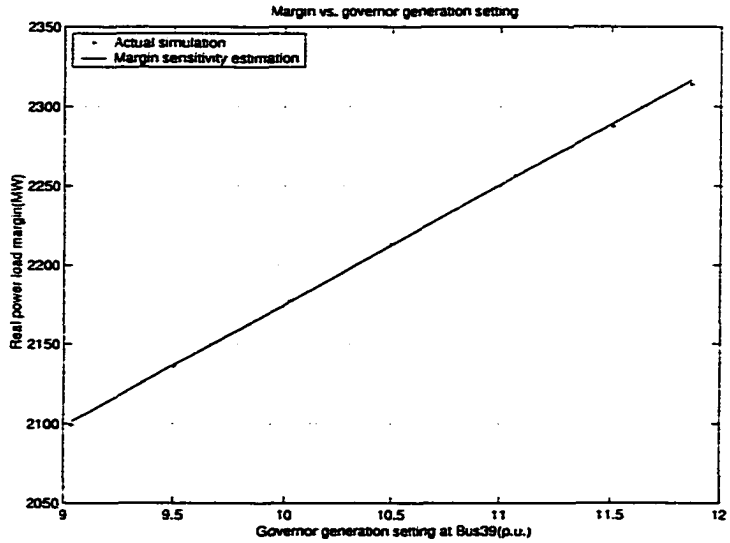

Figure 8.12 Load margin vs. governor generation setting

The AVR reference voltage (Figure 8.13) is one of the control settings to control generator terminal voltages. From Figure 8.13, we can see that V_{ref} is very effective for the increase of the transfer. A 20% increase in $V_{ref,31}$, with the nominal setting at $1.05p.u.$, makes the system able to transfer an approximately additional $548MW$ before the voltage collapse. This increase of the AVR reference voltage results in a little bit high generator terminal voltage ($V_{31} = 1.11p.u.$). If we enforce the terminal voltage limit, the margin change will then be further restricted.

One of the reasons for voltage instability is the lack of reactive power support at some critical locations. Providing enough reactive power (Figure 8.14) locally at or near heavily loaded buses usually

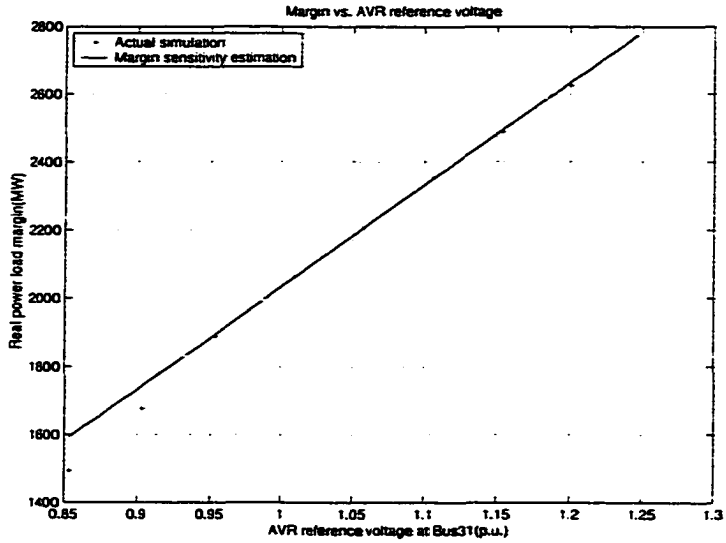

Figure 8.13 Load margin vs. AVR reference voltage

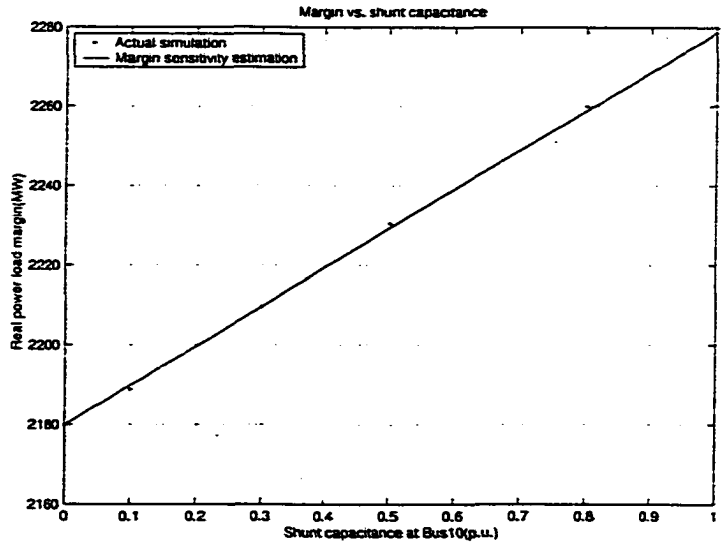

Figure 8.14 Load margin vs. shunt capacitance

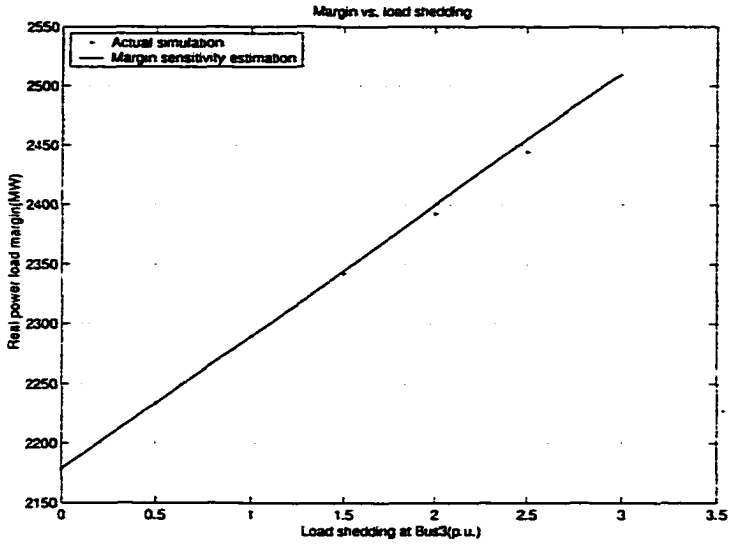

Figure 8.15 Load margin vs. load shedding

increases the real power transfer margin. For the New England system, margin sensitivity calculation shows that Bus10 is one of the best locations to put reactive power support. This bus is linked to G32 which has hit its limit. Quantitatively, it is shown in Figure 8.14 that around $1p.u.$ shunt installation leads to an increase of around $106MW$ in the total real power transfer.

The real and reactive power loads at Bus3 are $322MW$ and $122MVAR$ respectively after the complete restoration. If this load is shed up to $2.0p.u.$ at a constant power factor, the transfer margin will increase almost linearly to about $2386MW$ (Figure 8.15). The linear estimate works quite well for this case.

8.4 CQSS Simulation for Scenario Two

8.4.1 Load Restoration Simulation: α As Continuation Parameter

The contingency considered for Scenario Two is the transmission line outage between Bus8 and Bus9 as well as the loss of part generation of G39 when the system's total load is $7220MW$. The incident has been applied at $t = 0s$. After the contingency, the CQSS simulation is used to trace the system's trajectory while considering both tap dynamics and thermostatic load self-restoration.

This outage leads to the system's voltage collapse due to the singularity-induced bifurcation. At this point, there is no short-term equilibrium. Many generators hit their armature current, field current and

reactive power limits. During the tracing, we also identify the saddle node bifurcation that corresponds to the long-term instability.

For both Scenario One and Scenario Two, trajectory sensitivity could be used to identify the long-term saddle node bifurcation. Continuation parameter could be applied to identify the singularity-induced bifurcation in Scenario Two. We also use continuation parameter to identify the long-term saddle node bifurcation in Scenario One based on some specific assumptions.

Figure 8.16 gives the AVR responses of the generators G30, G32 and G33, under armature current limits. The armature current of G30 hits the limit at $t = 100s$, whereas that of G32 reaches the limit at $t = 120s$. The generator G33 is within the limit.

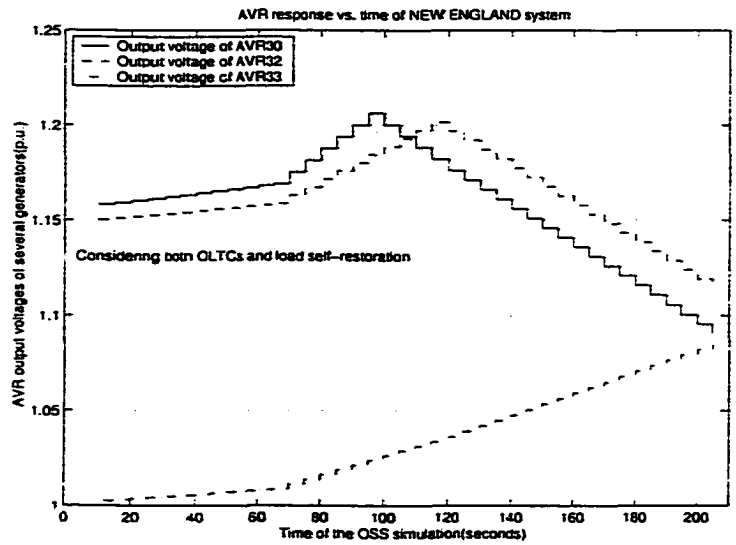

Figure 8.16 AVR responses of G30, G32 and G33 under armature current limits

Figure 8.17 depicts the AVR responses of the generators G31, G35 and G36, while considering their field current limits. Similarly, it shows that the field currents of G31 and G35 reach the limits around $t = 150s$ and that of G36 is within the limit.

Figure 8.18 presents typical OLTC behaviors. Although most taps decrease their ratios towards the lower bounds after the disturbance, the OLTCs can't bring the load-side bus voltages back to the normal values due to the severity of the contingency. Moreover, all the taps have not reached their operating limits at the collapse point.

Figure 8.19 shows the time evolution of three bus voltages on the distribution side of the OLTCs.

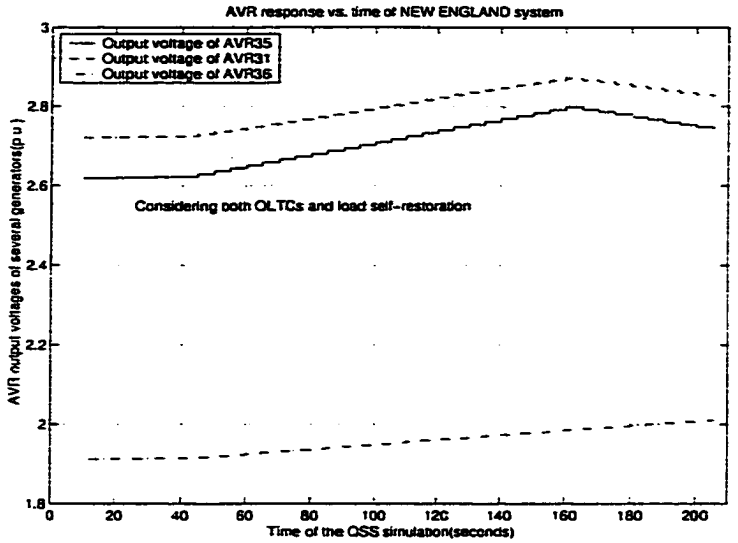

Figure 8.17 AVR responses of G31, G35 and G36 under field current limits

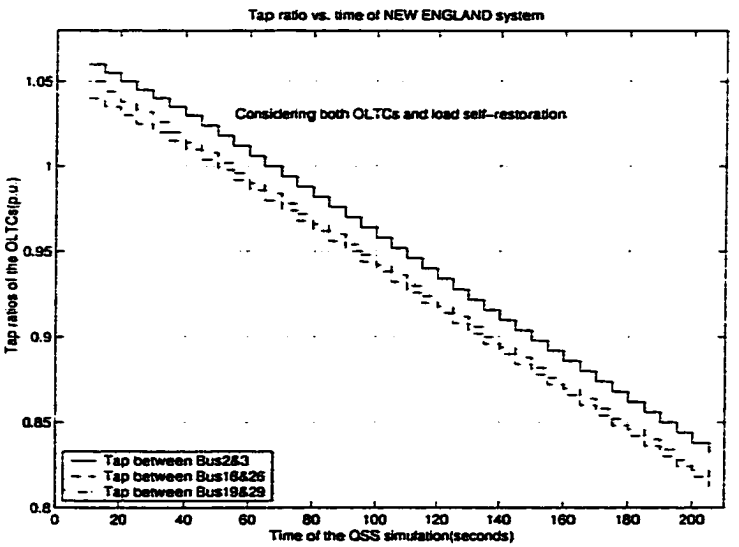

Figure 8.18 Three tap ratios vs. time

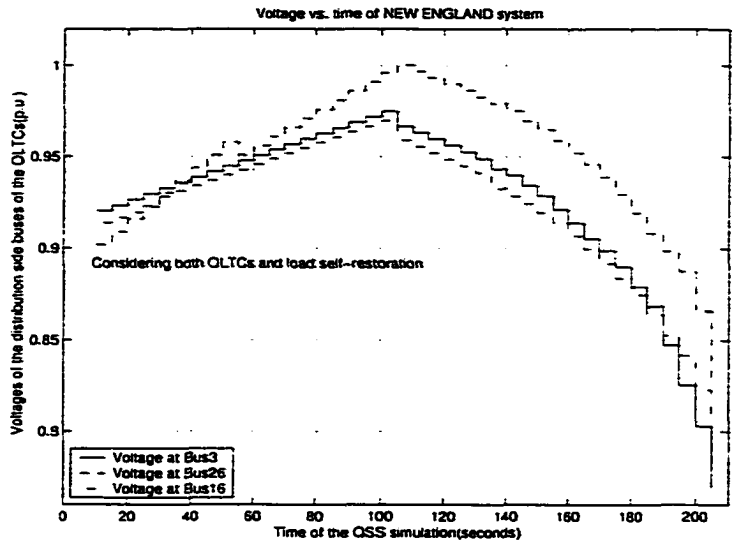

Figure 8.19 Voltage evolution of three buses

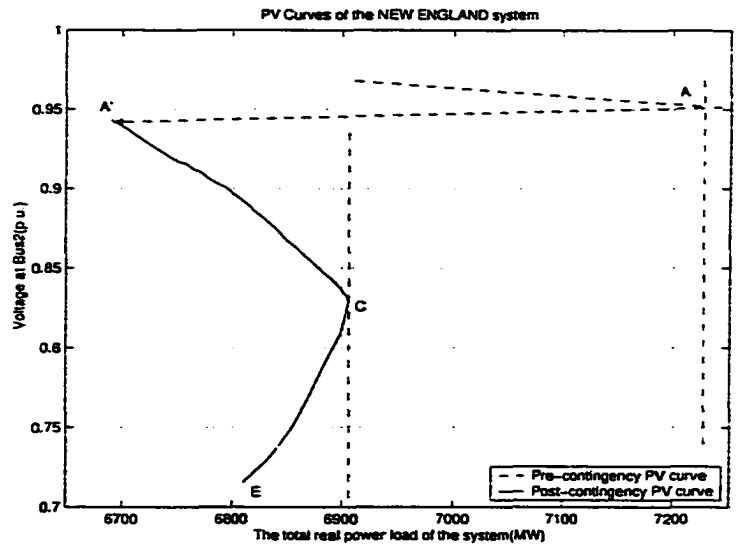

Figure 8.20 PV curves of the New England system

These voltages evolve under the effects of the OLTCs and the thermostatic load restoration. After some generators hit their limits, the OLTCs have no significant influence on the voltages [55].

Figure 8.20 shows the pre-contingency and post-contingency PV curves of the New England system. In the figure, A' is the system's operating point just after the contingency where $P_{A'} = 6690MW$. C and E respectively correspond to the SNB and the SIB in the long-term time scale. The maximum real power load of this system is around $6906MW$. Next, we will use two methods to identify the bifurcations mentioned above.

8.4.2 Identification of the Long-Term Saddle Node Bifurcation

The time evolution of the peak value of the trajectory sensitivity with respect to load shedding is shown in Figure 8.21. The SNB point corresponds to a time instant, where this sensitivity increases dramatically to a very large value. Then a change in sign indicates that the long-term SNB point has been crossed between $t = 150s$ and $t = 170s$. The point at $t = 160s$ is taken as the critical time for the system to reach the long-term SNB point. The result is well confirmed again by the one shown in [38].

8.4.3 Identification of the Singularity-Induced Bifurcation

This bifurcation can be readily identified by the null $d\alpha$. Table 8.3 shows how the continuation parameter α changes in the last five steps and the corresponding time.

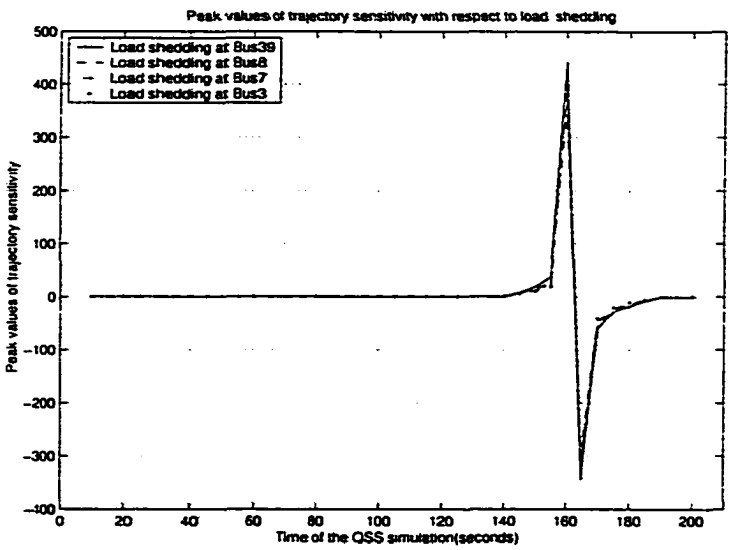

Figure 8.21 Peak values of trajectory sensitivity wrt. P_{l0} vs. time

The corresponding tangent vector obtained in the predictor, shown in Table 8.4, indicates that the instability is associated with a loss of synchronism of the generators. In our DAE formulation, the state variables associated with the short-term components are considered completely. Therefore, combined with $d\alpha$, the tangent vector gives us the stability information of the system's short-term dynamics. Compared to the eigenvalue and eigenvector calculation which sometimes is very expensive, the singularity identification achieved by the continuation parameter and the tangent vector is relatively simple and fast.

In the table, the first four machines are severely demagnetized, as seen from the large negative tangent vector components relative to $E_q^{'}$. This leads to considerable voltage drops at the machine terminals, as well as in the rest of the system, and coincides with the result given in [38].

Table 8.3 $d\alpha$ in the last five steps

Time(s)	160	170	180	190	200
$d\alpha$	-0.03186	-0.03185	-0.03183	-0.03182	0.03062

Table 8.4 Tangent vector when $d\alpha = 0.03062$

Generators	$d\delta$	$d\omega$	$dE_q^{'}$
G30	1.00	-0.06	-0.5983
G32	0.64	-0.05	-0.3869
G31	0.62	-0.05	-0.3837
G35	0.41	-0.04	-0.2356
G33	0.06	-0.00	0.1324
G36	0.00	-0.00	0.0632

8.5 Load Shedding to Restore the Long-Term Voltage Stability

8.5.1 Margin Sensitivity for Load Shedding

Margin sensitivity related to the load shedding is computed at the long-term SNB point of the post-contingency PV curve. Table 8.5 gives the values of margin sensitivity with respect to different load buses. This table shows that load shedding is the most effective at Bus39.

Assuming no limit on the interruptible part, it is sufficient in this example to act on a single load. As in this research we focus on minimal load shedding, it is best to shed load at the single bus which has the largest margin sensitivity. Any shedding at the combination of more buses increases the shedding

Table 8.5 Margin sensitivity wrt. different load-shedding locations

Controls	Margin sensitivity
$P_{l0,39}$	0.147214
$P_{l0,3}$	0.144382
$P_{l0,12}$	0.139294
$P_{l0,7}$	0.125803
$P_{l0,8}$	0.116293
$P_{l0,20}$	0.108976
$P_{l0,4}$	0.102863

amount, since the direction in which we move the unsolvable operating point back to the stability boundary doesn't correspond to the shortest distance. It is quite common to find in practice, however, that shedding the whole load of the bus with the largest margin sensitivity is not enough to restore a long-term equilibrium. Furthermore, only a fraction of each load may be interruptible. The minimal load shedding over several, partly interruptible loads, is directly obtained by treating loads at the decreasing order of their margin sensitivities, shedding at each bus the maximal interruptible part of the load until an equilibrium is recovered. Other criteria to shed loads could be developed in more detail in the future.

8.5.2 Load-Shedding Implementation

We use the load-shedding scheme proposed in Chapter 7 to achieve the stability of the system in Scenario Two in a similar manner as that outlined before. Several aspects of the results are presented and discussed here. The specific steps to obtain these results will not be stated again. By repeating the general load-shedding scheme for various shedding times, we can determine ΔP as a function of the shedding delay t_s. The result is shown in Figure 8.22. Note that the obtained characteristic is close to the one predicted before. Furthermore, when the load-shedding scheme is performed iteratively, there are errors involved since some tolerance is set for stopping the program.

Figure 8.23 shows a sample of curves by applying the above methodology to implement load shedding. They correspond to the shedding at $t = 170s$ of respective $260MW$, $290MW$, $340MW$ and $420MW$ of load at Bus39. The $340MW$ case is marginally stable while $290MW$ is unstable.

In order to have the system stable in the final steady state, it is required to shed $50MW$ more. Figure 8.23 shows that the additional $50MW$ shedding yields a significant increase in the final voltage. The same figure shows that shedding $80MW$ more only brings a marginal increase in voltage. The reason is that after shedding $340MW$, voltages are already well controlled by generators. The effect of

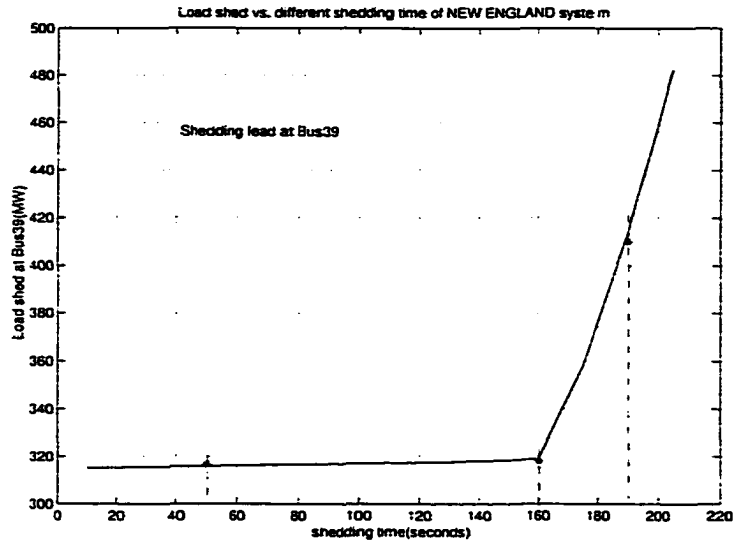

Figure 8.22 ΔP vs. time delay t_s of load shedding at Bus39

the additional $80MW$ shedding is to increase the reactive reserve, not to stabilize voltages.

Figure 8.24 shows the stabilized evolution of the voltage at Bus2 in three load-shedding scenarios taken from the curve of Figure 8.22. When load is shed at $t = 50s$, the voltage settles down at a lower than the pre-shedding voltage. When shedding load at $t = 160s$ or $t = 190s$, the voltage increases up to its final value.

Based on margin sensitivity also, we select four other buses (Bus7, Bus3, Bus8 and Bus20) for load shedding. However, there is not enough to shed the required load at a single bus (Bus3 and Bus7 respectively) to save the system. We have to shed the combination of loads at Bus3 and Bus7 according to the criterion stated in Chapter 8.5.1. Therefore, the load at Bus3 is first shed to zero and Bus7 takes the rest of the required amount. This criterion is really simple and easy to implement. Other optimization methods may be applied to obtain the optimal combination of several buses for load shedding. Figure 8.25 shows the ΔP vs. t_s characteristics relative to these shedding locations. The ranking predicted by margin sensitivity is fully confirmed by the relative position of the curves in Figure 8.25. The curve obtained by shedding loads at Bus3 and Bus7 is still lower than two other curves since margin sensitivities at both buses are larger than those at Bus8 and Bus20.

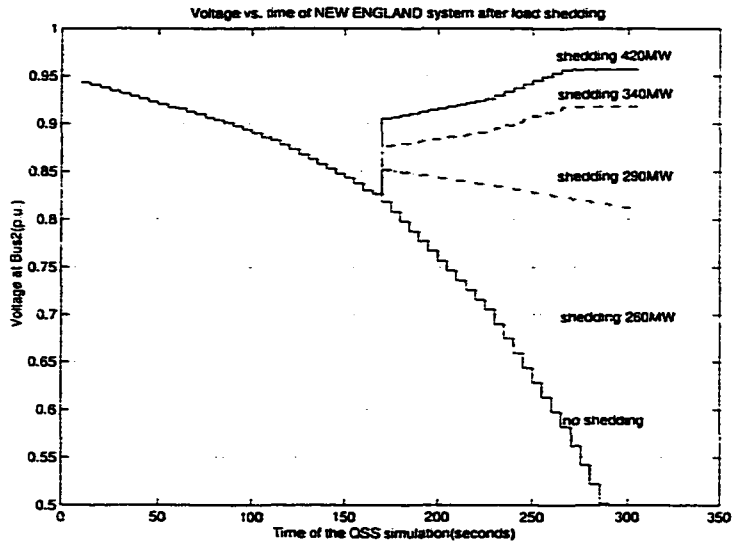

Figure 8.23 Different load shedding at Bus39 at $t = 170s$

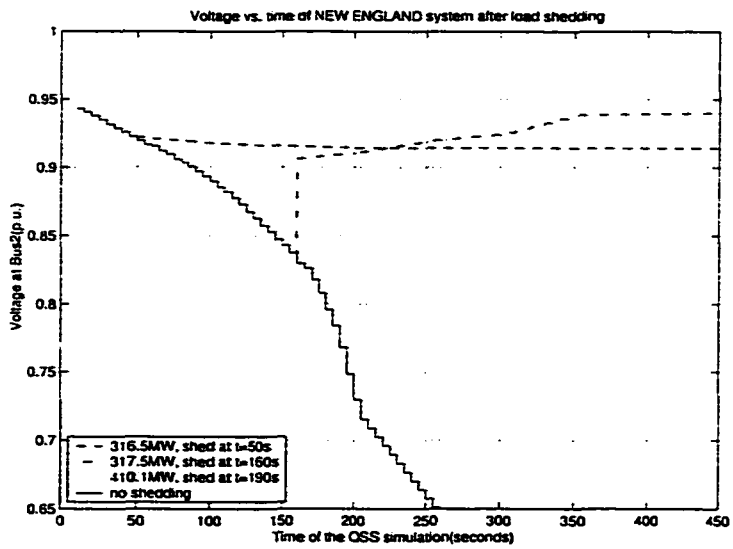

Figure 8.24 Influence of different load-shedding time delays

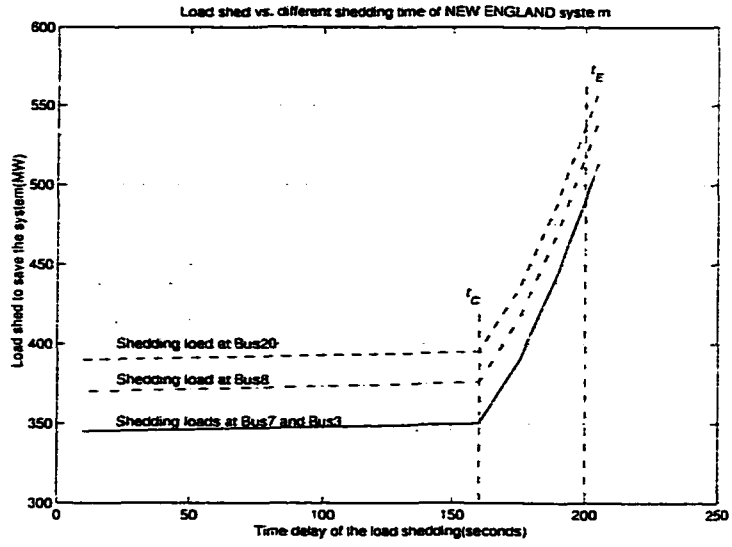

Figure 8.25 Influence of different load-shedding locations

8.6 Control Actions to Increase the Voltage Stability Margin

Among a total of 40 credible contingencies that include all of the single generator and non-radial transmission line outages after the restoration, only five generator contingencies (G31, G32, G33, G35 and G38) lead to the post-contingency voltage stability margin of less than 10%. The outage of the largest generator G39 creates an unsolvable case. To design the control strategy, here, we use the generator G33 contingency that results in the smallest post-contingency voltage stability margin (6.5%).

The objective of the control for G33 contingency is to increase its post-contingency voltage stability margin from 6.5% to the required 10% with the minimum cost. This is a typical case for Scenario One. We have obtained margin sensitivity at the long-term SNB point for all the applicable control variables after the contingency. Table 8.6 lists the control actions of eight different control schemes obtained by our proposed approach for different assumptions of control cost factors.

Scheme1 assumes that all the control actions have the same cost factor. Because AVR reference voltages are much more effective in increasing the stability margin than other control variables, the obtained optimal control strategy mainly involves the changes of the most effective AVR reference voltages ($V_{ref36,32,38,39}$). The Scheme2 gives another control strategy where the control costs for the generation rescheduling is assumed to be the cheapest. Scheme3 and Scheme4 respectively correspond to shedding loads at Bus20 and Bus15, and shedding loads at Bus3, Bus16 and Bus26. In Scheme3,

in order to achieve the specified margin increment of $239.25MW$, the total load of $678.32MW$ should be shed at those two buses. The load curtailment amount is much larger than the amount of actual voltage stability margin increase in both Scheme3 and Scheme4. Scheme5 adds shunt capacitance at Bus20 alone. Scheme6 performs the generator secondary voltage control at G36 and G38 respectively, combining with the additional installation of shunt capacitor at Bus20. Scheme7 implements both the generation rescheduling and the generator secondary voltage control at G35 and G38. Finally, Scheme8 performs the generation rescheduling at G39 with adding shunt capacitance at Bus20. Table 8.7 gives the verified results of these control schemes with the CQSS simulation program. Clearly, all the control schemes have achieved the expected margin increase. Most of them involve two control actions. The iteration number, which corresponds to the number of times when the optimization is performed, is also shown in the table. Again, it confirms us that this sensitivity-based optimization is quite appropriate for designing the control strategy.

After the linear optimization, we can obtain the whole PV curve from the original tracing by applying trajectory sensitivity. Figure 8.26 gives the approximate PV curve without tracing and the actual PV curve by the simulation under the modified control parameters when Scheme1 is chosen as the example. It shows that these two curves are very close.

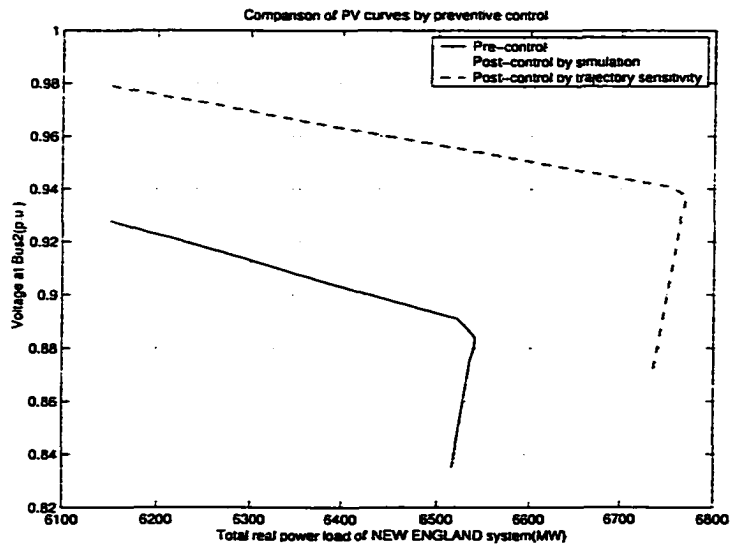

Figure 8.26 PV diagram comparison by tracing and trajectory sensitivity

Table 8.6 Changes of control variables in eight control schemes

Scheme no.	Variables for control	Weight factors	Control amount($p.u.$)
Scheme1	$V_{ref,36}$	1.00	**0.0168**
	$V_{ref,32}$	1.00	**0.0317**
	$V_{ref,38}$	1.00	**0.0604**
	$V_{ref,39}$	1.00	**0.0803**
	others	1.00	0.00
Scheme2	$P_{gs0,39}$	1.00	**0.6502**
	$P_{gs0,31}$	1.00	**−0.6604**
	$P_{gs0,34}$	1.00	**−0.4170**
	others	40.0	0.00
Scheme3	$P_{l0,20}$	1.00	**−3.6398**
	$P_{l0,15}$	1.00	**−3.1634**
	others	40.0	0.00
Scheme4	$P_{l0,3}$	1.00	**−3.0796**
	$P_{l0,16}$	1.00	**−2.4882**
	$P_{l0,26}$	1.00	**−1.2011**
	others	40.0	0.00
Scheme5	$B_{sh,20}$	1.00	**1.1879**
	others	40.0	0.00
Scheme6	$V_{ref,36}$	10.0	**0.0167**
	$V_{ref,38}$	10.0	**0.0608**
	$B_{sh,20}$	1.00	**1.0001**
	others	40.0	0.00
Scheme7	$P_{gs0,35}$	1.00	**0.6972**
	$P_{gs0,38}$	1.00	**−0.4283**
	$V_{ref,35}$	10.0	**0.0173**
	$V_{ref,38}$	10.0	**0.0595**
	others	40.0	0.00
Scheme8	$P_{gs0,39}$	1.00	**0.6583**
	$B_{sh,20}$	1.00	**1.0043**
	others	40.0	0.00

Table 8.7 Voltage stability margin with eight control schemes

Scheme no.	Iterations	Max. total load(MW)	Actual margin(%)	Error(%)
Scheme1	3	6772.9723	10.2853	0.2853
Scheme2	3	6755.2324	9.9964	-0.0036
Scheme3	3	6774.0872	10.3034	0.3034
Scheme4	2	6774.2738	10.3064	0.3064
Scheme5	2	6772.0231	10.2698	0.2698
Scheme6	3	6782.9783	10.4482	0.4482
Scheme7	2	6786.8232	10.5108	0.5108
Scheme8	1	6780.6789	10.4107	0.4107

8.7 Effects of Controls

In this research, a total of four controls are applied, which are generator governor setting (P_{gs0}), AVR reference voltage (V_{ref}), shunt capacitor (B_{sh}) and load shedding (P_{l0}). When the control schemes to increase the stability margin are implemented on the test systems, all the buses which have the necessary equipment for the controls can be considered as the control locations. For example, all the generator buses are eligible for generation rescheduling and secondary voltage control. All the load buses are the candidate buses for load shedding. Each bus in the system can be installed with the shunt capacitor. The formulation proposed in Chapter 7 can handle all the possible combinations for different selections of control locations. However, if we include all the buses in the problem formulation, solving this optimization problem may be very time-consuming. Though the better solution is found, the computational cost is increased significantly. In order to obtain a good compromise between accuracy and efficiency, margin sensitivity is used to choose most effective locations for implementing controls. The controls based on the sensitivity information are dominating in increasing the system's stability margin.

For the New England system, there are total 10 P_{gs0}'s and V_{ref}'s, 18 P_{l0}'s and 2 B_{sh}'s. This includes all the generators for P_{gs0} and V_{ref}, and all the load buses for P_{l0}. However, we didn't consider all the buses for shunt compensation (B_{sh}). Only the existing shunt compensators in the system are selected for the control. This is due to the limited available information of shunt capacitors in this system. In fact, we calculate margin sensitivity with respect to any installed compensator and select the location with the largest margin sensitivity to formulate the optimization problem. The aim of this control is to obtain the best control amount of the existing controls in the test system. However, as emphasized before, the designed control strategy can deal with all the control combinations, including the case

where all the buses are considered for implementing the controls.

In general, shunt compensation (B_{sh}) is more effective on improving the voltage stability margin than secondary voltage control (V_{ref}). However, here, AVR reference voltage control achieves a larger margin. The reason may be that there are only two locations for B_{sh}. The influence of shunt compensation is not as significant as expected in this system.

8.8 Concluding Remarks

In this chapter, the overall method proposed to mitigate the long-term voltage instability is tested on the New England 39-bus system. This approach includes the CQSS simulation for Scenario One and Scenario Two respectively. In each scenario, the identification of the SNB and/or SIB could be achieved by trajectory sensitivity and continuation parameter. Furthermore, load shedding to restore the long-term voltage instability and control actions to increase the margin, are implemented. The simulation results of the New England 39-bus confirm the conclusions from the analysis in the previous chapters. Chapter 9 will give the conclusion of this research and some suggestions for future work.

9 . CONCLUSIONS

In this thesis, we developed a novel continuation-based Quasi-Steady-State analysis approach to mitigate long-term voltage instability. The significance of this work is that it develops a comprehensive and efficient set of tools for the long-term voltage instability analysis and control by integrating QSS simulation, continuation method, load restoration and trajectory sensitivity. This comprehensive tool provides all relevant information needed to study long-term voltage instability phenomena.

The results of this research, including theory, analysis, data and observations, lead to the following conclusions:

- Development of the numerically well-conditioned CQSS simulation which takes into account the following factors:
  - The ill-condition of the Jacobian matrix near the bifurcation point that could be avoided by the appropriate selection of continuation parameter;
  - Combined effects of the OLTC and the load change on voltage stability;
  - Dependency of the load change on time.
- Implementation of load restoration through the parameterization of the load exponent which includes the following features:
  - The singularity-induced bifurcation, which can't be clearly identified by the original QSS simulation, is easily detected by the change of the load exponent;
  - The load exponent is solved from the differential equation representation of generic load restoration.
- Efficient calculation of trajectory sensitivity which provides:
  - Fast methods to calculate trajectory sensitivity at each equilibrium;
  - Identification of the long-term SNB point;

  - Margin sensitivity at the long-term SNB point by introducing continuation parameter;
  - State variable sensitivity and margin estimation for designing the control to maintain a sufficient stability margin.

- Implementation of the control actions to increase the system's stability margin which provides:
  - The controls for the specific margin requirement as well as satisfying the constraints on the other state variables;
  - The whole PV curve after optimization by directly applying trajectory sensitivity (without any re-tracing).

- Implementation of the load shedding to restore the system's solvability which provides:
  - The most appropriate time to take control actions;
  - The most effective locations to implement controls;
  - The amount of successful load shedding.

A systematic analysis tool is developed in this research, which includes the following three major contributions with respect to the existing research:

- Compared to the original QSS analysis, the CQSS simulation is more well-conditioned and fast by introducing continuation method. QSS analysis is much faster than the time-domain method by assuming the fast dynamics of the system have reached their equilibrium conditions. The speed of CQSS is further improved by replacing the differential equation with its analytical solution in the simulation.

- The control problem proposed in this research improves the voltage stability margin. In essence, it is a stability-constrained optimization problem. Unlike the previous research, here, voltage stability margin is explicitly represented as a constraint.

- The load-shedding scheme presented in this research expands the undervoltage load-shedding strategy proposed by D. J. Hill. The CQSS-based load shedding achieves the minimum load shedding by incorporating the timing and location issues, whereas only the amount aspect is considered in his research. The load-shedding scheme mainly takes into account the voltage constraints and is not optimized. Compared to V. Cutsem's binary search scheme, our method considers the short-term load characteristic explicitly and provides more accurate information of the system.

The following recommendations are made for future work based on the experience of this research work:

- The incorporation of other elements closely related to voltage stability phenomena. (Here, CQSS simulation only takes into account taps and thermostatic loads in the long-term time scale without considering other devices in this time scale.)
- The use of more advanced optimization algorithms to implement other fast control measures. (Here, only load shedding is considered for corrective control.)
- The design of more sophisticated criteria to consider better combinations and implementation steps for load shedding. (These criteria, integrated with other techniques in the power system such as SCADA, may be further developed as a good online tool for voltage stability analysis in Scenario Two.)
- The development of more efficient techniques for the large scale system calculation.

APPENDIX A SADDLE NODE BIFURCATION POINT DETERMINATION

For the general power system model below:

$$\dot{z} = h(x, y, z, \mu) \tag{A.1}$$

$$\dot{x} = f(x, y, z, \mu) \tag{A.2}$$

$$0 = g(x, y, z, \mu) \tag{A.3}$$

where z is a vector of continuous and discrete long-term state variables. x is a vector of transient state variables. y is a vector of algebraic variables and μ is a vector of system parameters.

While tracing the equilibrium path, the saddle-node bifurcation point is determined by well-known eigenproperties described as follows.

Linearizing (A.1-A.3), we can get:

$$\begin{bmatrix} \Delta\dot{z} \\ \Delta\dot{x} \\ 0 \end{bmatrix} = \underbrace{\begin{bmatrix} h_z & h_x & h_y \\ f_z & f_x & f_y \\ g_z & g_x & g_y \end{bmatrix}}_{J_{total}} \begin{bmatrix} \Delta z \\ \Delta x \\ \Delta y \end{bmatrix} \tag{A.4}$$

It should be noticed that since the time scales have been divided to short term and long term. both h_x and f_z will be equal to zero. Then the stability of the entire system is decided by considering the eigenvalues of the following equation:

$$\begin{bmatrix} \Delta\dot{z} \\ \Delta\dot{x} \end{bmatrix} = \underbrace{\left[\begin{bmatrix} h_z & h_x \\ f_z & f_x \end{bmatrix} - \begin{bmatrix} h_y \\ f_y \end{bmatrix} [g_y]^{-1} \begin{bmatrix} g_z & g_x \end{bmatrix}\right]}_{A_{sys}} \begin{bmatrix} \Delta z \\ \Delta x \end{bmatrix} \tag{A.5}$$

At a SNB point. a real eigenvalue of the reduced system matrix becomes zero and A_{sys} becomes singular. It is obvious that determinants of both A_{sys} and J_{total} matrices become singular at a SNB point as shown below:

$$Det[J_{total}] = Det[A_{sys}] = 0 \quad \text{if} \quad Det[g_y] \neq 0 \tag{A.6}$$

In this research, the singularity of J_{total} is detected to determine the saddle node bifurcation. Interestingly, when J_{total} becomes singular, an element of tangent vector at predictor step becomes zero and changes sign. For rough approximation, the tangent vector at predictor step can be assumed to be the left eigenvector v_i^T of A_{sys}.

When the system experiences instability, it is caused by the singularity of short-term or long-term dynamics. It will be shown that the singularity of short-term or long-term dynamics coincides with the singularity of the entire system equations.

A.1 Saddle Node Bifurcation of Long-Term Dynamics

If short-term dynamics are neglected and only long-term dynamics are considered, then:

$$\begin{bmatrix} \Delta \dot{z} \\ 0 \\ 0 \end{bmatrix} = \underbrace{\begin{bmatrix} h_z & 0 & h_y \\ 0 & f_x & f_y \\ g_z & g_x & g_y \end{bmatrix}}_{J_{total}} \begin{bmatrix} \Delta z \\ \Delta x \\ \Delta y \end{bmatrix} \tag{A.7}$$

Then the stability of long-term dynamics is determined by considering the eigenproperties of the following equation:

$$[\Delta \dot{z}] = \underbrace{\left[h_z - \begin{bmatrix} 0 & h_y \end{bmatrix} \begin{bmatrix} f_x & f_y \\ g_x & g_y \end{bmatrix}^{-1} \begin{bmatrix} 0 \\ g_z \end{bmatrix} \right]}_{A_{lt}} [\Delta z] \tag{A.8}$$

Then the system matrix of long-term dynamics A_{lt} and the total Jacobian J_{total} have the following relationship by using the partitioned matrix formula.

$$Det[J_{total}] = Det \underbrace{\begin{bmatrix} f_x & f_y \\ g_x & g_y \end{bmatrix}}_{J_{xy}} Det \underbrace{\left[h_z - \begin{bmatrix} 0 & h_y \end{bmatrix} \begin{bmatrix} f_x & f_y \\ g_x & g_y \end{bmatrix}^{-1} \begin{bmatrix} 0 \\ g_z \end{bmatrix} \right]}_{A_{lt}} \tag{A.9}$$

from which we conclude that, when g_y and J_{xy} are nonsingular, a SNB of long-term dynamics can lead to a SNB of the total coupled system.

A.2 Saddle Node Bifurcation of Short-Term Dynamics

If long-term dynamics are not considered and only short-term dynamics are taken into account, then:

$$\begin{bmatrix} 0 \\ \Delta\dot{x} \\ 0 \end{bmatrix} = \underbrace{\begin{bmatrix} h_z & 0 & h_y \\ 0 & f_x & f_y \\ g_z & g_x & g_y \end{bmatrix}}_{J_{total}} \begin{bmatrix} \Delta z \\ \Delta x \\ \Delta y \end{bmatrix} \tag{A.10}$$

Then the stability of short-term dynamics is determined by considering the eigenproperties of the following equations.

$$[\Delta\dot{x}] = \underbrace{\left[f_x - \begin{bmatrix} 0 & f_y \end{bmatrix} \begin{bmatrix} h_z & h_y \\ g_z & g_y \end{bmatrix}^{-1} \begin{bmatrix} 0 \\ g_x \end{bmatrix} \right]}_{A_{st}} [\Delta x] \tag{A.11}$$

Then the system matrix of short-term dynamics A_{st} and the total Jacobian J_{total} have the following relationship by re-using the partitioned matrix formula.

$$Det[J_{total}] = Det \underbrace{\begin{bmatrix} h_z & h_y \\ g_z & g_y \end{bmatrix}}_{J_{zy}} Det \underbrace{\left[f_x - \begin{bmatrix} 0 & f_y \end{bmatrix} \begin{bmatrix} h_z & h_y \\ g_z & g_y \end{bmatrix}^{-1} \begin{bmatrix} 0 \\ g_x \end{bmatrix} \right]}_{A_{st}} \tag{A.12}$$

from which we conclude that, when g_y and J_{zy} are nonsingular, a SNB of short-term dynamics leads to a SNB of the total coupled system.

A_{st} can be further reduced to (A.13) with the assumption that the long-term dynamics are considered as practically constant during the transient period.

$$A_{st} = f_x - f_y g_y^{-1} g_x \tag{A.13}$$

A.3 Singularity-Induced Bifurcation of Long-Term Dynamics

This singularity occurs at a point of the system's trajectory where the algebraic equation Jacobian is singular. The system model "breaks down", preventing simulation being continued. Singularity-induced bifurcation [11] corresponds to a condition where a curve of equilibrium points crosses the algebraic singularity surface. Passing through a SIB point, the linearized system matrix has an infinite eigenvalue.

From the expression of A_{lt}, we find that a singularity of long-term dynamics corresponds to a singular J_{xy}. Using matrix partitioning once more, we have:

$$Det[J_{xy}] = Det[g_y] Det[A_{st}] \tag{A.14}$$

for a nonsingular g_y. According to (A.14), we can conclude that a singularity of long-term dynamics corresponds to a saddle node bifurcation of short-term dynamics.

From the above discussion, it is obvious that determining saddle node bifurcation point of the total system is necessary and sufficient to identify overall system stability governed by short-term and long-term dynamics.

APPENDIX B SENSITIVITY $\partial Q_G/\partial Q^0$ DERIVATION

Sensitivity $\partial Q_G/\partial Q^0$ represents the sensitivity of the total reactive power generation Q_G with respect to Q^0, where

$$\frac{\partial Q_G}{\partial Q^0} = \left[\begin{array}{ccc} \frac{\partial Q_G}{\partial Q^0_1} & \cdots & \frac{\partial Q_G}{\partial Q^0_{m+n}} \end{array} \right] \tag{B.1}$$

where Q_G is total power generation:

$$Q_G = \sum_{i=m+1}^{m+n} \sum_{j=1}^{m+n} V_i V_j [G_{ij} \sin\theta_{ij} - B_{ij} \cos\theta_{ij}] \tag{B.2}$$

and Q^0 is the coefficient of reactive load model at i-th bus.

$$\underbrace{Q_i^0 (\frac{V_i}{V_0})^{\beta_i}}_{\text{load behavior}} - Q_{inj_i} = 0 \tag{B.3}$$

B.1 Derivation of $\partial Q_G/\partial Q^0$

With the system DAE formulation shown as below:

$$\dot{z} = h(x, y, z, \mu) \tag{B.4}$$

$$\dot{x} = f(x, y, z, \mu) \tag{B.5}$$

$$0 = g(x, y, z, \mu) \tag{B.6}$$

where z is a vector of continuous and discrete long-term state variables, x is a vector of transient state variables and y is a vector of algebraic variables, and μ is a vector of parameters. Rewrite the entire DAEs in compact form at a particular equilibrium point:

$$P(X, Q^0) = 0 \tag{B.7}$$

where $P = (h, f, g)^T$ and $X = (x, y, z)^T$.

Take partial differentiation of both sides of (B.7).

$$\left[\frac{\partial P}{\partial X}\right] \left[\frac{\partial X}{\partial Q^0}\right] + \left[\frac{\partial P}{\partial Q^0}\right] = 0 \tag{B.8}$$

Then,

$$\left[\frac{\partial X}{\partial Q^0}\right] = -\left[\frac{\partial P}{\partial X}\right]^{-1}\left[\frac{\partial P}{\partial Q^0}\right] \tag{B.9}$$

The sensitivity $\partial Q_G/\partial Q^0$ can be represented using chain rule as follows:

$$\left[\frac{\partial Q_G}{\partial Q^0}\right] = \left[\frac{\partial Q_G}{\partial X}\right]\left[\frac{\partial X}{\partial Q^0}\right] = -\left[\frac{\partial Q_G}{\partial X}\right]\left[\frac{\partial P}{\partial X}\right]^{-1}\left[\frac{\partial P}{\partial Q^0}\right] \tag{B.10}$$

Equation (B.10) is similar to Van Custem's security index derivation [28], which is transpose of (B.10). We can see:

$$\left[\frac{\partial Q_G}{\partial Q^0}\right]^T = -\left[\frac{\partial Q_G}{\partial X}\right]^T\left[\left[\frac{\partial P}{\partial X}\right]^T\right]^{-1}\left[\frac{\partial P}{\partial Q^0}\right]^T \tag{B.11}$$

$$= -\begin{bmatrix} 0 & 0 & \frac{\partial q_T}{\partial Q^0} \end{bmatrix}[J^T]^{-1}\begin{bmatrix} 0 \\ 0 \\ \frac{\partial Q_G}{\partial y} \end{bmatrix} \tag{B.12}$$

$$\approx -\frac{\alpha_c}{\lambda_c}\begin{bmatrix} 0 & 0 & \frac{\partial q_T}{\partial Q^0} \end{bmatrix} W_c$$

Stability is determined from the sensitivity as follows:

$\frac{\partial Q_G}{\partial Q^0} > 0$ indicates stable condition;

$\frac{\partial Q_G}{\partial Q^0} < 0$ indicates unstable condition.

B.2 Practical Meaning of Sensitivity $\partial Q_G/\partial Q^0$

This sensitivity indicates that if $\partial Q_G/\partial Q^0$ is infinite for a specific bus i, a tentative increase dQ_i^0 will be unsuccessful, because it would exceed the generation capabilities and cause voltage collapse. Reciprocally, if at each bus, $\partial Q_G/\partial Q^0$ is positively finite, first it implies there exists at least one generated reactive source available and there is no voltage-collapse. Actually, it has been defined in [76] and used in [77].

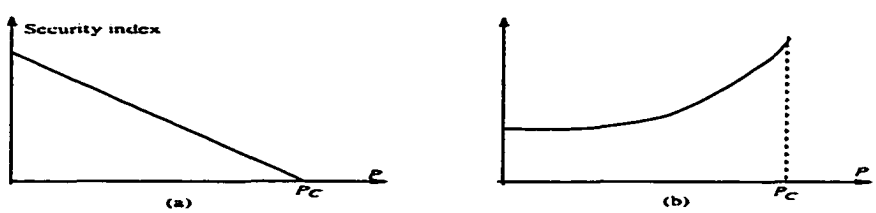

Figure B.1 Illustration of a secure index and an insecure index

It should be noted that Van Custem's sensitivity is not a secure index. The sensitivity is used to diagnose saddle node bifurcation. The secure index should be proportional to load change to provide the margin to instability boundary as shown in Figure B.1(a). However, Van Custem's sensitivity is quite insensitive during normal state and exponentially increase near the instability boundary as shown in Figure B.1(b).

APPENDIX C ISPS AND MARGIN SENSITIVITY FOR LONG-TERM EQUILIBRIUM

ISPS combines the stability and sensitivity information to know the factors that contribute to instability. In small-disturbance analysis, each eigenvalue belongs to a particular eigenbasis. If a critical eigenbasis refers to a critical eigenvalue, then according to the invariance property of the eigenbasis, the system's instabilities are governed by the dynamics on the critical eigenbasis.

Based on the general power system model:

$$\dot{z} = h(x, y, z, \mu) \tag{C.1}$$

$$\dot{x} = f(x, y, z, \mu) \tag{C.2}$$

$$0 = g(x, y, z, \mu) \tag{C.3}$$

where z is a vector of long-term state variables, x is a vector of transient state variables, y is vector of algebraic variables and μ is a vector of system parameters.

For a given state of equilibrium, the sensitivity of the state variable with respect to the parameter can be derived by taking the partial derivative of $f = 0$ and $g = 0$ and $h = 0$, i.e.,

$$\begin{bmatrix} \frac{\partial z}{\partial \mu} \\ \frac{\partial x}{\partial \mu} \end{bmatrix} = A_{sys}^{-1} S \tag{C.4}$$

$$\frac{\partial y}{\partial \mu} = \left[\frac{\partial g}{\partial y}\right]^{-1} \left[-\frac{\partial g}{\partial \mu}\right] - \begin{bmatrix} \frac{\partial g}{\partial z} & \frac{\partial g}{\partial x} \end{bmatrix} \begin{bmatrix} \frac{\partial z}{\partial \mu} \\ \frac{\partial x}{\partial \mu} \end{bmatrix} \tag{C.5}$$

where

$$S = \begin{bmatrix} \frac{\partial h}{\partial y}(\frac{\partial g}{\partial y})^{-1}\frac{\partial g}{\partial \mu} - \frac{\partial h}{\partial \mu} \\ \frac{\partial f}{\partial y}(\frac{\partial g}{\partial y})^{-1}\frac{\partial g}{\partial \mu} - \frac{\partial f}{\partial \mu} \end{bmatrix} \tag{C.6}$$

Then the link between the eigenvalues and the parameters is achieved by ISPS whose measure is defined as:

$$\sigma_p = v_i^T S = -\begin{bmatrix} v_h^T & v_f^T & v_g^T \end{bmatrix} \begin{bmatrix} h_\mu \\ f_\mu \\ g_\mu \end{bmatrix} \tag{C.7}$$

where v_i is left eigenvector of A_{sys}(Appendix A) and

$$\begin{bmatrix} v_h^T & v_f^T & v_g^T \end{bmatrix} J_{total} = \begin{bmatrix} \lambda_i v_h^T & \lambda_i v_f^T & 0 \end{bmatrix} \tag{C.8}$$

which leads to:

$$v_g^T = -\begin{bmatrix} v_h^T & v_f^T \end{bmatrix} \begin{bmatrix} h_y \\ f_y \end{bmatrix} g_y^{-1} \tag{C.9}$$

$$\begin{bmatrix} v_h^T & v_f^T \end{bmatrix} \left(\begin{bmatrix} h_z & 0 \\ 0 & f_x \end{bmatrix} - \begin{bmatrix} h_y \\ f_y \end{bmatrix} g_y^{-1} \begin{bmatrix} g_z & g_x \end{bmatrix} \right) = \lambda_i \begin{bmatrix} v_h^T & v_f^T \end{bmatrix} \tag{C.10}$$

where the definition of J_{total} can be found in Appendix A. From (C.10), we know that $[v_h^T \quad v_f^T]$ is the left eigenvector of A_{sys} corresponding to eigenvalue λ_i.

A normal vector to the feasible set at $\mathbf{S}^*$ is [78]:

$$\mathbf{n}(\mathbf{S}^*) = \zeta J_\mu \,. \tag{C.11}$$

where ζ is the left eigenvector corresponding to the trivial eigenvalue of J_{total} and J_μ is the Jacobian of h, f and g with respect to the parameter μ. This normal vector is perpendicular to the tangent plane. In addition, it is noticed that at this bifurcation point, $[v_h^T \quad v_f^T \quad v_g^T]$, computed from (C.8) for the zero eigenvalue of A_{sys}, is nothing but ζ in (C.11). Thus the normal vector can be written as:

$$\mathbf{n}(\mathbf{S}^*) = \begin{bmatrix} v_h^T & v_f^T & v_g^T \end{bmatrix} \begin{bmatrix} h_\mu \\ f_\mu \\ g_\mu \end{bmatrix} \tag{C.12}$$

The normal vector defined above is the negative of σ_p vector corresponding to the zero eigenvalue of A_{sys} at saddle node bifurcation. Then we can say that σ_p gives complete information about the parameter influence on the eigensubspace as well as provides the cluster of parameters that are most sensitive to the corresponding eigenvalues.

Furthermore margin sensitivity proposed in [15] and [67] can be further expanded as:

$$\frac{\partial \lambda}{\partial \mu} = -\frac{\begin{bmatrix} v_h^T & v_f^T & v_g^T \end{bmatrix} \begin{bmatrix} h_\mu \\ f_\mu \\ g_\mu \end{bmatrix}}{\begin{bmatrix} v_h^T & v_f^T & v_g^T \end{bmatrix} \begin{bmatrix} h_\lambda \\ f_\lambda \\ g_\lambda \end{bmatrix}} \tag{C.13}$$

Note here λ denotes continuation parameter, not the eigenvalue of A_{sys}.

APPENDIX D CLASSIFICATION OF INSTABILITY MECHANISMS

The major instability mechanisms according to different time scales are described in detail in [5] and described briefly as follows.

D.1 Short-Term Voltage Instability

In the short-term period immediately following a severe contingency, the slow, long-term variables z do not respond yet and can be considered constant, resulting in the approximate short-term subsystem whose dynamics of the voltage stability should be analyzed firstly. In the case of short-term voltage stability, the driving force of instability is the tendency of dynamic loads to restore. There are two major instability mechanisms relating to this subsystem:

- ST1: Loss of post-contingency equilibrium of short-term dynamics;
- ST2: Lack of attraction towards the stable post-contingency equilibrium of short-term dynamics;

A typical case of ST1 voltage instability is the stalling of induction motors after a disturbance increasing the total transmission impedance. Due to the increased impedance, the motor mechanical and electrical torque curves may not intersect after the disturbance, leaving the system without post-contingency equilibrium. As a result the network collapses.

ST2 voltage instability is the stalling of induction motors after a short-circuit. For heavily loaded motors and/or slowly cleared fault conditions, motors can not re-accelerate after the fault is cleared. The motor mechanical and electrical torque curves intersect in this case, but at fault clearing the motor slip exceeds the unstable equilibrium value.

D.2 Long-Term Voltage Instability

Here we assume that the short-term dynamics respond in a stable manner to the changes of z. Similar to short-term dynamics, long-term dynamics may become unstable in the following ways:

- LT1: Loss of equilibrium of long-term dynamics:
- LT2: Lack of attraction towards the stable long-term equilibrium:

LT1 is the most typical instability mechanism, with the loads trying either to recover their post-contingency powers through OLTC actions or to reach their long-term characteristics through self-restoration.

A typical example of LT2 instability would be an LT1 scenario followed by a delayed corrective control which restores a stable equilibrium but not soon enough for the system to be attracted by the stable post-contingency equilibrium.

D.3 Short-Term Instability Induced by Long-Term Dynamics

Usually, the long-term instability leads to a short-term instability. We can distinguish again two major types of instability:

- S-LT1: Loss of short-term equilibrium caused by long-term dynamics:
- S-LT2: Lack of attraction of the stable short-term equilibrium due to shrinking region of attraction caused by long-term dynamics:

A typical case of S-LT1 instability is when the system's degradation caused by long-term instability LT1 or LT2 results in either loss of synchronism of field current limited generators or induction motors stalling.

In practice, an S-LT2 instability will be encountered before reaching the actual saddle node of short-term dynamics, due to the shrinking region of attraction of the stable equilibrium point as it is approached by the unstable one.

APPENDIX E LOAD CHARACTERISTICS AND REGION OF ATTRACTION

E.1 System and Load Model

The power system model is shown in Figure E.1 [47]. A single generator is supplying a load over a transmission line. For simplicity, all resistances and line chargings have been neglected.

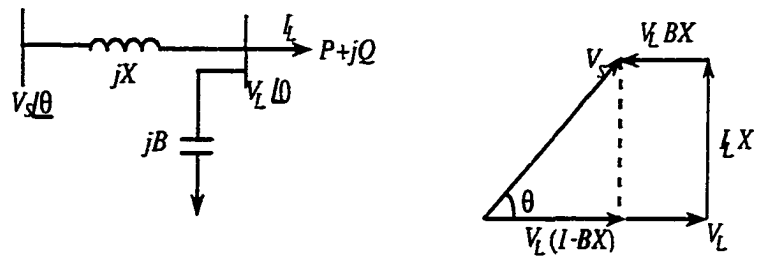

Figure E.1 A power system with constant source voltage

In voltage stability analysis, load dynamics play a very important role. When there is a sudden change in the system's voltage such as following a disturbance, the load will change momentarily. It will then adjust the current(or impedance) and draw whatever current from the system is necessary in order to satisfy the demand. The process is not instantaneous. Assuming a unity power factor load, the load dynamics may be represented by:

$$T_L \frac{dG}{dt} = P_0 - V_L^2 G \tag{E.1}$$

where V_L is the load voltage, P_0 is the power set point, G is the load conductance which is adjusted to maintain constant power, T_L is the load time constant. G depends on several factors (T_L, P_0, V_L and

t). Any change of them could affect the short-term load characteristic, such as load shedding (P_0 is changed). This model is used to provide insights and explain the various phenomena in voltage stability.

E.2 Region of Attraction

First we will examine the region of attraction of the stable equilibrium point in the context of the system's PV curve. Consider the simplified system with constant sending-end voltage shown in Figure E.1. The PV curve of the post-disturbance system is shown in Figure E.2. For a constant power load P_0, the load characteristic, as shown by the vertical line, would intersect the system's PV curve at two points, A and B, corresponding to the two possible equilibrium points. Point A, on the upper portion of the PV curve (the high voltage solution), is a stable equilibrium point, whereas point B, on the lower portion of the PV curve (the low voltage solution), is an unstable equilibrium point. This may be verified by linearizing (E.1) around these equilibrium points and applying the condition for stability.

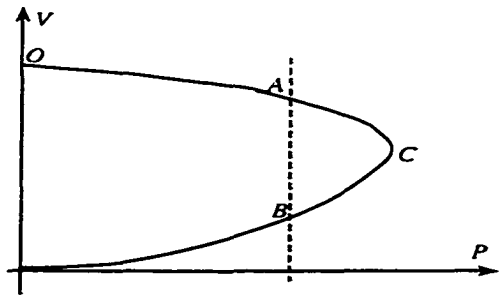

Figure E.2 PV curve of the small model system

It will be shown that if the state reached at the end of the disturbance lies anywhere on the portion of $O-A-C-B$ of the PV curve, the post-disturbance system will be stable, i.e., the operating point will settle at the stable equilibrium point A. The region $O-A-C-B$, i.e., the region of the PV curve to the right of the unstable equilibrium point is the region of attraction of the stable equilibrium point of the post-disturbance system. Because of the load dynamics, which change continuously with respect to time if no equilibrium is reached, C can not be interpreted as a separation point of the stable or unstable situation of the system.

From Figure E.1,

$$V_L^2 = \frac{V_s^2}{(1-BX)^2 + G^2X^2} \tag{E.2}$$

Therefore, (E.1) can be expressed as:

$$T_L \frac{dG}{dt} = \frac{P_0 X^2 (G - G_{10})(G - G_{20})}{(1 - BX)^2 + G^2 X^2} \tag{E.3}$$

where

$$G_{10,20} = \frac{V_s^2 \pm \sqrt{V_s^4 - 4P_0^2 X^2 (1 - BX)^2}}{2P_0 X^2} \tag{E.4}$$

The two values of G correspond to the two voltage solutions for the given power P_0. In Figure E.2, these two solutions correspond to the equilibrium points A and B respectively. The higher value of G corresponds to the low voltage solution, and vice versa. This is verified by:

$$V_{L1}^2 G_{20} = V_{L2}^2 G_{10} = P_0 \tag{E.5}$$

Equation (E.3) shows that if the initial state is to the left of the point A on the PV curve(G less than G_{20}), dG/dt is positive, and therefore, the operating point will move to A, where $dG/dt = 0$. Similarly, if the initial state is anywhere on the portion of $A - C - B(G_{20} < G < G_{10})$, dG/dt is negative and, therefore, the operating point moves to A. If the initial state is to the left of B, dG/dt is positive and the operating point moves further away from B. The region of the right of B is the region of attraction of the stable equilibrium point A.

A physical explanation can be provided as follows: Consider an initial state in the lower region of the PV curve but to the right of the unstable equilibrium point B. Since in this state the power delivered by the network is greater than the set-point power, P_0, the constant power control mechanism would decrease the current or admittance in order to bring the power down. However, this will increase the power still further, since the voltage will increase at a faster rate with the decrease in current or admittance in this region. The operating point will, therefore, move up the PV curve until point C is reached. From this point upwards the same control command will however, decrease the power. The process will continue until the stable equilibrium point A is reached. Using the same argument, it can be seen that starting from anywhere on the upper portion of the PV curve, the operating point will move to the stable equilibrium point A.

E.3 Load Restoration Classification

The exponential load model is given as follows:

$$P_l = P_{l0} \left(\frac{V_2}{V_{20}} \right)^{\alpha} \tag{E.6}$$

where V_2 is the secondary voltage of the OLTC.

There are two ways to accomplish the load restoration:

- Through OLTC: when the OLTC succeeds to restore V_2 close to its reference value, the load power is also restored. It is indirect. In Figure E.3, the tap ratio r changes continuously, which shows up as different short-term load characteristic curves. After the load restoration is accomplished, the distribution side voltage of the OLTC is close to the reference value. Then the load could be considered as constant power load in some sense.

- Through the generic load itself: α changes from transient (short-term) characteristic to steady-state (long-term) characteristic driven by load dynamics. When the load becomes its long-term characteristic, the load restoration is achieved. It is direct. In Figure E.4, the load state variable changes according to the differential equations and also gives different short-term load characteristic curves. After the complete restoration, the load characteristic itself is constant power.

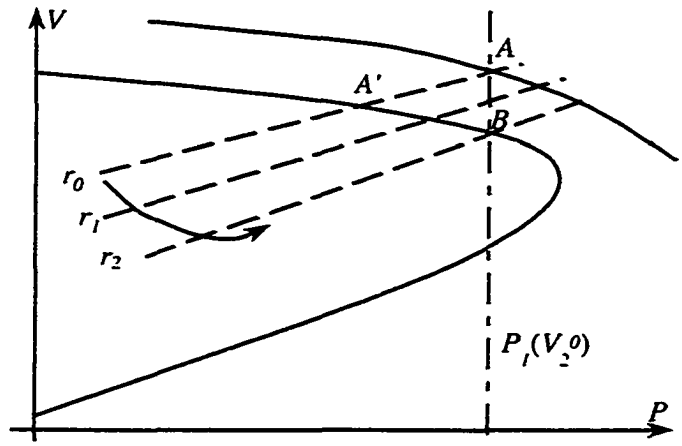

Figure E.3 Load restoration through OLTC

In the simulation of the New England system in Chapter 8, for Scenario One, the loads behind the OLTCs have constant impedance characteristics (E.6) and the other loads are modeled as constant power during the load restoration. Once the load restoration through OLTCs are achieved, all the loads are constant power loads.

However, the load model used for the simulation after the restoration is written as:

$$P_l = P_{l0}(1 + K_{lp}\lambda)\left(\frac{V_2}{V_{20}}\right)^{\alpha} \qquad \text{(E.7)}$$

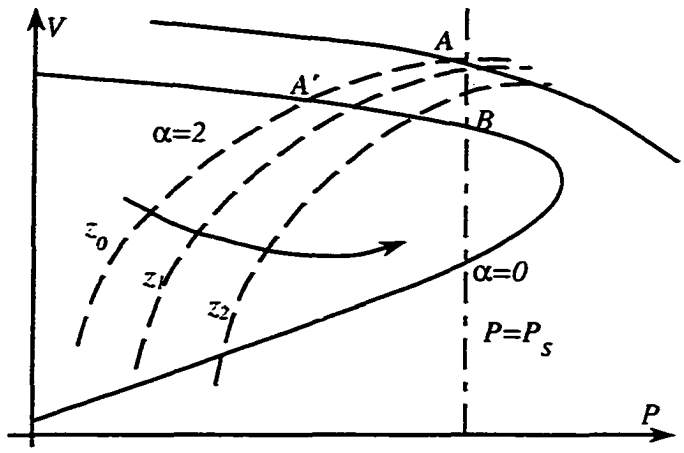

Figure E.4 Load restoration through the generic load itself

where $\alpha \neq 0$ and λ represents the total system load level. This load could be any type of load according to different α's.

Based on (E.7), we also can model other loads as constant impedance. Therefore, the mixture of all the loads is constant impedance load during the load restoration. After the restoration, it becomes the impedance-type load since three of them (after OLTCs) are constant power loads and the others are constant impedance loads. The long-term load characteristic curve shown in Figure 1.2 has to be changed accordingly. It is not a vertical line anymore.

APPENDIX F DAE, PV CURVE AND SADDLE NODE BIFURCATION

The general DAE model used for this study is:

$$\dot{z}_P = h(x, y, z_P) \tag{F.1}$$

$$0 = f(x, y, z_P) \tag{F.2}$$

$$0 = g(x, y, z_P) \tag{F.3}$$

where x, y and z have been defined before.

While tracing the PV curve, the load is specified at each equilibrium. Furthermore, the load has its own characteristic since it may be time varying or represented by differential equation to describe the dynamics involved. Actually these can be defined by the short-term and long-term load characteristic respectively. In this research, the load for the long term is characterized by λ and the load for the short term is characterized by z_P, which is the load state variable (x_L). λ is independent of other state variables and only time-dependent and it represents the load demand (z_L). In the load restoration procedure, $z_L = 1$.

F.1 Tracing PV Curve by Using λ

If short-term load dynamics (z_P) are not considered, each point on the PV curve is the solution of the following equations:

$$0 = f(x, y, \lambda) \tag{F.4}$$

$$0 = g(x, y, \lambda) \tag{F.5}$$

$$P = (1 + K\lambda)P(V) \tag{F.6}$$

$$\lambda = \lambda(t_k) \tag{F.7}$$

In Figure F.1, S and U are two different solutions for this set of equations. They are both the long-term equilibria of the system where S is stable and U is unstable. When λ changes from $\lambda(t_0)$ to the bifurcation point, which is defined as $\lambda(t_n)$, S and U shift from the left to right on the PV

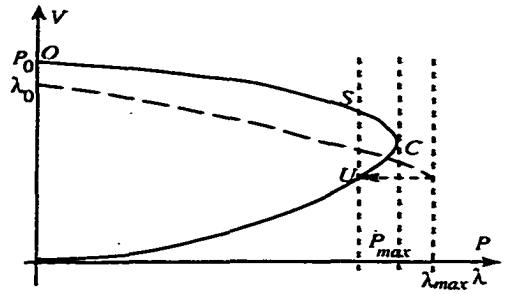

Figure F.1 PV curve with λ

curve according to the change of λ. At the saddle node bifurcation. S and U coincide and the system collapses. By analyzing the DAEs, we know that S and U are solved by:

$$\begin{bmatrix} 0 \\ 0 \end{bmatrix} = \begin{bmatrix} f_x & f_y \\ g_x & g_y \end{bmatrix} \begin{bmatrix} \Delta x \\ \Delta y \end{bmatrix} = J_{xy} \begin{bmatrix} \Delta x \\ \Delta y \end{bmatrix} \tag{F.8}$$

At a SNB point. J_{xy} becomes singular and λ. not P. achieves its maximal value. as shown in the figure. However. if the long-term load characteristic is $P = (1 + K\lambda)P_0$. then the maximal power point C is also the bifurcation point.

Generally. load dynamics drive the system to the saddle node bifurcation. From the analysis of Jacobian matrix. we may find the mechanism that causes the voltage collapse. For this case. load increase and OLTC actions can be considered as "dynamics" mainly involved. Directly from J_{xy}. OLTCs influence g_x and g_y significantly and load increase has great impact on the generation part of the system which is reflected in f_x and f_y. Both of them will result in the singularity of J_{xy}.

F.2 Tracing PV Curve by Using z_P

If short-term load dynamics z_P are considered. then:

$$0 = f(x, y, z_P) \tag{F.9}$$

$$0 = g(x, y, z_P) \tag{F.10}$$

$$\dot{z_P} = h(x, y, z_P) \tag{F.11}$$

$$P = P(z_P, V) \tag{F.12}$$

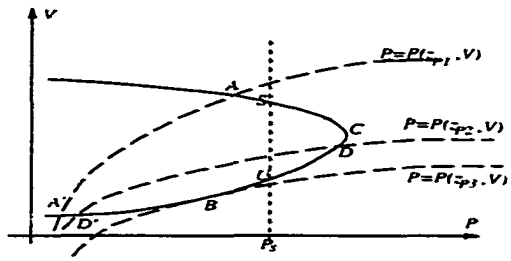

Figure F.2 PV curve with z_P

The solution of this set of equations is a curve in the three-dimensional $(x/y/z_P)$ space. Suppose O is a point on this curve, we project O to the PV plane, which is A shown in Figure F.2.

Different O's correspond to different A's on the PV curve. A is usually called the short-term equilibrium. It can be solved by:

$$0 = f(x, y, z_P) \tag{F.13}$$

$$0 = g(x, y, z_P) \tag{F.14}$$

$$z_P = z_P(t_k) \tag{F.15}$$

where z_P changes with the time by its self-control (restoration) mechanism represented by:

$$T_P \dot{z}_P = (P_s - P_t)/P_0 = (P_s - P(z_P, V))/P_0 \tag{F.16}$$

Newton method is applied for solving both O and A. For O,

$$\begin{bmatrix} \Delta \dot{z} \\ 0 \\ 0 \end{bmatrix} = \underbrace{\begin{bmatrix} h_z & 0 & h_y \\ 0 & f_x & f_y \\ g_z & g_x & g_y \end{bmatrix}}_{J_{total}} \begin{bmatrix} \Delta z \\ \Delta x \\ \Delta y \end{bmatrix} \tag{F.17}$$

While for A, based on the specific z_P which discretely changes,

$$\begin{bmatrix} 0 \\ 0 \end{bmatrix} = \begin{bmatrix} f_x & f_y \\ g_x & g_y \end{bmatrix} \begin{bmatrix} \Delta x \\ \Delta y \end{bmatrix} \tag{F.18}$$

From Appendix A, the reduced system matrix of long-term dynamics A_{lt} and the total Jacobian J_{total} have the following relationship:

$$Det[J_{total}] = Det[J_{xy}] Det[A_{lt}] \tag{F.19}$$

Load dynamics reflected in A_{lt}, such as thermostatic load self restoration, cause the singularity of A_{lt} as well as J_{total}. It is difficult to plot it in the three-dimensional space. However, we can clearly find the SIB point of the long-term dynamics (Appendix A), which is B in Figure F.2. Recalling (F.18) for solving λ, J_{xy} is calculated under a specific z_P value. When $P = P(z_P, V)$ is tangent to the PV curve, it means that J_{xy} becomes singular and (F.18) has no solution any more. According to the definition in Appendix A, B is the short-term saddle node bifurcation point induced by the long-term dynamics. Actually, this instability comes from the short-term dynamics closely related to f_x and f_y in J_{xy}. Note that B is evaluated under z_{P3}.

APPENDIX G COMPLETE DATA FOR THE NEW ENGLAND TEST SYSTEM

G.1 The IEEE Format Power Flow Data of the New England System

BUS DATA FOLLOWS 39 ITEMS

31 BUS31 1 1 0 0.9500 -13.41 0.00 0.00 0.00 0.00 0.00 0.0000 0.0000 0.0000 0.0000 0.0000 0 1

2 BUS2 1 1 0 0.9500 -11.22 0.00 0.00 0.00 0.00 0.00 0.0000 0.0000 0.0000 0.0000 0.0000 0 2

3 BUS3 1 1 0 0.9000 -13.88 275.00 112.40 0.00 0.00 0.00 0.0000 0.0000 0.0000 0.0000 0.0000 0 3

4 BUS4 1 1 0 0.9000 -14.02 515.70 158.00 0.00 0.00 0.00 0.0000 0.0000 0.0000 0.0000 0.0000 0 4

5 BUS5 1 1 0 0.9240 -12.25 0.00 0.00 0.00 0.00 0.00 0.0000 0.0000 0.0000 0.0000 0.0000 0 5

6 BUS6 1 1 0 0.9290 -11.41 0.00 0.00 0.00 0.00 0.00 0.0000 0.0000 0.0000 0.0000 0.0000 0 6

7 BUS7 1 1 0 0.9000 -13.76 290.80 70.00 0.00 0.00 0.00 0.0000 0.0000 0.0000 0.0000 0.0000 0 7

8 BUS8 1 1 0 0.9000 -14.33 600.00 226.00 0.00 0.00 0.00 0.0000 0.0000 0.0000 0.0000 0.0000 0 8

9 BUS9 1 1 0 0.9130 -14.60 0.00 0.00 0.00 0.00 0.00 0.0000 0.0000 0.0000 0.0000 0.0000 0 9

10 BUS10 1 1 0 0.9580 -9.42 0.00 0.00 0.00 0.00 0.00 0.0000 0.0000 0.0000 0.0000 0.0000 0 10

11 BUS11 1 1 0 0.9470 -10.10 0.00 0.00 0.00 0.00 0.00 0.0000 0.0000 0.0000 0.0000 0.0000 0 11

12 BUS12 1 1 0 0.9370 -10.24 7.50 77.00 0.00 0.00 0.00 0.0000 0.0000 0.0000 0.0000 0.0000 0 12

13 BUS13 1 1 0 0.9510 -10.23 0.00 0.00 0.00 0.00 0.00 0.0000 0.0000 0.0000 0.0000 0.0000 0 13

14 BUS14 1 1 0 0.9410 -12.19 0.00 0.00 0.00 0.00 0.00 0.0000 0.0000 0.0000 0.0000 0.0000 0 14

15 BUS15 1 1 0 0.9000 -13.34 375.00 136.00 0.00 0.00 0.00 0.0000 0.0000 0.0000 0.0000 0.0000 0 15

16 BUS16 1 1 0 0.9000 -12.16 371.20 122.30 0.00 0.00 0.00 0.0000 0.0000 0.0000 0.0000 0.0000 0 16

17 BUS17 1 1 0 0.9630 -13.12 0.00 0.00 0.00 0.00 0.00 0.0000 0.0000 0.0000 0.0000 0.0000 0 17

18 BUS18 1 1 0 0.9000 -13.86 145.00 27.00 0.00 0.00 0.00 0.0000 0.0000 0.0000 0.0000 0.0000 0 18

19 BUS19 1 1 0 1.0004 -7.87 0.00 0.00 0.00 0.00 0.00 0.0000 0.0000 0.0000 0.0000 0.0000 0 19

20 BUS20 1 1 0 0.9500 -9.48 767.00 198.00 0.00 0.00 0.00 0.0000 0.0000 0.0000 0.0000 4.0000 0 20

21 BUS21 1 1 0 0.9500 -9.83 269.00 108.00 0.00 0.00 0.00 0.0000 0.0000 0.0000 0.0000 0.0000 0 21

22 BUS22 1 1 0 1.0010 -5.44 0.00 0.00 0.00 0.00 0.00 0.0000 0.0000 0.0000 0.0000 0.0000 0 22

23 BUS23 1 1 0 0.9000 -5.65 253.50 83.60 0.00 0.00 0.00 0.0000 0.0000 0.0000 0.0000 0.0000 0 23

24 BUS24 1 1 0 0.9000 -12.07 296.60 85.20 0.00 0.00 0.00 0.0000 0.0000 0.0000 0.0000 0.0000 0 24

25 BUS25 1 1 0 0.9500 -10.02 228.00 46.90 0.00 0.00 0.00 0.0000 0.0000 0.0000 0.0000 0.0000 0 25

26 BUS26 1 1 0 0.9500 -11.40 136.00 45.00 0.00 0.00 0.00 0.0000 0.0000 0.0000 0.0000 0.0000 0 26

27 BUS27 1 1 0 0.9500 -13.40 263.00 71.50 0.00 0.00 0.00 0.0000 0.0000 0.0000 0.0000 0.0000 0 27

28 BUS28 1 1 0 0.9000 -8.01 585.00 27.60 0.00 0.00 0.00 0.0000 0.0000 0.0000 0.0000 0.0000 0 28

29 BUS29 1 1 0 0.9000 -5.23 645.50 126.90 0.00 0.00 0.00 0.0000 0.0000 0.0000 0.0000 0.0000 0 29

30 BUS30 1 1 2 0.9000 -8.97 0.00 0.00 230.00 181.51 0.00 0.9000 500.00 -100.00 0.0000 0.0000 0 30

1 BUS1 1 1 3 0.9000 0.00 0.00 0.00 1420.00 776.66 0.00 0.9000 999.00 -999.00 0.0000 0.0000 0 31

32 BUS32 1 1 2 1.0000 -1.58 0.00 0.00 630.00 475.85 0.00 1.0000 600.00 -300.00 0.0000 0.0000 0 32

33 BUS33 1 1 2 0.9000 -2.80 0.00 0.00 612.00 343.36 0.00 0.9000 500.00 -300.00 0.0000 0.0000 0 33

34 BUS34 1 1 2 1.0000 -4.49 0.00 0.00 488.00 -132.00 0.00 1.0000 500.00 -250.00 0.0000 0.0000 0 34

35 BUS35 1 1 2 1.0000 -0.58 0.00 0.00 630.00 355.70 0.00 1.0000 600.00 -250.00 0.0000 0.0000 0 35

36 BUS36 1 1 2 1.0000 2.01 0.00 0.00 540.00 132.64 0.00 1.0000 500.00 -220.00 0.0000 0.0000 0 36

37 BUS37 1 1 2 1.0000 -3.43 0.00 0.00 520.00 224.56 0.00 1.0000 500.00 -220.00 0.0000 0.0000 0 37

38 BUS38 1 1 2 1.0000 1.73 0.00 0.00 810.00 256.60 0.00 1.0000 500.00 -300.00 0.0000 0.0000 0 38

39 BUS39 1 1 2 0.9000 -14.69 975.00 202.00 1000.00 -84.37 0.00 0.9000 900.00 -900.00 0.0000 0.0000 0 39

-999

BRANCH DATA FOLLOWS 48 ITEMS

1 2 1 1 1 0 0.003500 0.041100 0.69870 0. 0. 0. 0 0 0.0000 0.00 0.0000 0.0000 0.0000 0.0000 0.0000 1

1 39 1 1 1 0 0.002000 0.050000 0.37500 0. 0. 0. 0 0 0.0000 0.00 0.0000 0.0000 0.0000 0.0000 0.0000 2

1 39 1 1 2 0 0.002000 0.050000 0.37500 0. 0. 0. 0 0 0.0000 0.00 0.0000 0.0000 0.0000 0.0000 0.0000 3

2 25 1 1 1 0 0.007000 0.008600 0.14600 0. 0. 0. 0 0 0.0000 0.00 0.0000 0.0000 0.0000 0.0000 0.0000 4

3 4 1 1 1 0 0.001300 0.021300 0.22140 0. 0. 0. 0 0 0.0000 0.00 0.0000 0.0000 0.0000 0.0000 0.0000 5

3 18 1 1 1 0 0.001100 0.013300 0.21380 0. 0. 0. 0 0 0.0000 0.00 0.0000 0.0000 0.0000 0.0000 0.0000 6

4 5 1 1 1 0 0.000800 0.012800 0.13420 0. 0. 0. 0 0 0.0000 0.00 0.0000 0.0000 0.0000 0.0000 0.0000 7

4 14 1 1 1 0 0.000800 0.012900 0.13820 0. 0. 0. 0 0 0.0000 0.00 0.0000 0.0000 0.0000 0.0000 0.0000 8

5 6 1 1 1 0 0.000200 0.002600 0.04340 0. 0. 0. 0 0 0.0000 0.00 0.0000 0.0000 0.0000 0.0000 0.0000 9

5 8 1 1 1 0 0.000800 0.011200 0.14760 0. 0. 0. 0 0 0.0000 0.00 0.0000 0.0000 0.0000 0.0000 0.0000 10

6 7 1 1 1 0 0.000600 0.009200 0.11300 0. 0. 0. 0 0 0.0000 0.00 0.0000 0.0000 0.0000 0.0000 0.0000 11

6 11 1 1 1 0 0.000700 0.008200 0.13890 0. 0. 0. 0 0 0.0000 0.00 0.0000 0.0000 0.0000 0.0000 0.0000 12

7 8 1 1 1 0 0.000400 0.004600 0.07800 0. 0. 0. 0 0 0.0000 0.00 0.0000 0.0000 0.0000 0.0000 0.0000 13

8 9 1 1 1 0 0.002300 0.036300 0.38040 0. 0. 0. 0 0 0.0000 0.00 0.0000 0.0000 0.0000 0.0000 0.0000 14

9 39 1 1 1 0 0.001000 0.025000 1.20000 0. 0. 0. 0 0 0.0000 0.00 0.0000 0.0000 0.0000 0.0000 0.0000 15

10 11 1 1 1 0 0.000400 0.004300 0.07290 0. 0. 0. 0 0 0.0000 0.00 0.0000 0.0000 0.0000 0.0000 0.0000 16

10 13 1 1 1 0 0.000400 0.004300 0.07290 0. 0. 0. 0 0 0.0000 0.00 0.0000 0.0000 0.0000 0.0000 0.0000 17

13 14 1 1 1 0 0.000900 0.010100 0.17230 0. 0. 0. 0 0 0.0000 0.00 0.0000 0.0000 0.0000 0.0000 0.0000 18

14 15 1 1 1 0 0.001800 0.021700 0.36600 0. 0. 0. 0 0 0.0000 0.00 0.0000 0.0000 0.0000 0.0000 0.0000 19

15 16 1 1 1 0 0.000900 0.009400 0.17100 0. 0. 0. 0 0 0.0000 0.00 0.0000 0.0000 0.0000 0.0000 0.0000 20

16 17 1 1 1 0 0.000700 0.008900 0.13420 0. 0. 0. 0 0 0.0000 0.00 0.0000 0.0000 0.0000 0.0000 0.0000 21

16 21 1 1 1 0 0.000800 0.013500 0.25480 0. 0. 0. 0 0 0.0000 0.00 0.0000 0.0000 0.0000 0.0000 0.0000 22

16 24 1 1 1 0 0.000300 0.005900 0.06800 0. 0. 0. 0 0 0.0000 0.00 0.0000 0.0000 0.0000 0.0000 0.0000 23

17 18 1 1 1 0 0.000700 0.008200 0.13190 0. 0. 0. 0 0 0.0000 0.00 0.0000 0.0000 0.0000 0.0000 0.0000 24

17 27 1 1 1 0 0.001300 0.017300 0.32160 0. 0. 0. 0 0 0.0000 0.00 0.0000 0.0000 0.0000 0.0000 0.0000 25

21 22 1 1 1 0 0.000800 0.014000 0.25650 0. 0. 0. 0 0 0.0000 0.00 0.0000 0.0000 0.0000 0.0000 0.0000 26

22 23 1 1 1 0 0.000600 0.009600 0.18460 0. 0. 0. 0 0 0.0000 0.00 0.0000 0.0000 0.0000 0.0000 0.0000 27

23 24 1 1 1 0 0.002200 0.035000 0.36100 0. 0. 0. 0 0 0.0000 0.00 0.0000 0.0000 0.0000 0.0000 0.0000 28

25 26 1 1 1 0 0.003200 0.032300 0.51300 0. 0. 0. 0 0 0.0000 0.00 0.0000 0.0000 0.0000 0.0000 0.0000 29

26 27 1 1 1 0 0.001400 0.014700 0.23960 0. 0. 0. 0 0 0.0000 0.00 0.0000 0.0000 0.0000 0.0000 0.0000 30

26 28 1 1 1 0 0.004300 0.047400 0.78020 0. 0. 0. 0 0 0.0000 0.00 0.0000 0.0000 0.0000 0.0000 0.0000 31

28 29 1 1 1 0 0.001400 0.015100 0.24900 0. 0. 0. 0 0 0.0000 0.00 0.0000 0.0000 0.0000 0.0000 0.0000 32

2 30 1 1 1 1 0.000000 0.018100 0.00000 0. 0. 0. 0 0 1.0250 0.00 0.0000 0.0000 0.0000 0.0000 0.0000 33

6 31 1 1 1 1 0.000000 0.050000 0.00000 0. 0. 0. 0 0 1.0700 0.00 0.0000 0.0000 0.0000 0.0000 0.0000 34

6 31 1 1 2 1 0.000000 0.050000 0.00000 0. 0. 0. 0 0 1.0700 0.00 0.0000 0.0000 0.0000 0.0000 0.0000 35

10 32 1 1 1 1 0.000000 0.020000 0.00000 0. 0. 0. 0 0 1.0700 0.00 0.0000 0.0000 0.0000 0.0000 0.0000 36

12 11 1 1 1 1 0.001600 0.043500 0.00000 0. 0. 0. 0 0 1.0060 0.00 0.9200 1.0800 0.0000 0.9500 1.0500 37

12 13 1 1 1 1 0.001600 0.043500 0.00000 0. 0. 0. 0 0 1.0060 0.00 0.9200 1.0800 0.0000 0.9500 1.0500 38

19 20 1 1 1 1 0.000700 0.013800 0.00000 0. 0. 0. 0 0 1.0600 0.00 0.9200 1.0800 0.0000 0.9500 1.0500 39

19 33 1 1 1 1 0.000700 0.014200 0.00000 0. 0. 0. 0 0 1.0700 0.00 0.0000 0.0000 0.0000 0.0000 0.0000 40

20 34 1 1 1 1 0.000900 0.018000 0.00000 0. 0. 0. 0 0 1.0250 0.00 0.8750 1.1250 0.0000 0.9500 1.0500 41

22 35 1 1 1 1 0.000000 0.014300 0.00000 0. 0. 0. 0 0 1.0250 0.00 0.0000 0.0000 0.0000 0.0000 0.0000 42

23 36 1 1 1 1 0.000500 0.027200 0.00000 0. 0. 0. 0 0 1.0000 0.00 0.0000 0.0000 0.0000 0.0000 0.0000 43

25 37 1 1 1 1 0.000600 0.023200 0.00000 0. 0. 0. 0 0 1.0250 0.00 0.0000 0.0000 0.0000 0.0000 0.0000 44

29 38 1 1 1 1 0.000800 0.015600 0.00000 0. 0. 0. 0 0 1.0250 0.00 0.0000 0.0000 0.0000 0.0000 0.0000 45

2 3 1 1 1 2 0.001300 0.015100 0.00000 0. 0. 0. 20 2 1.0600 0.00 0.0000 1.1000 0.0000 0.9000 1.1000 46

19 16 1 1 1 2 0.001600 0.019500 0.00000 0. 0. 0. 20 2 1.0600 0.00 0.0000 1.1000 0.0000 0.9000 1.1000 47

29 26 1 1 1 2 0.001700 0.013800 0.00000 0. 0. 0. 20 2 1.0600 0.00 0.0000 1.1000 0.0000 0.9000 1.1000 48

-999

LOSS ZONES FOLLOWS 2 ITEMS

-99

INTERCHANGE DATA FOLLOWS 1 ITEMS

-9

TIE LINES FOLLOW 0 ITEMS

-999

G.2 The ISU Format of the Dynamic Data of the New England System

Generator transient parameter follows

Num Gen name X_d X_q X'_d X'_q R_s T'_{d0} T'_{q0} M_g D_g

30 BUS30 0.1000 0.0690 0.0310 0.0690 0.0002 10.2000 0.010 84.000 5.000

31 BUS31 0.2590 0.2820 0.0700 0.1700 0.0002 6.5600 1.5000 60.600 5.000

32 BUS32 0.2500 0.2370 0.0530 0.0880 0.0002 5.7000 1.5000 71.600 5.000

33 BUS33 0.2620 0.2580 0.0440 0.1660 0.0002 5.6900 1.5000 57.200 5.000

34 BUS34 0.6700 0.6200 0.1320 0.1660 0.0002 5.4000 0.4400 52.000 5.000

35 BUS35 0.2540 0.2410 0.0500 0.0810 0.0002 7.3000 0.4000 69.600 5.000

36 BUS36 0.2950 0.2920 0.0490 0.1860 0.0002 5.6600 1.5000 52.800 5.000

37 BUS37 0.2900 0.2800 0.0570 0.0910 0.0010 6.7000 0.4100 48.600 5.000

38 BUS38 0.2110 0.2050 0.0570 0.0590 0.0002 4.7900 1.9600 69.000 5.000

39 BUS39 0.0200 0.0190 0.0060 0.0080 0.0002 7.0000 0.7000 1000.000 10.000

-999

Generator control system (excitor + AVR + governor) parameter follows

Num Gen name K_e T_e S_e K_a T_a K_f T_f T_{ch} T_g R_g

30 BUS30 1.0000 0.2500 0.0000 20.0000 0.0600 0.0400 1.0000 1.6000 0.2000 0.0500

31 BUS31 1.0000 0.4100 0.0000 40.0000 0.0500 0.0600 0.5000 54.1000 0.4500 0.0500

32 BUS32 1.0000 0.5000 0.0000 40.0000 0.0600 0.0800 1.0000 10.0000 3.0000 0.0500

33 BUS33 1.0000 0.5000 0.0000 40.0000 0.0600 0.0800 1.0000 10.1800 0.2400 0.0500

34 BUS34 1.0000 0.7900 0.0000 30.0000 0.0200 0.0300 1.0000 9.7900 0.1200 0.0500

35 BUS35 1.0000 0.4700 0.0000 40.0000 0.0200 0.0800 1.2500 10.0000 3.0000 0.0500

36 BUS36 1.0000 0.7300 0.0000 30.0000 0.0200 0.0300 1.0000 7.6800 0.2000 0.0500

37 BUS37 1.0000 0.5300 0.0000 40.0000 0.0200 0.0900 1.2600 7.0000 3.0000 0.0500

38 BUS38 1.0000 1.4000 0.0000 20.0000 0.0200 0.0300 1.0000 6.1000 0.3800 0.0500

39 BUS39 1.0000 1.0000 0.0000 20.0000 0.0200 0.0300 1.0000 10.0000 2.0000 0.0500

-999

Dynamic loads data follows

Num Bus name T_{pL} T_{qL} A_{Ld} B_{Ld} α_{Ld} β_{Ld}

-999

Static Var capacitor data follows

Num Bus name K_{svs} T_{svs} V_{svsr}

-999

On load tap-changer data follows

SN Secondary Bus PN Prime Bus T_r V_{rr}

3 BUS3 2 BUS2 0.250 1.000

16 BUS16 19 BUS19 0.250 1.000

26 BUS26 29 BUS29 0.250 1.000

-999

G.3 The ISU Format of the Control Parameter Limits Data of the New England System

IEEE NEW ENGLAND 39 BUS SYSTEM

THE AVR VOLTAGE LIMITS-FIELD CURRENT

30 1.4500

31 4.9000

32 3.2500

33 4.2500

34 8.2300

35 3.4000

36 3.6500

37 3.7500

38 3.4500

39 1.500

-999

THE GOVERNOR LIMITS-PGSMAX

30 3.1250

31 9.1500

32 8.1250

33 7.9000

34 6.3500

35 8.1250

36 7.0000

37 6.7500

38 10.3750

39 12.5000

-999

THE SHUNT CAPACITOR LIMITS

MAXIMUM: 10

MINIMUM:-10

-999

THE INTERRUPTED PERCENTAGE OF LOAD AT EACH BUS

MAXIMUM: 100

MINIMUM: 0

-999

THE VOLTAGE OPERATING LIMITS

MAXIMUM: 1.1

MINIMUM: 0.8

-999

THE TAP RATIO OPERATING LIMITS

MAXIMUM: 1.1

MINIMUM: 0.8

-999

G.4 One-Line Diagram of the New England 39-bus System

The one-line diagram of the New England 39-bus System is shown below:

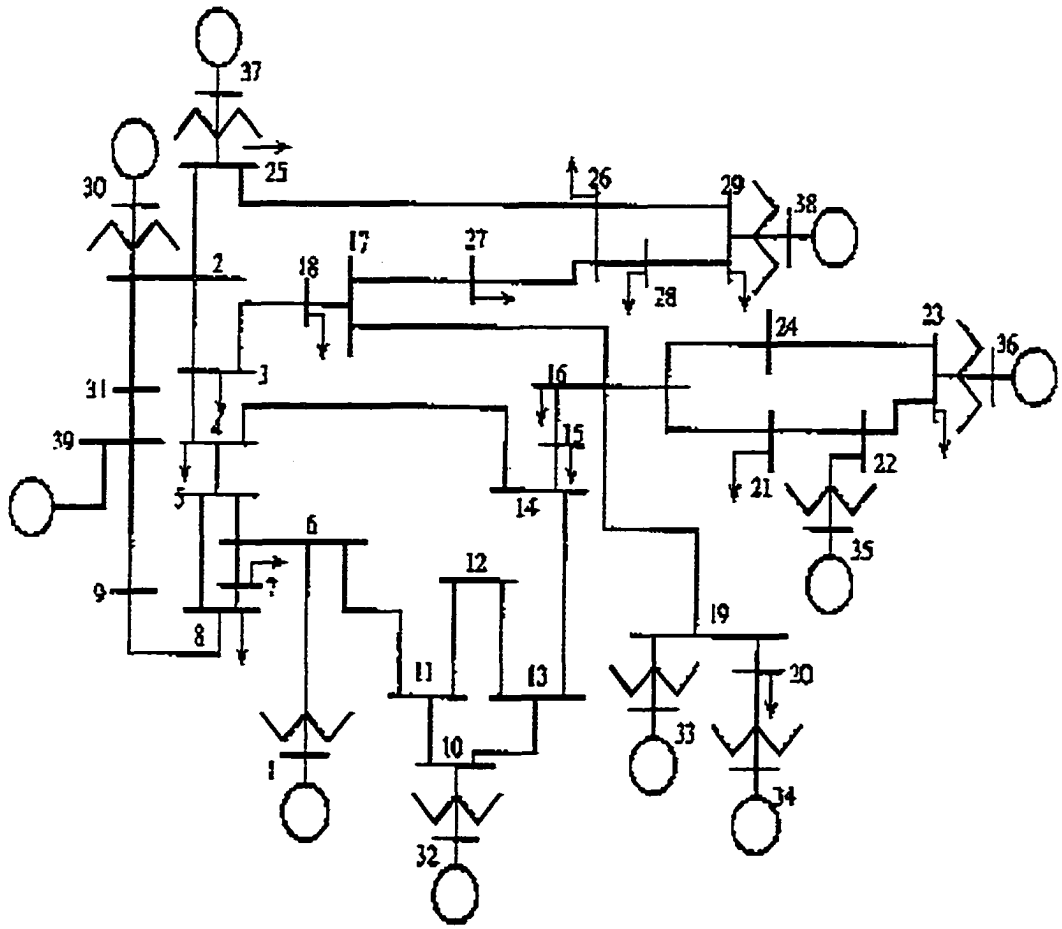

Figure G.1 One-line diagram of the New England 39-bus system

APPENDIX H THERMOSTATICALLY CONTROLLED LOAD

H.1 Introduction to Thermostatic Load

Thermostatically controlled loads, such as space heaters, molding and packaging machines, water heaters and the like, are very close to a constant impedance characteristic in the short-term scale. Such loads operate in a temperature range where the changes in power input do not alter temperature enough to noticeably affect the impedance. They can give considerable real power relief following a voltage depression induced by a contingency. However, it is still needed to maintain a constant temperature. How thermostatic loads achieve this will be explained as follows.

After the voltage decreases, the reduction in heat output from thermostatic loads will be sensed by thermostats and the "on" part of the thermostat cycle can be extended. Thermostats in the "off" period of their cycles will not respond to the voltage drop until they enter the "on" portion of their cycles. Because of the longer "on" period, more thermostats are in the "on" mode at any given instant when voltage is low, and the total load is thus the same as it is at normal voltage. Hence, the aggregate effect is to push the load power up towards a level that will produce the pre-contingency real power at the depressed voltage. Thermostatic loads are, effectively, constant power loads on a long-term basis.

In transient-stability study of less than about 5 minutes, thermostatic loads could be given a constant impedance characteristic. For a long-term study of several minutes or more duration, a dynamic characteristic, which begins with a step change in power and restores back to a new steady-state value with an appropriate time constant, should be applied. The values of the time constant between 5 to 30 minutes have been suggested [48]. When thermostatically controlled loads are subjected to a change in voltage, the transition from constant impedance characteristic to constant power characteristic is very typical. After the voltage drops, the load impedance initially remains unchanged and the load power decreases. Over time, this reduced electrical heating results in a fall in temperature. As explained before, individual thermostats compensate by increasing the "on" time of their impedance. Then the aggregate load impedance reduces (more devices on) and the aggregate load demand increases. The load will recover to a steady state in which the heater input is equal to the energy being lost to the surrounding

environment or in which the load restoration is limited by all the heaters being on continuously.

H.2 Mathematical Representation of Thermostatic Load

In Kundur's book [1], a thermostatically controlled load model is shown in Figure H.1. The dynamic equation of a heating device is also given in [1]:

$$K\frac{d\tau_H}{dt} = P_H - P_L \tag{H.1}$$

where τ_H is the temperature of the heated area, τ_A is the ambient temperature, $P_H = K_H G V^2$ is the power from the heater, $P_L = K_A(\tau_H - \tau_A)$ is the heat loss by escape to the ambient area, G is the load conductance, G_0 is the initial value of G, G_{max} is the maximum value of G, K_P is the gain of proportional controller, K_I is the gain of integral controller, T_C is the time constant of integral controller, τ_{ref} is the reference temperature, T_1 is the load time constant, K_1 is the gain associated with the load model.

The temperature τ_H is compared with the reference temperature, and the error signal controls the load conductance through a proportional plus integral controller. When all the thermostatically controlled loads supplied by the load bus are on, G reaches its maximum value G_{max}.

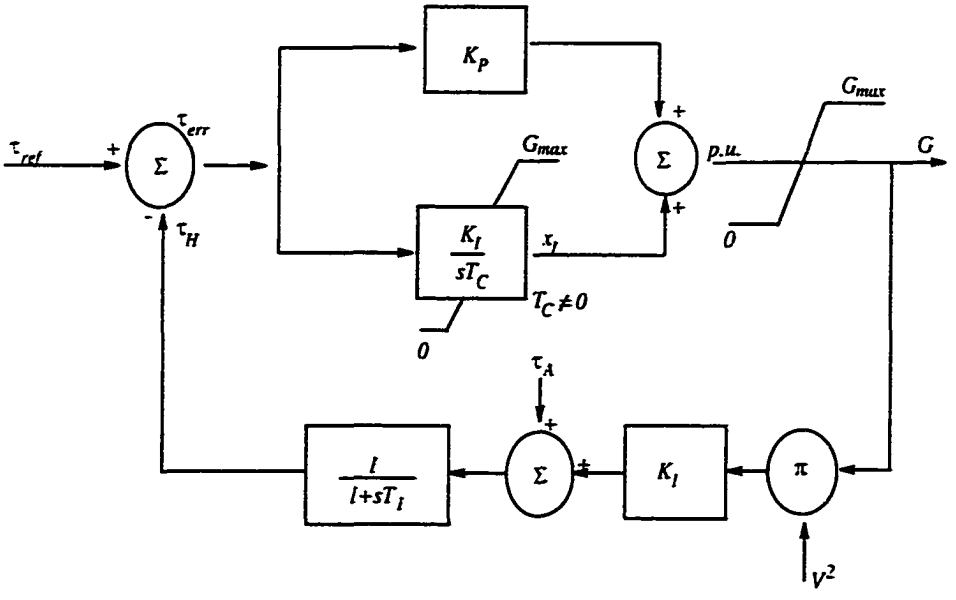

Figure H.1 A realistic model for thermostatically controlled loads [1]

In (H.1), the dynamic response of a thermostatically controlled load is represented by temperature. In [5], another expression of thermostatically controlled load is proposed:

$$T_P\dot{G} = P_0/V^2 - G \tag{H.2}$$

where T_P is the thermostatic load recovery time constant and P_0 is the total power drawn by all devices before the voltage change. The total load power at any point of time is given by:

$$P_d = GV^2 \tag{H.3}$$

H.3 Derivation from Thermostatic Load Model to Generic Load Model

We take (H.1) from Kundur's book [1] and (H.2) from V. Cutsem's book [5] as the differential representations of thermostatically controlled loads. Both of them are linked to the generic load model by D. J. Hill in [50].

For (H.1), assuming a linear resistance characteristic $G = \frac{1}{r\tau_H}$ (r is a constant), then:

$$P_H = K_H \frac{1}{r\tau_H} V^2 \tag{H.4}$$

Differentiating P_H, then:

$$\begin{aligned}
\dot{P}_H &= \frac{K_H}{r}\frac{2V\dot{V}\tau_H - V^2\dot{\tau}_H}{\tau_H^2} \\
&= -\frac{K_H}{r}\frac{V^2}{\tau_H^2}\dot{\tau}_H + \frac{2VK_H}{r\tau_H}\dot{V} \\
&= -\frac{K_H V^2}{r\tau_H^2 K}(P_H - P_L) + \frac{2V^2K_H}{r\tau_H V}\dot{V} \\
&= -\frac{K_H^2 V^4}{r^2\tau_H^2 K_H V^2}\frac{r}{K}(P_H - P_L) + \frac{2P_H}{V}\dot{V} \\
&= -\frac{P_H^2}{K_H V^2}\frac{r}{K}(P_H - P_L) + \frac{2P_H}{V}\dot{V}
\end{aligned} \tag{H.5}$$

or

$$\dot{P}_H + \frac{r}{KK_H}\frac{P_H^2}{V^2}(P_H - P_L) = \frac{2P_H}{V}\dot{V} \tag{H.6}$$

Similarly, from (H.2), we can get:

$$\begin{aligned}
\dot{P}_d &= \dot{G}V^2 + 2V\dot{V}G \\
&= \frac{1}{T_P}(P_0/V^2 - G)V^2 + \frac{2V^2G}{V}\dot{V} \\
&= \frac{1}{T_P}(P_0 - P_d) + \frac{2P_d}{V}\dot{V}
\end{aligned} \tag{H.7}$$

or

$$\dot{P}_d + \frac{1}{T_P}(P_d - P_0) = \frac{2P_d}{V}\dot{V} \tag{H.8}$$

or

$$T_P\dot{P}_d + P_d = P_0 + T_P\frac{2P_d}{V}\dot{V} \tag{H.9}$$

Equations (H.6) and (H.9) can be generalized to the form of generic load model proposed by D. J. Hill in [50], which is:

$$\dot{P}_d + f(P_d, V) = g(P_d, V)\dot{V} \tag{H.10}$$

However, in looking for a simple dynamic load model based on (H.10), a useful approximation is to assume an exponential recovery to the steady-state value. In [50], an additive load model, is given as below:

$$T_P\frac{d}{dt}P_d + P_d = P_S(V) + T_P\frac{d}{dt}(P_T(V)) \tag{H.11}$$

The above load model is expressed in the input-output form, which is shown in Figure H.2, where the input is voltage V and the output is the load power P_d. This block diagram form illustrates the interaction between nonlinear functions and a linear transfer function.

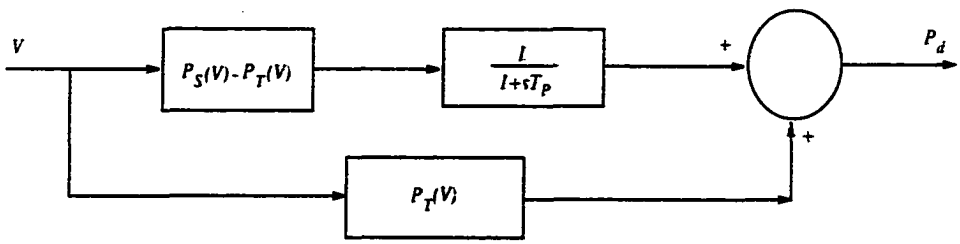

Figure H.2 Input-output form of generic load model

This was converted to the following form by introducing a state variable in [50]:

$$\dot{x_P} = -\frac{1}{T_P}x_P + N(V) \tag{H.12}$$

$$x_P = T_P(P_d - P_T(V)) \tag{H.13}$$

$$N(V) = P_S(V) - P_T(V) \tag{H.14}$$

where $P_S = P_{l0}(V/V_0)^{\alpha_S}$ and $P_T = P_{l0}(V/V_0)^{\alpha_T}$ for the exponential load model. By setting $x_P = T_P P_{l0} z_P$, we can transform (H.12) and (H.13) to the following equations:

$$T_P\dot{z_P} = -z_P + (\frac{V}{V_0})^{\alpha_S} - (\frac{V}{V_0})^{\alpha_T} \tag{H.15}$$

$$P_d = P_0((\frac{V}{V_0})^{\alpha_T} + \alpha_P) \tag{H.16}$$

This is the load-restoration model used in this research. When the voltage undergoes a step change, the internal state cannot change instantaneously. Over time x_P will respond, driven by (H.12). Steady state will be reached when $P_d = P_S(V)$. The initial transient step change in load, the final value of load, and the recovery rate are described by $P_T(V)$, $P_S(V)$ and T_P respectively. The exponential recovery load model is one example of load models that capture the smooth load behavior [79].

From (H.6) and (H.9), we know that thermostatic load model (H.9) and generic load model (H.11) essentially represent the same characteristic of the load, except that they are represented by different state variables. The load model used in this research (H.15) and (H.16)is in a special form of them. In fact, (H.9) could also be written as:

$$T_P \frac{d}{dt} P_d + P_d = P_S(V) + T_P \frac{d}{dt}(P_T(V)) \tag{H.17}$$

where $P_S(V) = P_0$, and $P_T(V) = \int_0^V \frac{2P_d}{\sigma} d\sigma + c_0$, c_0 is a constant.

The time constant used for thermostatic load model is generally 5 to 30 minutes. It means that thermostatic load restoration takes long time. Here we choose $T_P = 300s$. After the contingency, by assuming transient stability has been achieved, the new short-term equilibrium is established. Our simulation of load restoration begins at this point ($t = 0s$). If the system is stable during the load restoration, it will take $500 - 600s$ for the load to reach a new steady state. One example has been illustrated in [5]. However, since the contingency is so severe in this simulation, the system loses stability and collapses in the load restoration procedure. The collapse point may happen in a period of $100 - 200s$ from the base case ($t = 0s$). The load doesn't reach its new steady state at this point. This is the reason why the simulation shows up to only few hundred seconds.

BIBLIOGRAPHY

[1] P. Kundur. *Power System Stability and Control.* McGraw-Hill. New York. 1994.

[2] IEEE System Dynamic Performance Subcommittee, "Voltage stability of power systems: concepts. analytical tools and industry experience." *IEEE/PES Publication 90TH0358-2-PWR.* 1990.

[3] Y. Mansour. ed.. "Suggested techniques for voltage stability analysis." *IEEE Working Group on Voltage Stability, Publication 93TH0620-5-PWR.* 1993.

[4] C. W. Taylor. *Power System Voltage Stability.* McGraw-Hill. New York. 1994.

[5] T. Van Cutsem and Costa Vournas. *Voltage Stability of Electric Power Systems.* Kluwer Academic Publishers. Norwell. MA. 1998.

[6] *Voltage Stability of Power Systems: Concepts, Analytical Tools, and Industry Experience.* IEEE Working Group on Voltage Stability. 1990.

[7] *Criteria and Counter Measures for Voltage Collapse*, CIGRÉ Task Force 38.02.12. 1994.

[8] L. H. Fink. ed.. *Proc. of Bulk Power System Voltage Phenomena-III. Voltage Stability. Security and Control.* Davos. Switzerland. ECC/NSF, Workshop. Aug. 1994.

[9] C. W. Taylor, "Concepts of under voltage load shedding for voltage stability," *IEEE Trans. PD.* Vol. 7. Apr. 1992. pp. 480-488.

[10] T. Kumano. A. Yokoyama and Y. Sekine. "Fast monitoring and optimal preventive control of voltage instability." *Electrical Power and Energy Systems.* Apr. 1994. pp. 117-125.

[11] V.Venkatasubramanian. H.Schattler. and J.Zaborszky, "A taxonomy of the dynamics of the large power system with emphasis on its voltage stability," *Proc. of International Workshop on Bulk Power System Voltage Phenomena II-Voltage Stability and Security*, Maryland. USA. Aug. 1991. pp. 9-44.

[12] S. Arnborg, G. Andersson, D. J. Hill and I. A. Hiskens, "On undervoltage load shedding in power systems." *International Journal of Electrical Power and Energy Systems*. Vol. 19. No. 2. 1997. pp. 141-149.

[13] I. Dobson and L. Lu. "Voltage collapse precipitated by the immediate change in stability when generator reactive power limits are encountered." *IEEE Trans. Circuits and Systems Part I*. Vol. 39. Sep. 1992. pp. 762-766.

[14] F. Bourgin, G. Testud, B. Heilbronn and J. Verseille, "Present practices and trends on the French power system to prevent voltage collapse." *IEEE Trans. PWRS*. Vol. 8. No. 3. Aug. 1993. pp. 778-788.

[15] S. Greene. I. Dobson and F. L. Alvarado, "Sensitivity of the loading margin to voltage collapse with respect to arbitrary parameters." *IEEE Trans. PWRS*. Vol. 11. No. 2. May 1996. pp. 845-850.

[16] I. Dobson and L. Lu. "New methods for computing a closest saddle node bifurcation and worst case load power margin for voltage collapse." *IEEE Trans. PWRS*. Vol. 8. No. 3. Aug. 1993. pp. 905-913.

[17] B. Gao. G. K. Morison and P. Kundur, "Towards the development of a systematic approach for voltage stability assessment of large-scale power systems." *IEEE Trans. PWRS*. Vol. 11. No. 3. Aug. 1996. pp. 1314-1324.

[18] B. Gao. G. K. Morison and P. Kundur, "Voltage stability evaluation using modal analysis." *IEEE Trans. PWRS*. Vol. 7, No. 4. Nov. 1992, pp. 1529-1542.

[19] A. Tiranuchit and R. J. Thomas, "A posturing strategy against voltage instability in electric power systems." *IEEE Trans. PWRS*. Vol. 3, No. 1. Feb. 1988, pp. 87-93.

[20] T. Quoc Tuan. J. Fandino and J. C. Sabonnadiere. "Calculation of load shedding using sensitivities in order to avoid voltage collapse." *Proc. of 27th Universities Power Engineering Conference*. UPEC92. University of Bath, Sep. 1992. pp. 161-164.

[21] T. Quoc Tuan. J. Fandino. J. C. Sabonnadiere and H. Vu, "Emergency load shedding to avoid risks of voltage stability using indicators." *IEEE Trans. PWRS*. Vol. 9. No. 1. Feb. 1994. pp. 341-351.

[22] P. Kessel and H. Glavistch. "Estimation the voltage stability of a power system." *IEEE Trans. PD*. Vol. 1. Aug. 1986. pp. 346-354.

[23] T. Kumano, A. Yokoyama and Y. Sekine. "Dection of closest critical point and suboptimal preventive control of voltage stability," *Electrical Engineering in Japan*, Vol. 111, No. 3, 1991, pp. 89-97.

[24] R. Balanathan, N. C. Pahalawaththa, U. D. Annakkage, P. W. Sharp. "Undervoltage load shedding to avoid voltage instability," *IEE Proc.- Gener. Transm. Distrib.*, Vol. 145, March 1998, pp. 175-181.

[25] D. S. Popovic, V. A. Levi and Z. A. Gorecan, "Co-ordination of emergency secondary-voltage control and load shedding to prevent voltage instability," *IEE Proc.-Gener. Transm. Distrib.*, Vol. 144, May 1997, pp. 293-300.

[26] T. J. Overbye. "A power flow measure for unsolvable cases," *IEEE Trans. PWRS*, Vol. 9, No. 3, Aug. 1994, pp. 1359-1365.

[27] T. J. Overbye. "Computation of a practical method to restore power flow solvability," *IEEE Trans. PWRS*, Vol. 10, No. 1, Feb. 1995, pp. 280-287.

[28] T. Van Cutsem, Y. Jacquemart, J. N. Marquet and P. Pruvot. "A comprehensive analysis of mid-term voltage stability," *IEEE Trans. PWRS*, Vol. 10, No. 2, May 1995, pp. 1173-1182.

[29] T. Van Cutsem, "Analysis of emergency voltage situations," *Proc. of 11th Power System computation conference*, Avignon, France, Vol. 1, pp. 323-330.

[30] T. Van Cutsem. "An approach to corrective control of voltage instability using simulation and sensitivity," *IEEE Trans. PWRS*, Vol. 10, No. 2, May 1995, pp. 612-622.

[31] T. Van Cutsem, L. Wehenkel, M. Pavella, B. Heibronn and M. Goubin. "Decision tree approaches to voltage security assessment," *IEE Proc.-Gener. Transm. Distrib.*, Vol. 140, May 1993, pp. 189-198.

[32] S. Granville, J. C. O. Mello and A. C. G. Melo, "Application of interior point methods to power flow unsolvability," *IEEE Trans. PWRS*, Vol. 11, No. 2, May 1996, pp. 1096-1103.

[33] X. Wang, G. C. Ejebe, J. Tong and J. G. Waight. "Preventive/corrective control for voltage stability using direct interior point method," *IEEE Trans. PWRS*, Vol. 13, No. 3, Aug. 1998, pp. 878-883.

[34] S. K. Tso, T. X. Zhu, Q. Y. Zeng and K. L. Lo, "Evaluation of load shedding to prevent dynamic voltage instability based on extended fuzzy reasoning," *IEE Proc.- Gener. Transm. Distrib.*, Vol. 144, March 1997, pp. 81-86.

[35] M. K. Pal, "Assessment of corrective measures for voltage stability considering load dynamics." *Electrical Power and Energy Systems*, Vol. 17, No. 5, 1995, pp. 325-334.

[36] M. Eslami. *Theory of Sensitivity in Dynamic Systems*, Springer. New York. 1994.

[37] M. J. Laufenberg, M. A. Pai. "A new approach to dynamic security assessment using trajectory sensitivities." *IEEE Trans. PWRS*. Vol. 13, No. 3. Aug. 1998. pp. 953-958.

[38] T. Van Cutsem, C. D. Vournas. "Voltage stability analysis in transient and mid-term time scales." *IEEE Trans. PWRS*, Vol. 11, No. 1, Feb. 1996, pp. 146-154.

[39] B. Meyer, M. Stubbe. "EUROSTAG, a single tool for power system simulation." *Transmission and Distribution International*, Mar. 1992.

[40] M. Stubbe, A. Bihain, J. C. Baader, J. Deuse, "Simulation of the dynamic behavior of electrical power systems in the short- and long-terms." *CIGRÉ. Paper 38-03.*

[41] M. Stubbe, A. Bihain, J. Deuse, J. C. Baader, "STAG - a unified software program for the study of the dynamic behavior of electrical power systems." *IEEE Trans. PWRS*. Vol. 4, No. 1, Feb. 1989.

[42] P. Bornard, B. Meyer, M. Stubbe, J. P. Antoine, "EUROSTAG, a major step in power system simulation." *IERE - Rio de Janeiro meeting*, Brazil. 1991.

[43] J. Deuse, M. Stubbe, "Dynamic simulation of voltage collapse," *Proc. of IEEE/PES 1992 Summer Meeting*. Paper 396-2, Seattle, WA, 1992.

[44] J.Y. Astic, A. Bihain, and M. Jerosolimski, "The mixed Adams BDF variable step size algorithm to simulate transient and long term phenomena in power systems." *IEEE Trans. PWRAS*, Vol. 9, No. 2, May 1994, pp. 929-935.

[45] Z. Feng, V. Ajjarapu and B. Long, "Identification of voltage collapse through direct equilibrium tracing," *IEEE Trans. PWRS*, Vol. 15, No. 1, Feb. 2000, pp. 342-349.

[46] V. Ajjarapu and C. Christy, "The continuation power flow: a tool for steady-state voltage stability analysis." *IEEE Trans. PWRS*, Vol. 7, No. 1, Feb. 1992, pp. 416-423.

[47] M. K. Pal, "Voltage stability conditions considering load characteristics." *IEEE Trans. PWRS*, Vol. 7, No. 1, Feb. 1992, pp. 243-249.

[48] IEEE Task Force on Load Representation for Dynamic Performance, "Load representation for dynamic performance analysis," *IEEE Trans. PWRS*, Vol. 8, No. 2, May 1993, pp. 472-481.

[49] C. Concordia, S. Ihara, "Load representation in power system stability studies." *IEEE Trans. PAS-101*, 1982, pp. 969-977.

[50] D. J. Hill, "Nonlinear dynamic load models with recovery for voltage stability studies." *IEEE Trans. PWRS*, Vol. 8, No. 1, Feb. 1993, pp. 166-172.

[51] D. Karlsson, D. J. Hill, "Modeling and identification of nonlinear dynamic loads in power systems." *IEEE Trans. PWRS*, Vol. 9, No. 1, Feb. 1994, pp. 157-166.

[52] W. Xu, Y. Mansour, "Voltage stability analysis using generic dynamic load models." *IEEE. Tran. PWRS*, Vol. 9, No. 1, Feb. 1994, pp. 479-493.

[53] J. V. Milanovic, "On unreliability of exponential load models." *Electric Power System Research*, Vol. 49, 1999, pp. 1-9.

[54] R. Seydel, *From Equilibrium to Chaos-Practial Bifurcation and Stability Analysis*, Elsevier, New York, 1988.

[55] H. Ohtsuki, A. Yokoyama and Y. Sekine, "Reverse action of on-load tap changer in association with voltage collapse." *IEEE Trans. PWRS*, Vol. 6, No. 1, Feb. 1991, pp. 300-306.

[56] K. T. Vu, C. C. Liu, "Analysis of tap-changer dynamics and construction of voltage stability regions." *Proc. of IEEE ISCAS*, Vol. 3, 1988, pp. 1615-1618.

[57] K. T. Vu, C. C. Liu, "Shrinking stability regions and voltage collapse in power systems." *IEEE Trans. Circuits and Systems, Part I*, Vol. 39, No. 4, Apr. 1992, pp. 271-289.

[58] J. Medanić, M. Ilić and J. Christensen, "Discrete models of slow voltage dynamics for under load tap-changing transformer coordination," *IEEE Trans. PWRS*, Vol. 2, No. 2, May 1987, pp. 873-882.

[59] M. J. Laufenberg, M. A. Pai, "Dynamic sensitivity functions in power systems," *Proc. of the 27th Annual North American Power Symposium*, Oct. 1995, Bozeman, Montana, pp. 505-509.

[60] T. B. Nguyen, M. A. Pai, I. A. Hiskens, "Direct computation of critical clearing time using trajectory sensitivities." *Proc. of the IEEE Power Engineering Society Summer Meeting*, Vol. 1, July 2000, pp. 604-608.

[61] I. A. Hiskens, M. A. Pai, "Trajectory sensitivity analysis of hybrid systems," *IEEE Trans. on Circuits and Systems I: Fundamental Theory and Applications*, Vol. 47, No. 2, Feb. 2000, pp. 204-220.

[62] I. A. Hiskens, M. A. Pai, "Sensitivity analysis of power system trajectories: recent results," *Proc. of the 1998 IEEE International Symposium on Circuits and Systems*, Vol. 3, 1998, pp. 439–443.

[63] M. Caracotsios, W. E. Stewart, "Sensitivity analysis of initial value problems with mixed ODEs and algebraic equations," *Computers and Chemical Engineering*, Vol. 9, No. 4, 1985, pp. 359-365.

[64] T. Van Cutsem, Y. Jacquemart, J. N. Marquet, P. Pruvot, "Extensions and applications of a mid-term voltage stability analysis method," *Proc. 3rd intern. workshop on bulk power system voltage phenomena-voltage stability and security*, Davos, Switzerland, Aug. 1994, pp. 251-270.

[65] T. Van Cutsem, R. Mailhot, "Validation of a fast voltage stability analysis method on the Hydro-Quebec system," *IEEE Trans. PWRS*, Vol. 12, No. 1, Feb. 1997, pp. 282-292.

[66] C. L. Demarco, B. R. Barmish, "A result on tracking equilibria for slowly varying nonlinear systems," *Proc. of 1986 American Control Conference*, June 1986, pp. 362-372.

[67] B. Long and V. Ajjarapu, "The sparse formulation of ISPS and its application to voltage stability margin sensitivity and estimation," *IEEE Trans. PWRS*, Vol. 14, No. 3, Aug. 1999, pp. 944-957.

[68] Z. Feng, V. Ajjarapu and D. J. Maratukulam, "A practical minimum load shedding strategy to mitigate voltage collapse," *IEEE Trans. PWRS*, Vol. 13, No. 4, Nov. 1998, pp. 1285-1291.

[69] C. Moors, T. Van Cutsem, "Determination of optimal load shedding against voltage instability," *Proc. of 13th PSCC*, June 28-July 2, 1999, Trondheim, Norway, pp. 993-1000.

[70] T. Van Cutsem, C. Moisse, R. Mailhot, "Determination of secure operating limits with respect to voltage collapse," *IEEE Trans. PWRS*, Vol. 14, No. 1, Feb. 1999, pp. 327-335.

[71] B. Lee and V. Ajjarapu, "Invariant subspace parametric sensitivity (ISPS) of structure preserving power system models," *IEEE Trans. PWRS*, Vol. 11, No. 2, May 1996, pp. 845-850.

[72] S. Arnborg, G. Andersson, D. J. Hill and I. A. Hiskens, "The influence of load modeling for undervoltage load shedding studies," *IEEE Trans. PWRS*, Vol. 13, No. 2, May 1998, pp. 395-400.

[73] D. Karlsson, *Voltage stability simulations using detail models based on field measurements*, Ph.D. thesis, Technical Report 230, Dept. of Electrical Power Systems, Chalmers University of Technology, Gothenburg, Sweden, 1992.

[74] Z. Feng, V. Ajjarapu, D. J. Maratukulam, "A comprehensive approach for preventive and corrective control to mitigate voltage collpase," will be published in *IEEE Trans. PWRS*, PE-290PRS (10-99).

[75] B. Lee, *A unified framework to study the voltage stability of the structure-preserving power system model*, PhD Thesis, Iowa State University, 1994.

[76] J. Carpentier, R. Girard and E. Scano, "Voltage collapse proximity indicators computed from an optimal power flow," *Proc. 8th PSCC*, Aug. 1984, pp. 671-678.

[77] M. Begovic, A. Phadke, "Control of voltage stability using sensitivity analysis," *IEEE Trans. PWRS*, Vol. 7, No. 1, Feb. 1992, pp. 114-123.

[78] I. Dobson, "Observations on the geometry of saddle node bifurcation and voltage collapse in electric power systems," *IEEE Trans. Circuit and Systems Part I*, Vol. 39, March 1992, pp. 240-243.

[79] IEEE/PES Power System Stability Subcommittee, "Voltage stability assessment, procedures and guides," *Final Draft*, Jan. 2001.